

NORTHWESTERN UNIVERSITY

A DISSERTATION

Multi-Scale Electron Microscopy Imaging Platform for Quantifying Genome Organization

SUBMITTED TO THE GRADUATE SCHOOL
IN PARTIAL FULFILLMENT OF THE REQUIREMENTS

for the degree

DOCTOR OF PHILOSOPHY

Applied Physics

By

Yue Li

EVANSTON, ILLINOIS

September 2019

© Copyright by Yue Li, 2019

All Rights Reserved

ABSTRACT

Multi-Scale Electron Microscopy Imaging Platform For Quantifying Genome Organization

Yue Li

The structural aspects of biological systems are tightly paired with their functions. This understanding has been demonstrated over a broad range of length scales, spanning the ultrastructure of a cell to the macroscopic architecture of organs. Connecting structure and function relies on the integration of physical and biological sciences to analyze the fundamental arrangement and cooperation of specific sets of biomolecules, frequently at the nanoscale. One crucial area within this nano regime is the study of the folding of chromatin and its relation to critical biological processes such as transcription, replication, differentiation, DNA repair, and apoptosis.

In molecular biology, angstrom resolution imaging through cryo-electron microscopy has been routinely performed to solve the structure of virus, protein, and macromolecules. On the other end, in cellular biology, the conventional electron microscopy has been utilized to provide ultrastructure for organelles for many decades. For epigenomics, the unique challenges in quantifying the chromatin organization are twofold: 1. The demand for ultra-high resolution and large imaging volume. 2. The demand for identifying structures based on their molecular functions. While the fundamental components of chromatin, the nucleotides, are only ~ 1 nm (the DNA double-helix is 2 nm across), they self-organize into a massive hierarchical polymer

complex, the chromosomes, which are distributed over a distance of tens of microns within the cell nucleus. For most ultra-thin TEM samples, the contrast in electron micrographs originates from the phase shift of electrons passing through the specimen and interfering on the detector. On the other hand, for thick specimens like chromatin, large-angle scattering of electrons passing through the biological sample dominates the image contrast, and the image intensity reflects primarily the mass-thickness distribution. Although it is possible to identify specific organelles through morphological information such as mitochondria, it is difficult, if not impossible, to differentiate different types of nucleic acids from electron micrographs, let alone genes with different transcription states.

Within this work, we introduce multiple methods specifically designed to overcome the issues in adapting electron microscopy in chromatin imaging. In Chapter 1, we review needs in chromatin characterization and the major advances in electron microscopy over the last few years, as well as outstanding challenges in comprehensive quantification of genome organization. We highlight the demand for novel imaging methods for ultra-thick, low-contrast, and beam sensitive samples, such as chromatin. Expanding on this, Chapter 2 discusses the practical implementation of a label-free three-dimensional tomography reconstruction of a whole mammalian cell. Chapter 3 further advances this topic by introducing molecular specific labeling into electron tomography reconstruction. Combining previously reported DNA labeling ChromEM with quantitative high angle annular dark field (HAADF) imaging mode in the scanning transmission electron microscopy (STEM) for thick samples, the hybrid method, ChromSTEM, effectively kills two birds with one stone. The work shifts gears slightly in Chapter 4 for introducing a shortcut to obtain the label-free chromatin distribution for the whole cell statistically instead of deterministically, in

comparison with Chapter 2. Chapter 5 will discuss the potential of utilizing novel sparse-sampling and inpainting to reduce beam damage in 3D tomography reconstruction even further. Finally, in Chapter 6, we will discuss the potentials of a consolidated nanoimaging platform featuring Spectroscopic Intrinsic Contrast photon-localization Nanocsopy (SICLON), 3D Spectroscopic Photon-Localization Microscopy (SPLM), and ChromSTEM. Future directions and potential expansions on the preliminary work is discussed in this thesis. The consistent theme of this work is the development and adaptation of advanced microscopy in quantifying the genome organization over a broad range of length scales, particularly with an eye towards reducing the time or integrated electron dose for critical information. In many cases, we find that vast new information can be obtained with simple innovations in conventional electron microscopy, and the future of epigenomics will likely be at the interface of computation, microscopy, and sequencing studies.

Thesis Advisors: Prof. Vinayak P. Dravid and Prof. Vadim Backman

ACKNOWLEDGMENTS

The past five years has been a self-discovery adventure, and this work has been the surprise and the pride of my life. I cannot overstate the excitement in approaching the conclusions and the enjoyment in pushing the boundary of our understanding of science. I am genuinely grateful to all the people who have made this possible: both because of their intellectual and personable contributions.

I want to begin by thanking my mother for providing her support and encouragement that is a necessity for me to complete such an endeavor. The trajectory of my life towards this moment has been circuitous, and quite frankly, being the first Ph.D. in STEM major, including my extended family, is an honor. This honor will not be possible without the sacrifices my mother made for me to be here – sending her only child to the other hemisphere and providing her wisdom whenever her daughter is in a difficult situation. From the bottom of my heart, I thank her for all she had given me. With that in mind, I would also like to deeply thank Dr. Karl Hujsak for the love and support, both emotionally and scientifically, during the years of this Ph.D. Karl is my smartest colleague, best friend and the love of my life, I learned so much from him and everything he has done has made this possible. I hope this work is a small gift to honor them all by.

Next, I want to thank the mentorship and advice from Prof. Vinayak P. Dravid and Prof. Vadim Backman. I have had the pleasure of being your student, mentee, and colleague these last five years. Although I did not always deserve it, I am positive their dedication to their students' success is the major reason I have been able to complete my Ph.D. They consistently put the wellbeing of their students first and foremost, making the one-on-one time a priority for all

members of the group. While I did not realize it at the time, by pushing me outside my comfort zone, I have grown more than I possibly could have imagined before starting at Northwestern. The guidance they both have provided have molded me into a more thoughtful scientist and beyond.

I want to thank Dr. Reiner Bleher and Mr. Eric Roth for the training, thoughts, support, and friendship. Simply put, they are the best colleagues anyone could ever hope to work with. None of this work would have gotten off the literal drawing board without their help. They have truly been an inspiration; they encompass a rare combination of work ethics, extreme intelligence, and friendly demeanor. I want to also thank all the members in both labs for their questions, discussions, and collaboration. In particular, from the Backman lab, I would like to thank in no particular order: Dr. Di Zhang, Dr. Lusik Cherkezyan, Dr. Luay Almassalha, Dr. Adam Eshein, Dr. Scott Glastein, Dr. Greta Bowers, Maria Proenca, Benjamine Keane, Vasundhara Agrawal, Jane Frederick, Ranya Virk, David VanDerway and Xiang Zhou. Likewise, from the VPD Lab and NUANCE center, I would like to thank Dr. Jingson Wu, Dr. Shuyou Li, Dr. Benjamin Myers, Dr. Kai He, Dr. Vikas Nadwana, Dr. Qin Tu, Amy Morgan, Elise Beck, Kelly Parker, Jen DiStephano, Tirzah Abbott, Xiaomi Zhang, Chamille Lescott and Will Kellogg. In addition, I would like to thank the outstanding collaborators, in particular, the remarkable scientists and friends, Prof. Igal Szleifer, Prof. Hao Zhang, Dr. Doga Gursoy, Dr. Pablo Mataran, Prof. Aggelos Katsaggelos, Prof. Ollie Cossairt, Prof. Richard Leapman, Dr. Yang Zhang, Dr. Kai Huang, and Anne Shim. I have learned so much from all of you – this work was only possible through the combined work of all of these brilliant colleagues.

I would also like to thank my mentors, who have supported me throughout my education. In no particular order, I thank Prof. Chris Wolverton and Prof. Erik Luijten, Prof. Jiaxin Huang,

Prof. Yip-Wah Chung, without their help I would not have even started this journey; Prof. Lincoln Lauhon, Prof. Jen Koch for helping me navigating through the Ph.D. program; Prof. Chris Jacobsen and Prof. John Marko for being on my committee and their helpful feedback on my thesis.

Born and raised in China, I was fortunate during my time at Northwestern to enjoy the friendship of many of my cohort and others from the greater diverse community. They have made this time especially meaningful, and I will carry many memories forward with me. Special thanks to my dancing friends in NuBlast, NuTango to keep me active physically and emotionally and help me stay engaged in social events during my Ph.D. In no particular order, I'd like to thank Angelia Wang, Peter Tran, Tiffany Jeung, Sophia Wienbar, Jerome Dyson, Vicky Yang, Anh Le, and Shirley Zhang. Extra special thanks to Karl for putting up with me going out to dance, hosting my dance friends over, and even learning to dance, for all this time.

Yue

June 2019

DEDICATION

This dissertation is dedicated to my mother, Prof. Renzhen Li, for the love and support, which put me on this path.

TABLE OF CONTENTS

ABSTRACT	3
ACKNOWLEDGMENTS	6
DEDICATION.....	9
CHAPTER 1 INTRODUCTION	37
1.1 PHILOSOPHY AND APPROACH	37
1.2 INTRODUCTION TO 3D GENOME ORGANIZATION	38
1.2.1 <i>3D Genome Organization in Regulating Gene Transcription.....</i>	<i>38</i>
1.2.2 <i>Techniques to Investigate 3D Genome Organization</i>	<i>39</i>
1.3 A GENERAL INTRODUCTION TO MODERN ELECTRON MICROSCOPY	41
1.3.1 <i>Quantitative imaging Using Scanning Transmission Electron Microscopy (STEM).....</i>	<i>44</i>
1.3.2 <i>High-resolution 3D Reconstruction through Electron Tomography.....</i>	<i>45</i>
1.3.3 <i>Challenges of Utilizing Electron Microscopy in Characterizing Chromatin</i>	<i>48</i>
1.4 SCOPE OF THE DISSERTATION	54
CHAPTER 2 LABEL-FREE 3D IMAGING OF MAMMALIAN CELLS USING SCANNING TRANSMISSION ELECTRON TOMOGRAPHY	56
2.1 IMAGING THICK BIOLOGICAL SAMPLE	56
2.2 CHALLENGES IN IMAGING THICK BIOLOGICAL SAMPLES	57
2.3 SOLUTIONS TO IMAGE THICK BIOLOGICAL SAMPLES	59
2.4 MATERIALS AND METHODS	60
2.4.1 <i>Entire Cheek Cell Preparation for STEM tomography</i>	<i>60</i>

2.4.2	<i>Optimization of Electron Microscope Setup</i>	61
2.4.3	<i>Dual-tilt Tomography Reconstruction</i>	63
2.5	DISCUSSIONS AND CONCLUSIONS	67
CHAPTER 3 MULTI-SCALE QUANTIFICATION OF 3D GENOME ORGANIZATION		
USING SCANNING TRANSMISSION ELECTRON MICROSCOPY: CHROMSTEM.. 73		
3.1	PREVIOUS WORK ON 3D CHROMATIN IMAGING	74
3.2	CHROMSTEM PLATFORM FORMULATION	75
3.2.1	<i>Overview of the ChromSTEM Platform</i>	76
3.2.2	<i>ChromSTEM sample preparation</i>	78
3.2.3	<i>ChromSTEM Tomography of Cell Nucleus</i>	84
3.2.4	<i>ChromSTEM Imaging of Tissue Biopsies</i>	88
3.3	QUANTIFYING 3D GENOME ORGANIZATION USING CHROMSTEM	91
3.3.1	<i>Internal Structure of Chromatin Packing Domains</i>	91
3.3.2	<i>ChromSTEM Analysis of Nanoscale Chromatin Packing Domains</i>	96
3.3.3	<i>Comparison of Chromatin Packing for Different Nuclear Compartments</i>	107
3.3.4	<i>Comparison of Chromatin Packing for Different Nuclear Compartments in Mouse Ovary</i>	111
3.4	DISCUSSIONS AND CONCLUSIONS	113
CHAPTER 4 RECONSTRUCTION OF 3D AUTOCORRELATION FUNCTION FROM		
2D AUTOCORRELATION FUNCTION: CORRELATIVE SCANNING TRANSMISSION		
ELECTRON MICROSCOPY AND ATOMIC FORCE MICROSCOPY 117		

4.1	PREVIOUS WORK ON 3D CHARACTERIZATION OF MAMMALIAN CELLS.....	118
4.2	THE WORKFLOW OF THE RECONSTRUCTION METHOD.....	118
4.3	MATHEMATICAL FORMULATION AND NUMERICAL VALIDATION OF THE ALGORITHM ...	121
4.4	MATERIALS AND METHODS.....	124
4.4.1	<i>Sample Preparation</i>	124
4.4.2	<i>Quantitative High Angle Annular Dark Field Imaging Through Z-contrast</i>	125
4.4.3	<i>Correlative Atomic Force Microscopy (AFM)</i>	128
4.4.4	<i>Mass and Thickness Mapping for a Human Cheek Cell</i>	130
4.4.5	<i>3D Autocorrelation Function Reconstruction for a Human Cheek Cell</i>	132
4.5	DISCUSSIONS AND CONCLUSIONS.....	134
CHAPTER 5 INPAINTING ASSISTED CONTROLLED ROTATION TOMOGRAPHY:		
CORT	136
5.1	RADIATION DAMAGE FOR BEAM SENSITIVE SAMPLES.....	137
5.2	INTRODUCTION TO SPARSE IMAGING.....	139
5.2.1	<i>Sparse Imaging Theory</i>	139
5.2.2	<i>Experimental Implementation of Sparse Imaging in Electron Microscopy</i>	141
5.3	CORT METHODOLOGY FORMULATION.....	143
5.3.1	<i>Mathematical Formulation of CORT Sampling</i>	143
5.3.2	<i>Workflow of CORT</i>	145
5.4	CORT PERFORMANCE EVALUATION.....	147
5.4.1	<i>Influences of Angular Averaging</i>	147
5.4.2	<i>Intuition for CORT Data</i>	149

5.4.3	<i>Sample Rotation Speed and the Distribution of Visited Pixels in the Sinogram</i>	152
5.4.4	<i>Modeling Inorganic Sample: Double-Walled Carbon-Nanotubes with Silver Nanoparticles</i>	153
5.4.5	<i>Modeling Organic Sample: Human Cheek Cell</i>	156
5.5	DISCUSSION AND CONCLUSIONS	160
CHAPTER 6 FUTURE OUTLOOK AND CONCLUSIONS		162
6.1	SPECTROSCOPIC INTRINSIC-CONTRAST PHOTON-LOCALIZATION OPTICAL NANOSCOPY (SICLON) FOR LABEL-FREE NUCLEIC ACIDS IMAGING	162
6.1.1	<i>SICLON: Super-Resolution Microscopy for Label-Free Imaging at Sub-10 nm Resolution.....</i>	164
6.1.2	<i>Quantification of Chromatin Structure from SICLON Images</i>	166
6.1.3	<i>Chromatin Alterations Detection in Wild Type and Chemo-Treated Ovarian Cancer Cell Lines.....</i>	167
6.1.4	<i>Discussions and Conclusions.....</i>	169
6.2	MULTI-TECHNIQUE-MULTI-SCALE (MTMS) IMAGING PLATFORM: BRIDGING THE PHYSICAL AND GENOMIC LANDSCAPE IN CHROMATIN	170
6.2.1	<i>Significance of Developing a Microscopy-Based Multi-Technique Multi-Scale Imaging Platform for Genomics Analysis</i>	171
6.2.2	<i>Formulation of the Microscopy-Based Multi-Technique Multi-Scale (MTMS) Imaging Platform.....</i>	173
6.2.3	<i>The workflow of the Microscopy-Based Multi-Technique Multi-Scale (MTMS) Imaging Platform</i>	174

6.2.4	<i>Materials and Methods</i>	176
6.2.5	<i>Chromatin Forms Spatially Separable Packing Domains with Fractal Internal Structures</i>	180
6.2.6	<i>Characterizing Dexamethasone-Induced Time-Sensitive Chromatin Packing Alterations</i>	182
6.2.7	<i>Discussions and Conclusions</i>	189
6.3	CORRELATIVE SUPER RESOLUTION AND ELECTRON MICROSCOPY (cSRAEM) TO RELATE STRUCTURE-FUNCTION RELATION FOR CHROMATIN ORGANIZATION AND GENE TRANSCRIPTION	
	190	
6.3.1	<i>Adding Colors to the Electron Micrographs</i>	190
6.3.2	<i>Combining Super-Resolution and Electron Microscopy</i>	192
6.3.3	<i>Materials and Methods</i>	193
6.3.4	<i>Preliminary results for cSRAEM with A2780</i>	195
6.3.5	<i>Discussions and Conclusions</i>	196
6.4	CONCLUDING COMMENTS	196
	REFERENCES	198
	APPENDIX	223
	APPENDIX A: CHEMICALS USED IN CHROMSTEM STAINING	223
	APPENDIX B: SAMPLE PREPARATION FOR CHROMSTEM FOR CELL CULTURES	225
	APPENDIX C: SAMPLE PREPARATION FOR CHROMSTEM FOR TISSUE BIOPSIES	227
	APPENDIX D: SAMPLE PREPARATION AND IMAGING FOR PHOTON LOCALIZATION MICROSCOPY OF A549	228

APPENDIX E: SAMPLE PREPARATION FOR WHOLE CHEEK CELL STEM TOMOGRAPHY	230
APPENDIX F: PUBLICATIONS	232

LIST OF FIGURES

- Figure 1.1** Relationship between intensity and mass in HAADF images as a function of the inner semi-collection angle. (a) Linear coefficient of intensity and mass as we change the projection lens current, the selected inner semi-collection angle is 72.3 mrad when considering linearity and signal to noise ratio. (b) to (f) HAADF image of a polystyrene bead recorded at 10K magnification from larger projection lens current to smaller projection lens current. Scale bar, 1 μm **45**
- Figure 1.2** Principle and workflow of electron tomography for biological samples. The sample is generally tilted from -70° to 70° or -60° to 60° and the projection image at each tilt is collected sequentially. The tilt series is then aligned and reconstructed for 3d structure. Volume/surface rendering can be employed to assist visualization, and image segmentation is generally performed to identify useful features. **47**
- Figure 2.1** Intrinsic trade-off between lateral resolution and depth of field (DOF) for STEM imaging for thick samples. The DOF is inversely related to the convergence angle while the lateral resolution is positively correlated with the convergence angle. At high tilt, a small DOF will limit the region in the sample in focus. **59**
- Figure 2.2** Effects of convergence angle in image quality at different tilt angles. A convergence angle of 10 mrad and parallel probe ($\sim 0^\circ$) was employed for sample oriented at 0° tilt and 60° tilt. For the low tilt angle, under current magnification, the resolution is identical for both probes. For the high tilt angle, the 10 mrad convergence angle provided a small DOF, and the edge of the cell was not in focus. In contrary, the parallel probe was able to capture the entire cell in focus. **62**

Figure 2.3 Estimation of the resolution of a parallel probe at higher magnification. We obtained the image resolution by the full-width-half-maximum (FWHM) of the first derivative (b, blue curve) of the intensity line profile (b, black curve) across a gold nanoparticle (a, red line). Scale bar: 100 nm for (a)..... **63**

Figure 2.4 STEM tomography tilt series of a whole cheek cell. Top panel: The cheek cell was deposited on the top surface of the TEM grid for the first tilt series (Axis A). Later, the sample was manually flipped upside-down and rotated 90° laterally for the second tilt series (Axis B). Middle and bottom panel: examples of HAADF images of the sample at different tilt angles with respect to Axis A and B. Scale bar: 10 μm. **64**

Figure 2.5 Tomography reconstruction of an entire human cheek cell. (a) One virtual 2D slice with a nominal thickness of 73 nm in the middle of the cell. Scale bar: 10 μm. (b) Volume rendering of the tomography, x-z (side) view. Scale bar: 5 μm. (c-d) Organelles resolved in the virtual 2D slices (contrast inverted). (c) Vesicles. (d) Liposomes. (e) Nucleus. (f-h) Bright field STEM imaging of a 70 nm thick resin-section of cheek cell. (f) Vesicles. (g) Liposomes. (h) Nucleus. Scale bar: 1 μm for (c-d), (f-g); 5 μm for (e) and (h). **66**

Figure 2.6 Subliming ice crystals at ultra-high vacuum electron microscope chamber. (a) Ice crystals (arrows) formed during sample repositioning and kept stable at -164°C inside the electron microscope chamber. Scale bar: 5 μm. (b) Increased the temperature to -100°C for 20 min, the ice sublimed without damaging the sample. **68**

Figure 2.7 Comparing sample morphology before and after dual-tilt series collection. (a) Before the first tilt series collection. (b) After the second tilt series collection. In both images, the sample was oriented at 0° tilt. The second image was rotated 90° laterally to match the

orientation of the first image for direct visual comparison. Scale bar: 10 μm . (c) Overlay of the two images. Green: (a), red: (b). (d) Pairwise distances between 16 pairs of fiducial markers on the cheek cell before and after tilt series acquisition. The data were fitted to a linear function: $y = x$ **70**

Figure 3.1 Multi-scale quantification of the chromatin organization through ChromSTEM. The ChromSTEM platform includes several experimental techniques to assess chromatin 3D organization by directly measuring the chromatin mass scaling, chromatin volume concentration (CVC), the average and the variance of DNA concentration, the mass scaling exponent (D), and the distance to the nuclear membrane. To estimate chromatin connectivity and accessibility, a 3D tomography reconstruction of semi-thick samples ($\sim >100$ nm thick) can be deployed. The analysis of the spatial distribution of the chromatin throughout the nucleus is achieved by ChromSTEM mapping of a stack of ultrathin sections (~ 30 nm). Both tomography and thin section projection can be employed to measure chromatin heterogeneity. **77**

Figure 3.2 Partially photo-oxidized nucleus. The boundary of the labeled regions matches the geometry of the laser spot. **80**

Figure 3.3 Different in staining A549 cell by varying photo-bleaching time. To test the consistency of photo-bleaching, we experimented the process with different illumination time. (a) Photobleaching for 7 min (blue square) and for 15 min (red square). The resulting staining is significantly more substantial in the long photo-bleaching spot. (b) STEM HAADF image (contrast inverted) of the 30 nm section for one cell in the 7 min spot. Scale bar: 2 μm . (c) A TEM image of the 30 nm section for one cell in the 15 min spot. For the TEM images, we first

converted the image contrast to mass-thickness using Beer's law, then calculated the average DNA concentration, and normalized the histogram to the same range as the STEM image. (d) Comparison of the histogram of the average DNA concentration for one cell in the 7 min spot (solid blue line) and three cells in the 15 min spot (red dash lines). We observed that the average DNA concentration of the 7 min cell lied in the range of the 15 min cells. Considering cell to cell variations, we concluded that within the time frame, there is no significant influence of the length of photo-bleaching in the analysis of the chromatin packing. 81

Figure 3.4 Tomography region before and after dual-tilt series collection. (a) The chromatin region before the first tilt-series acquisition. (b) The same region after the second tilt-series acquisition. Scale bar: 200 nm. (c) Overlay of the two images. Green: (a). Red: (b). (d) Fiducial pairwise distances before and after tomography acquisition. 83

Figure 3.5 Orthogonal views of chromatin after tomography reconstruction of an A549 cell. In the tomography experiment and reconstruction, dual-tilt and penalized maximum likelihood algorithm were employed to suppress the artifacts introduced by the missing cone. In the X-Z and Y-Z plane, the "X" shaped artifacts can still be seen in the tomograms, but the individual nucleosomes can be easily identified, and the stretch in the Z direction is not severe. The quality of this tomography is not as high as the ones used in Ou's ChromEMT work, as only two axes were used in our work but eight in his work. However, based on the CVC analysis, our tomography exhibits an almost identical histogram like the one shown in Ou's paper, indicating our tomography has sufficient quality for studying the local chromatin packing for 100 nm super-voxels. 85

Figure 3.6 ChromSTEM tomography reconstruction of the chromatin of an A549 cell. (a-b) The DRAQ5 photo-oxidation process takes 7 min for each region of interest. Scale bar: 10 μm . (c) The labeled regions were more stained than the nearby regions (red squares; the letter corresponds to the regions in the left panels). Scale bar: 20 μm . (d) STEM image of A549 cell in HAADF mode. Scale bar: 2 μm . (e) Schematics for dual-tilt tomography. The sample was tilted from -60° to 60° with 2° increment on two perpendicular axes. (f) 3D rendering of the chromatin organization, the pseudo color was based on the intensity of the tomograms. (g) A magnified view of the region labeled by a white square in (f). In (g), pink and green represent high and low DNA density regions, respectively. (h) 3D tomography of the A549 chromatin. Scale bar: 120 nm. (i-l) The fine structure of the chromatin chain: Nucleosomes (blue arrows in (i)), linker DNA (blue arrows in (j)) supranucleosomal stack (red dashed line in (k)) and ring (red dashed circle in (l)). Scale bar: 30nm..... **87**

Figure 3.7 ChromSTEM of mouse tissue biopsy. We modified the original protocol for cultured cells to tissue samples. Semi-thin agarose sections of the tissue were prepared, and DRAQ5 was employed to label the double strand DNA specifically. (a) Fluorescence image of a 40 μm thick agarose section during photo-oxidation. Scale bar: 100 μm . (b) After resin embedding, the photo-oxidized region was clearly identifiable due to dark contrast. The red dashed line marked the region with photo-oxidation. Scale bar: 200 μm . (c-j) STEM imaging of the tissue prepared by ChromSTEM on a 120 μm resin section. Different morphologies of the tissue bed were preserved, and four types of commonly seen cell types in the ovary were observed. Scale bar: (c-e) 5 μm , (f-j) 2 μm **90**

Figure 3.8 The internal structure of chromatin packing domains. (a) STEM HAADF image of an A549 cell nucleus shows that the chromatin is organized into compartments (light and dark image contrast), which consist of smaller domains (insets). Scale bar: 1 μm ; inset scale bar: 300 nm. (b) For each virtual 2D slice, automatic thresholding was applied to create a binary chromatin mask. The mass scaling analysis was performed inside a circle with a radius of 300 nm. Scale bar: 120 nm. (c-d) Examples of the mass scaling curve for chromatin regions highlighted by red circles c and d in (b). In (c-d), Mass is defined as the mass of chromatin that is enclosed by a ring with inner radius r and the width of 2.9 nm (1 pixel). Three distinct regimes of mass scaling can be identified: the chromatin chain regime (yellow data points and regression line), the packing domain with a fractal internal structure (blue), and the supradomain structure (red). The fractal dimension (D) and the radial size (R_f , defined as the upper length scale of fractality) of domains varied across domains. (e) The average mass scaling of 4096 randomly centered regions on each of the 33 tomograms. The error bar is the standard deviation. Three regimes of mass-scaling behavior can be identified: the chromatin chain regime (yellow) with $r < 8.7$ nm, fractal regime (blue) with the average fractal dimension $D = 2.6$ and $8.7 \text{ nm} < r < 50 \text{ nm}$, space-filling regime of spatially uncorrelated packing domains (red) with scaling exponent = 3 and $r > 100$ nm. In between the fractal region and space-filling region ranging from 50 nm to 100 nm (purple), we observed a smooth increase of the scaling exponent, which indicates variability in packing domains sizes. (f) Schematic of the packing structure of chromatin that is suggested by the ChromSTEM data. The schematic shows 9 chromatin fractal packing domains, some of which might be formed by loop extrusion (inset) or non-loop extrusion mechanisms. We hypothesized that the chromatin is organized into

spatially uncorrelated and segregated packing domains with various sizes and fractal dimensions. While some of the domains might be spatially isolated (domains 1,2,7,9), others may interpenetrate at the domain periphery as a result of decreasing chromatin density (domains 3 and 6, 5 and 8). For both configurations, the mass scaling outside of the domain is the same as the dimensionality of the space the chromatin is embedded in, 3. 93

Figure 3.9 Mass-scaling and density scaling. (a) The mass scaling of the fractal region was calculated as described. The density distribution was the unit mass on the ring with inner radius r and bandwidth of 2.9 nm (1 pixel). (b) The mass scaling and unit ring mass (density) for the mask in (a). Two transitions are present. In $r < 14.5$ region, the density decreases following a power law. In $14.5 \text{ nm} < r < 55.1 \text{ nm}$, the density keeps dropping but with oscillations but overall following the same scaling as expected from a mass fractal. At $r = 55.1 \text{ nm}$, the density increases sharply. In $r > 55.1 \text{ nm}$, the density oscillates but maintains the baseline. This behavior indicates the interpenetration of the domains..... 96

Figure 3.10 Influence of projection at varying thicknesses to the average and the standard deviation of the DNA concentration. We projected various numbers of the virtual 2D slices after tomography reconstruction to form “projections” and calculated the 2D average and the 2D standard deviation (STDEV) of DNA concentration using a 2D window with 95.7 nm on each side. For each projection (thickness), the 3D average and the 3D STDEV were calculated using a 3D window with 95.7 nm in x and y and the thickness of the projection in Z . In theory, the 2D and the 3D average of DNA concentration should remain the same, while the 2D STDEV will be a non-monotonic underestimation of the 3D STDEV. (a) We coded the 2D metrics magenta and the 3D metric green and overlaid them for different thickness. For

each pixel, a perfect match of the two will result in black and white contrast; a mismatch will result in colored contrast. As expected, for all thickness, the average from 2D and 3D window matched perfectly. While for STDEV, the mismatch increases rapidly as the thickness of projection increases. (b) The STDEV calculated from the 2D window on the projection was plotted against the STDEV calculated from the 3D window on the tomography to quantify the extent of underestimation given this chromatin structure at different thicknesses. From 8.7 nm to 95.7 nm, the ratio of 2D STDEV to 3D STDEV kept decreasing, indicating at a larger thickness, the STDEV is more severely underestimated. Meanwhile, the spread of the curve at larger thickness is also significantly wider, indicating non-monotonic, irreversible smearing of the STDEV. However, at small thickness (ultra-thin section) such as 8.7 nm, the slope is 1, and the spread is minimal, indicating almost no smearing of the STDEV. For 26.1 nm projection, the slope is 0.9 with a r^2 equals to 0.99 in the linear regression, suggesting that the STDEV from the projection is sufficiently accurate to serve as the proxy of the real STDEV from tomography with a pre-factor difference..... **98**

Figure 3.11 Alignment of the tomography region to the whole nucleus and the normalization of the average DNA concentration of A549 cells. To quantify the DNA concentration for the entire nucleus, the tomography region was registered to the whole nucleus using cross correlation with openCV2 packing in Python, and the average DNA concentration calculated from the whole nucleus image was normalized to the average DNA concentration calculated directly from the tomography. (a) A larger ROI (blue square) including the tomography region, was selected for the automatic registration. Scale bar: 2 μ m. (b) The tomography region (red square) was registered to the ROI. Scale bar: 500 nm. (c) Overlay the tomography region (red

square) and the ROI (blue square) onto the whole nucleus image. Scale bar: 2 μm . (d) The histogram of the average DNA concentration of the tomography region but calculated from the whole cell projection (orange) was normalized to the average DNA concentration calculated from the tomography (blue). The coefficients were used to normalize the DNA concentration for the whole nucleus. We observed small discrepancies for the average DNA concentration calculated from the tomography and projection even after normalization. We believe the difference in noise level at two image condition might be the reason. Importantly, the majority of the histograms match perfectly..... **100**

Figure 3.12 Chromatin is organized into spatially separated nanoscale packing domains. (a) The average DNA concentration and (b) the variance of DNA concentration both show chromatin packing domains. Scale bar: 100 nm for (a,b,h,i). (c) The diameters of the domains were estimated as the full width at half maximum (HWHF) fitted from the line profile across the domain (blue line in (a) and red line in (b)). (d) Box plot of the domain diameter measured based on the maps of the average and the variance of DNA concentration. Histograms of (e) the average DNA concentration, (f) the variance of the DNA concentration, and (g) the CVC. (h) The map of the DNA content fraction defined as the ratio of the local average DNA concentration and the CVC. (i) The fractal dimension D for packing domains identified in (a). (j) We identified two distinct states of chromatin packing with differential DNA content fraction (DNA rich vs. DNA poor domains). Redline: the linear regression of the entire dataset. DNA content fraction state I (blue) lies below the regression line, indicating low DNA fraction. State II (red) lies above the regression line, indicating high DNA fraction. The dashed line represents the 95% confidence interval of the linear regression. (k) Segmentation of

chromatin based on DNA fraction. Chromatin regions with low DNA fraction (blue) and high DNA fraction (red) in (k) correspond to states I and II in (j), respectively. From the mass-scaling curve for each of the 43 domains segmented by watershed algorithm from (a), we quantified the fractal dimension (l) and fractal domain radius (m). **103**

Figure 3.13 Comparing cluster boundaries in the DNA concentration and the DNA concentration / CVC. To investigate the spatial distribution of cluster identified independently in the DNA concentration map (left) and the DNA concentration/CVC ratio map (middle), we overlaid the two maps with false coloring (right). In the overlay image, the magenta denotes the DNA concentration, and the green represents the DNA concentration/CVC ratio. Qualitatively, the clusters have similar boundaries and spatial distribution. However, the cluster with high DNA concentration can have an arbitrary value of DNA concentration/CVC ratio, which leads to low pixel-to-pixel cross-correlation coefficient (-0.13). **106**

Figure 3.14 STORM of A549 to quantify heterochromatin volume concentration. To quantify the average volume percentage of heterochromatin for A549 cell, the H3K9me3 and anti-H3K27me3 were labeled, and STORM images were taken for multiple cells. The ratio of pixels with signal and total pixels of the nucleus was used to represent the average heterochromatin volume percentage. (a) and (b) Examples of STORM images with 43.8% and 54.2% heterochromatin, scale bar: 3 μ m. (c) Distribution of heterochromatin volume percentage for 4 cells at in total 10 different focal planes, the average heterochromatin volume concentration is calculated to be 47% and used in heterochromatin segmentation from the average DNA concentration map. **108**

Figure 3.15 Packing properties of chromatin in different nuclear compartments. (a) The spatial and (b) the statistical distribution of the average DNA concentration calculated for a 30 nm section of A549 cells. Scale bar: 2 μm for (a) and (c). The nucleoli are clearly identifiable (white arrows in (a)). (c) The spatial and (d) the statistical distribution of the variance of the DNA concentration for the same sample. (e) Mask for heterochromatin segmentation based on the tomography data. Scale bar: 200 nm. (f-h) Differences in the average DNA concentration, the variance of the DNA concentration, and the CVC between euchromatin (blue) and heterochromatin (orange). (i) Mask for heterochromatin segmentation for the cell in (a), the nucleoli were removed from the mask. Scale bar: 3 μm . (j-l) Differences in the average DNA concentration, the variance of the DNA concentration, and the distance to the nuclear envelope between euchromatin (blue) and heterochromatin (orange). **110**

Figure 3.16 Differences in DNA concentration between euchromatin and heterochromatin of cells in the mouse ovary. (a-e) Neighboring cells in the mouse ovary tissue processed with the ChromEM staining. Scale bar: 1 μm . (f) The average DNA concentration for each cell (blue area) and the mean DNA concentration of the five cells (red line). (g) The most probable DNA concentration for euchromatin and heterochromatin. (h) The distribution of the ratio between the most probable DNA concentration within heterochromatin (He) and euchromatin (Eu) in each cell. On average, DNA concentration in heterochromatin is 2.4 times higher than that in euchromatin. **112**

Figure 4.1 Comparison between workflows calculating ACF using the conventional method and the method in this paper. As only one EM image is required in the proposed method, the experimental time and beam damage will be greatly reduced. The resolution of ACF from the

new method is not constrained by Crowther's criterion. In addition to assuming the sample is isotropic, the proposed method also assumes the sample thickness is uniform within the region of interests. However, the error introduced by this assumption is not significant for most biological samples. **120**

Figure 4.2 Statistically isotropic and anisotropic medium. (a) An isotropic sample with (c) ACF along all direction identical. (b) An anisotropic sample with (d) ACF different along z- and x-axis. Scale bar: 2 μm **124**

Figure 4.3 Calculation of projected mass in a specific pixel area. (a) R is the radius of the bead, which can be measured as the diameter of the projected circle. r is the distance of the pixel to the center of the circle. d is the thickness of the beads projected to the pixel, $d = 2\sqrt{R^2 - r^2}$. (b) A HAADF image of a polystyrene bead taken under low projection lens current. Scale bar: 1 μm . (c) The radial distance of different pixels to the center of the polystyrene bead. The intensity of pixels in the same band is averaged. The region with non-polystyrene material was not considered and resulted in a "wedge". (d) The intensity over mass plot and linear fitting of the bead shown in (b). **127**

Figure 4.4 AFM experiment flow-chart. (a) We first registered TE image to SE image by cross-correlation, then we registered nucleus to SE image. Scale bar: 10 μm . (b) A small area of features was scanned with low resolution and registered to the SE image. Scale bar: 3 μm . (c) Position of the AFM probe (red dot position 1) while scanning (b), (b) was overlaid on the SE image. Position of the probe while scanning the nucleus (blue dot position 2), and position of the probe while scanning the reference (yellow dot position 3) Scale bar: 10 μm **130**

Figure 4.5 STEM images of the same cheek cell. (a) HAADF image of the entire cell. Scale bar:

20 μm . (b) Nucleus region of the same cell. Scale bar: 3 μm **131**

Figure 4.6 Regional thickness distribution measured by AFM. (a) AFM measurement on a large

area as reference height. (b) AFM measurement performed on a smaller region enclosing the

nucleus, with a lateral resolution of 11 nm to reveal the fine topographic detail. (c) The relative

position of the two images. Scale bar: (a) 3 μm , (b) 50 nm, (c) 10 μm **132**

Figure 4.7 Cheek cell mass-density distribution. (a) 2D mass-density projection, scale bar: 1 μm .

(b) ACF of (a) and (c) reconstructed 3D mass-density ACF of (b). **133**

Figure 5.1 Examples of different types of beam-induced morphological changes. (a) and (b), TEM

images of the same cell that experienced materials loss due to radiolysis. In (a) red line

highlighted the beginning of thinning in the sample. Compared to other parts of the sample,

the damaged area appears lighter, indicating less mass. Scale bar: 2 μm . In (b), the beam

damaged area expanded. Radiolysis is the primary form of beam damage for the biological

sample. (c) and (d), STEM HAADF images of the same lipids-iron nanoparticle construction

that experienced the redeposition of hydrocarbons. After prolonged illumination (~1hr),

contamination layer formed on the sample in (c) and created a “core-shell” structure in (e-g).

The contamination was highlighted by the arrows in (e-g). Scale bar: 100 nm in (c). **138**

Figure 5.2 Reconstruction (lower panel) from sparsely sampled projection images (middle panel)

under STEM HAADF mode. The sparsely sampled images were simulated from the ground

truth (top panel) by randomly selecting pixels. The number of pixels samples varies in each

column. 20% and above sampling rate provides enough information for the nonparametric

Bayesian dictionary learning inpainting method BPFA to recover the full image faithfully for this particular sample. 141

Figure 5.4 Sampling scheme and workflow of CORT. In CORT, the sample rotates non-stop during imaging. To process CORT data, pixels collected at the same sample orientation will be sorted and placed in the same image frame. The undersampled sinogram will be inpainted, and the recovered sinogram will be used in tomography reconstruction. 147

Figure 5.5 Effects of angular averaging in each pixel. Images reconstructed from tilt series with and without averaging of varying window sizes were compared with the ground truth. The reconstructed image from tilt series without averaging shows lower MSE and higher PSNR, indicating it is closer to the ground truth from pixel values. However, the SSIM graph indicates that the image from tilt series with averaging is structural more similar to the ground truth at small averaging windows. 149

Figure 5.6 CORT data presentation as raw data, sorted projection, and sinogram. (a) The projection images of a double-walled carbon nano-tube with silver particles at different tilt angles (0° , 60° , 120° , 180°). (b) CORT raw data of 31 frames. As the sample is continuously rotated, the traditional tilt angle does not apply here. (c) Sorted CORT data can form undersampled traditional projection image at different tilt angles (0° , 60° , 120° , 180°). (d) The sorted projection can be rotated and resliced to create undersampled sinogram of the sample (top, middle, bottom)..... 151

Figure 5.7 Influence of the sample rotation speed to the mask of visited pixels in the sinogram. For the same 31 CORT frame with the same pixel dwell time, the rotation speed of the sample drastically changed the sampling mask in the sinogram. Compared to the fully sampled

sinogram, the faster the sample rotates, the more even the pixels visited can distribute through the image. However, notice that at $v = 67^\circ/\text{s}$, there is a sizable void with no pixels sampled. Due to the periodicity in equation 5.1, for some special cases, the high speed does not guarantee even distribution. **153**

Figure 5.8 Performance of CORT on reconstructing a double-walled carbon nanotube with silver nanoparticles. (a) Fully sampled sinogram. (b) Fully-sample projection image. (c) One virtual 2D slice of the tomogram reconstructed from the fully sampled tilt series. (d) Inpainted sinogram from CORT data. (e) Resliced projection image from inpainted sinogram from CORT data. (d) One virtual 2D slice of the tomogram reconstructed from CORT data. (g) SSIM of the tomography reconstructed from fully-sample tilt series and CORT. (h) Pixel-to-pixel cross-correlation between the tomography reconstructed from fully-sample tilt series and CORT. **156**

Figure 5.9 CORT data presentation as raw data, sorted projection, and sinogram for a human cheek cell. (a) The fully sampled projection images of a human cheek cell at different tilt angles (0° , 60° , 120° , 180°). (b) CORT raw data of 31 frames. In each frame, the pixels were oriented at different angles. (c) Sorted CORT data can form undersampled traditional projection image at different tilt angles (0° , 60° , 120° , 180°). (d) The sorted projection can be rotated and resliced to create undersampled sinogram of the sample (top, middle, bottom). **157**

Figure 5.10 Performance of CORT on reconstructing a human cheek cell. (a) Fully sampled sinogram. (b) Fully-sample projection image. (c) One virtual 2D slice of the tomogram reconstructed from the fully sampled tilt series. (d) Inpainted sinogram from CORT data. (e) Resliced projection image from inpainted sinogram from CORT data. (d) One virtual 2D slice

of the tomogram reconstructed from CORT data. (g) SSIM of the tomography reconstructed from fully-sample tilt series and CORT. (h) Pixel-to-pixel cross-correlation between the tomography reconstructed from fully-sample tilt series and CORT..... **160**

Figure 6.1 Validation of SICLON resolution by AFM. (a) STORM reconstruction of DNA fiber using 532 nm illumination. (b) SICLON reconstruction of DNA fiber after applying the SR algorithm. (c) AFM measurement of a separate single DNA fiber. (d) Comparison of resolution between traditional PLM and SICLON with SR shows a 4X resolution enhancement. (e) AFM reveals that the ground truth width of the fiber is estimated to be 4.1 nm..... **165**

Figure 6.2 Quantifying chromatin structure from SICLON images by correlation dimension D_c . (a) SICLON image of chromatin of an isolated nucleus. Scale bar: 2 μm . The number of pairs of points with a mutual distance smaller than r as a function of r . The log-log plot showed a linear region, indicating a fractal internal structure. The correlation dimension was 1.41 from the slope of the linear regression..... **167**

Figure 6.3 Quantifying chromatin alterations in wildtype and chemo-resistant ovarian cancer cell lines (A2780). (a) and (b), PWS measurement of the A2780 wildtype and the strand with chemo-resistance mutation. Scale bar: 15 μm . (c) and (d), SICLON image of the A780 wildtype and chemo-resistant mutation. Scale bar: 10 μm . The cytoplasm was shaded with a gray mask, and the nuclei were labeled. (e) The PWS measurement and (d) Correlation dimension from SICLON for the chromatin in A2780 wildtype and chemo-resistant mutation. In both modules, the chromatin heterogeneity of the chemo-resistant mutation was significantly more considerable than that of the wildtype. **169**

Figure 6.4 Examples of the multi-technique nanoimaging and computational transcriptomics platform. The multi-technique platform consists of three parts: nanoimaging to directly visualize chromatin packing at all length scales (5 nm to 200 μm); multi-scale computational analysis to investigate the underlying physics behind chromatin structure; Hi-C characterization to provide big data for high-statistical power analysis across the entire genome over different cells lines and conditions. Top panel, from left to right: 1. Ultra-high-resolution scanning transmission electron tomography at 3 nm resolution for 3D chromatin structure in mammalian cells. Scale bar: 30 nm. 2. High throughput TEM imaging of 50 nm slice of BJ cell nucleus. Scale bar: 1 μm . 3. PWS (red) and super-resolution STORM (green) co-registered imaging of chromatin scaling and Pol II. Scale bar: 3 μm . 4. Label-free PWS image of live HeLa cells. Pseudo-color: DPWS with sensitivity from 20 to 350 nm. Scale bar: 20 μm **175**

Figure 6.5 Chromatin packing exhibits mass fractal structures in multiple length scales. (a) A pseudo-2D cross-section (2.9 nm in thickness) of A549 cell nucleus chromatin after 3D STEM HAADF tomography reconstruction (contrast inverted). Scale bar: 200 nm. (b-c) The STEM tomography has a nominal resolution of 2.9 nm and is capable of resolving individual nucleosomes and linker DNAs in the pseudo-2D cross sections. Scale bar: 20 nm. (d) Average 2D ACF of 33 chromatin cross sections plotted in log-log scale. Three linear regions were identified on the curve belonging to different topologies in chromatin packing: nucleosome region (0 to 11.6 nm), pure mass fractal region (11.6 nm to 58 nm), chromatin interpenetrating region (58 nm to 145 nm). The ACF analysis provided experimental evidence that chromatin is a mass fractal structure in certain length scales. (e) The moving average chromatin volume

concentration (CVC) map showed spatially separated packing domains with a diameter of around 100 nm. (f) The fractal map overlaid with CVC map. Each fractal domain can contain multiple CVC domains. (g) The mass fractal dimension D_{MS} and CVC showed a positive correlation. **181**

Figure 6.6 Measuring chromatin packing scaling alterations induced by dexamethasone in A549 cells. (a-b) Multi-platform characterization of A549 chromatin with and without DXM treatment. From left to right: TEM images of the chromatin structure with ChromEM staining, scale bar: 1 μ m. Hi-C contact map of the entire genome. The red square highlighted the regions with contact probability analysis. PWS map of the chromatin packing scaling, the black circle highlighted the nucleus. Qualitatively, from both TEM and PWS, after the DXM treatment, the chromatin packing became more homogeneous. (c) ACF analysis using TEM images of A549 chromatins. The average ACF of the control group (blue) is significantly different from the average ACF of the treated group (red). The shades indicate standard errors. The chromatin fractal dimension was measured inside the first fractal domain (20 nm to 54 nm) by linear fitting the ACF in log-log scale (dashed lines). (d) Contact probability analysis using the Hi-C contact map between 60 kb and 0.3 Mb bp. The power law scaling s was quantified by linear regression (dotted line). (e–g) Chromatin packing scaling alterations induced by DXM treatment measured using ACF analysis of TEM images, contact probability analysis of Hi-C maps, and PWS. Across the platform, consistent changes were observed in chromatin packing. **185**

Figure 6.7 Measuring chromatin packing scaling alterations induced by dexamethasone in BJ cells. (a) Characterizing the chromatin packing at three different time points (0hr, 16hr, 32hr)

after introducing DXM via the multi-technique platform. The upper panel showed the Hi-C results, and the bottom panel showed the PWS maps. In the PWS maps, the cell nucleus was highlighted by the black circle. The PWS signal continued to drop as we extend the treatment time. The TEM images of the BJ cells in the control group (b) also showed more heterogeneous chromatin distribution than the treated group after 32 hours (c). Scale bar: 1 μ m. (d) ACF analysis of the TEM images, the fractal dimension was calculated by linear regression (dashed lines) of the ACF curve in between 20 nm to 54 nm. (e) The contact probability analysis of the Hi-C map, the power law scaling s was quantified by linear regression (dashed lines). (f-h) Fractal dimension quantified across the multi-technique platform. For ChromEM, only the control group and the 32 hr treatment were analyzed. In all modalities, we observed a consistent decreasing of D after the DXM treatment. **189**

Figure 6.8 Workflow of cSRAEM. Prior to STORM imaging, a low magnification transmission image was taken using an optical microscope which was used as a roadmap together with the STORM fluorescent image (FL) to assist locating the same cells in the photo-oxidation. The arrows pointed to the same cell in the transmission image and the fluorescent image taken during the photo-oxidation. Scale bar: 5 μ m. After resin-embedding, serial sections, with 120 nm in thickness for each section, were prepared by ultramicrotomy. For this cell, 60 sections were made. TEM was performed on each section in sequence, and the images were aligned in IMOD for tomography reconstruction. **194**

Figure 6.9 cSRAEM on an A2780 cell with RNA PolII labeling for STORM and ChromEM DNA labeling for EM. (a) Projection view of the 3D STORM reconstruction. Scale bar: 5 μ m. (b) The side view of the 3D STORM reconstruction. For both (a) and (b), the color represents a

different focal plane during acquisition. (c-e) TEM images of the top, middle, and bottom slice of the same cell. Scale bar: 2 μm **195**

LIST OF TABLES

Table 4.1 Camera length, inner and outer semi-collection angle at different projection lens current	126
---	------------

CHAPTER 1 INTRODUCTION

1.1 Philosophy and Approach

Gene transcription is crucial in maintaining all aspects of cell functions, including replication, differentiation, controlled apoptosis, to name a few. Although the genetic information is directly coded in DNA in the form of nucleotide sequences, the regulation of the gene transcription is controlled by the genome organization. It is the primary goal in epigenomics to investigate the biological, chemical, and physical properties of the genome organization. Rapid advances in the technologies regarding chromatin labeling and imaging with ever-finer resolution in both electron microscopy and super-resolution microscopy have enabled us to explore the physical structure of the genome organization with unprecedented details. To take advantage of this chance to interrogate some of the most complicated questions in the chromatin study has required the integration of a diverse set of colleagues, from microscopy and biomedical engineering to more traditional polymer physics and molecular biology.

The goal of this introductory chapter is two-fold: first, to give an general background to the field of epigenomics with emphasis on the importance of understanding the physical aspects of genome with higher resolution for larger volume; and second, to give non-imaging experts a brief introduction of the strengths and challenges of modern electron microscopy and how it can be utilized to provide insights on the chromatin ultrastructure. The introduction chapter will review the challenges of using electron microscopy to investigate chromatin in mammalian cells specifically, which will be reintroduced in the following chapters when relevant for the major developments and proposals in this thesis.

1.2 Introduction to 3D Genome Organization

1.2.1 3D Genome Organization in Regulating Gene Transcription

The human genome is a complicated system with intrinsic three-dimensional (3D) spatial organizations that are evolving constantly. Our current understanding of the physical structure of the genome, the chromatin, can be dictated by a hierarchical structure, which is also updating with the development of advanced microscopy. At its smallest length-scale (3.4 pm to 2 nm), the chromatin is fundamentally composed of nucleic acid base pairs (bp, or nucleotides) joining together into a primary double-helix structure: DNA. The DNA, which contains the primary genetic sequence for protein, is coiled into 147-bps units around histone proteins to form 11 nm wide, 5 nm thick, disk-like nucleosomes^{1,2}. The nucleosomes are next linked into the “beads on a string” by the linker DNAs. Above 200 nm, chromosomal territories with distinct morphology inside the nucleus are observed across cell types and species³. In between 10 nm to 200 nm, the linear configuration folds into more complex 3D structures, but little is known about neither the details of the spatial topology nor the folding mechanisms.

Gene transcription regulation across these broad length scales of chromatin structures includes both molecular regulators such as DNA methylation, promoter-enhancer interaction, and physiochemical regulators, such as electrochemical shielding and divalent cation distributions⁴⁻⁶. Importantly, the controlled transcription of a specific group of genes at certain rates and times is the result of coordinated communication between many neighboring and distal elements, all of which are located in a highly dense chromatin nanoenvironment within the cell nucleus. In turn, the nanoenvironment depends on chromatin packing directly, which acts through physical forces

and shapes the genomic information landscape^{7,8}. In particular, it has been shown that the chromatin packing-density heterogeneity at length scales from ~20 nm to 350 nm (kbp to Mbp genomic range) can modulate transcriptional diversity, intercellular transcriptional heterogeneity, and gene network heterogeneity⁹.

1.2.2 Techniques to Investigate 3D Genome Organization

Sequencing techniques, such as assays for transposase-accessible chromatin using sequencing (ATAC-seq) and Chromatin Immuno-Precipitation sequencing (CHIP-seq), have been dominating the study of the molecular regulator of chromatin topology at the level of nucleosomes (“histone code”) and primary sequence (“genomic code”)¹⁰⁻¹². These techniques, in combination with gene expression quantifications, as provided by mRNA microarray or RNA-seq, allow correlational investigation of the regulators of transcription¹³.

At the level of supra-nucleosomal organization, in the last 20 years, the field considering chromatin architecture has benefited from explorations with the combination of targeted chemistry, molecular dynamics modeling, and especially, high throughput quantitative sequencing¹⁴. Among all, the chromatin conformation capture-based (3C-based) techniques, including 3C, 4C, 5C, and Hi-C, have indeed extended our knowledge towards the spatial chromatin organization by measuring the frequency of physical interactions or proximity among any pairs of genomic loci¹⁵⁻¹⁷. Particularly, the finding of cell-type invariant, evolutionarily conserved, sub-megabase scale domains, TADs, in a broad spectrum of cell types has provided a new molecular framework for the study of chromatin structure-function relation¹⁸. Traditionally,

the C-based techniques assess the organization of the entire genome from millions of cells, but the structural information describing individual cell variability is missing because the pairs of ligated sequences that are recorded have a vanishingly small chance of coming from the same chromosome or the same cell. C-based analysis can provide a super-imposition of the ensemble of genome conformations, rather than one stable individual structure. The single-cell Hi-C will potentially provide a solution to differentiate the inter-cellular heterogeneity, but the intra-cellular information is lost, as digestion of the cell is still a critical step¹⁹.

Recently, microscopy-based techniques have been regaining popularity in order to address the challenges imposed by the limitations of current C-based techniques and providing insights to some long-standing questions such as the inheritability of genome organization during cell differentiation at single-cell level. Importantly, the advances in pushing the resolution limit of optical microscopy have provided invaluable tools to investigate the chromatin organization with unseen details with applications in live cells²⁰⁻²². Notably, the combination of custom oligonucleotide arrays such as Oligopaint and novel super-resolution microscopy approaches such as STORM and PALM have enabled the direct visualization of the chromatin fiber and different groups of nuclear bodies at single-cell level, and has been further employed to reveal the power-law relationship between the chromatin physical volume and genomic length at different epigenetic states in active, inactive, and Polycomb-repressed domains for *Drosophila melanogaster*²³. Furthermore, early success has been reported to generate “Hi-C” like contact probability maps from STORM images for single-cell nuclei²³. In the pursuit of chromatin heterogeneity imaging for living cells with real-time tracking ability, Partial Wave Spectroscopy (PWS) Microscopy stands out. Due to its ability to measure the nanoscopic chromatin packing

density with sensitivity to chromatin organizations between 20 and 350 nm in live cells, PWS has been employed to monitor the chromatin alterations during chemotherapy, UV radiation, ionic environment changes, and cell differentiation²⁴⁻²⁶.

However, all the optical microscopy-based techniques have a practical limitation on spatial resolution (~20 nm). Electron microscopy, due to its superior resolution, has a unique role in bridging the gap between individual nucleosome (~10 nm) and linker DNA (~2 nm) and the optical resolution limit. From conventional TEM for ultrastructural imaging to cryo-EM for single particle reconstruction, electron microscopy has been widely applied to investigate the morphological and chemical properties for features with length scales ranging from single virus to protein to organelle and the entire organ²⁷⁻³⁰. In particular, the ChromEMT method, which utilizes a DNA specific labeling protocol (“Click-EM”) and TEM tomography, has achieved a 1.6 nm voxel resolution and resolved individual nucleosomes and linker DNAs in the interphasic and mitotic nuclei³¹. The findings from the ChromEMT experiments suggest that the chromatin polymer is a disordered chain with 5 to 24 nm in diameter packed together at different densities throughout the nucleus³². Due to its superior resolution and full 3D imaging capability, electron microscopy has the potential to answer some of the most complicated questions in the field of chromatin organization related to phase-separation and supercoiling³³⁻³⁶.

1.3 A General Introduction to Modern Electron Microscopy

Electron microscopy has emerged as the technique of choice in terms of investigating and understanding ultrastructure over a wide span of subjects in including energy storage and

conversion materials, semiconductors, and biological samples³⁷⁻⁴². Thanks to the sub-atomic wavelength of high energy electrons, electron microscopy has provided information of structures at pico-meter resolution^{43,44}. This resolution advantage comes with a set of strict requirements for the nature of the samples: they must be physically and chemically stable in a vacuum, processable into a thin electron transparent film, interact with electrons to provide image contrast, and resistant to the electron beam⁴³. Biological samples, in particular, which exist fundamentally without these properties, can be quite challenging to prepare and investigate.

Based on the geometry of the incident electron beam, we can classify the electron microscope into two significant categories: transmission electron microscope (TEM) with a nearly parallel beam and scanning transmission electron microscope (STEM) with a convergent beam. In both TEM and STEM, the electrons are accelerated at high voltage (hundreds of kilovolts) to achieve high incident energy to travel through the sample so that enough electrons can reach the detectors located at the back side of the specimen.

In TEM, an electron micro- or nano-probe illuminates and interact with a small area of the sample. Electrons that are elastically and inelastically scattered within the aperture can be recorded on the post-specimen camera to form a static image. Most images have a phase contrast component, and two methods are primarily used to generate such contrast: Scherzer focusing and defocusing contrast. On the one hand, the defocusing contrast is proportional to the Laplacian of the projected charge density for a pure phase object⁴⁵. On the other hand, the Scherzer focusing relies upon a careful balancing of negative defocus settings to provide a stationary phase condition that allows the introduction of desired phase shifts to eliminate the imaginary component⁴⁶. Another approach to generate phase contrast is to use electron holography. This technique uses a

highly coherent field emission electron source and a beam splitter to create an interferogram, or hologram, of the electron wavefield⁴⁷. Considerable efforts have been expended on the development of phase recovery methods⁴⁸. However, due to beam instability during data acquisition and lacking prior knowledge of non-periodic biological structures, these methods have some difficulties to reliably provide unambiguous, quantitative reconstructions.

In STEM, a convergent nano- or pico-scale probe is focused on the sample and rastered to form an image^{49,50}. Typically, the electrons passing through the sample, or those that are backscattered, are integrated on annular photomultiplier tubes (PMTs) to enable accurate and high dynamic range detection⁵⁰. The inner detector produces Bright Field (BF) images using those electrons whose trajectory did not deviate significantly after interacting with the sample. On the other extreme, the High Angle Annular Dark Field detector (HAADF) integrates electrons which have been elastically scattered to large angles (Rutherford Scattering)⁵¹.

The set of electrons, non-scattered and scattered within the aperture, can be selected individually to form bright field or dark field images for TEM and STEM. As electrons traverse the specimen, the electron wave can change both its amplitude and its phase. Both types of change can give rise to image contrast: amplitude contrast and phase contrast. In most situations, both types of contrast contribute to an image, but for amorphous, thick biological samples, the mass-thickness contrast (one form of amplitude contrasts) dominates for both TEM and STEM and in both BF and DF images.

Despite similar image contrast, that STEM does not require post-specimen lenses to form an image. The resolution of TEM for thick samples is limited by the energy losses of the electrons

passing through the specimen, which cannot be focused due to the chromatic aberration of the post-specimen lenses. STEM suffers less from chromatic aberration, and improved resolution has been demonstrated for specimens in the range of 1-2 μm thickness^{52,53}. Therefore, it is suitable for imaging samples that are too thick for TEM. Ultimately, the multiple, dynamic, scattering will obscure even STEM's ability to image extremely specimens ($> 4 \mu\text{m}$).

1.3.1 Quantitative imaging Using Scanning Transmission Electron Microscopy (STEM)

Importantly, HAADF in STEM is an incoherent imaging mode where the phase-contrast cancels each other after integration⁵⁴. The contrast in HAADF is analytical and has excellent potential in quantifying the physical properties of the sample with calibration⁵⁵. The elastic scattering cross-section σ is dictated by:

$$S \sim Z^{1.7}. \quad (1.1)$$

Z is the atomic mass of the atom that interacts with the electrons, and thus HAADF imaging mode has a more popular name: Z-contrast. For more biological samples, the chemical composition is similar, and with the image resolution needed, the average atomic number for a biological sample can be viewed as constant, and the Z-contrast is directly proportional the mass-density.

As shown in Figure 1.1, a polystyrene bead was imaged using Z-contrast with varying collection angle. As we increased the semi collection angle of ADF detector, the influence of inelastic scattering was eliminated, and the image contrast is approaching perfectly linear to the total mass along the trajectories of electrons.

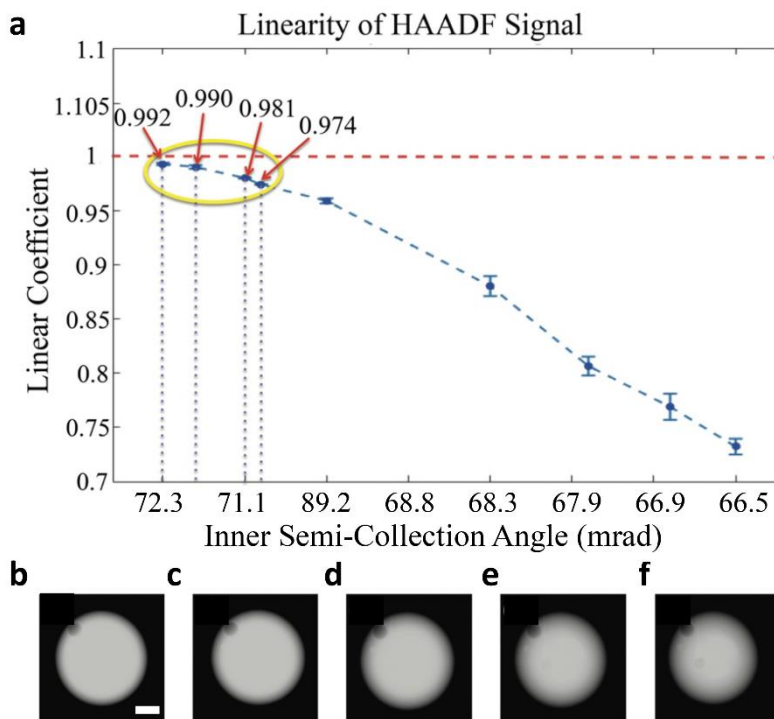


Figure 1.1 Relationship between intensity and mass in HAADF images as a function of the inner semi-collection angle. (a) Linear coefficient of intensity and mass as we change the projection lens current, the selected inner semi-collection angle is 72.3 mrad when considering linearity and signal to noise ratio. (b) to (f) HAADF image of a polystyrene bead recorded at 10K magnification from larger projection lens current to smaller projection lens current. Scale bar, 1 μm .

1.3.2 High-resolution 3D Reconstruction through Electron Tomography

Electron tomography has been a leading technique for 3D structural analysis of unique complex biological samples⁵⁶⁻⁶¹, as a 2D projection image is not interpretable due to many

superimposed densities. Sites with high-voltage EM, like Wadsworth center in Albany, NY, and the Boulder 3-D lab, made significant pioneering progress in both detector and computer software for data acquisition and 3D processing^{62,63}. Nowadays, it is feasible to directly visualize the molecular architecture of organelles, cells, and complex viruses as well as cellular dynamic events captured from the near-native state at close-to-molecular resolution⁶⁴⁻⁷¹. The resolving power of ET at multi-length-scale offer a unique potential to bridge the gap between the low resolution (medical CT, confocal microscopy, soft x-ray tomography, x-ray fluorescence tomography⁷²⁻⁷⁴) and high-resolution techniques (x-ray or electron crystallography, nuclear magnetic resonance⁷⁵⁻⁷⁷).

Similar to computed tomography, electron tomography is a computerized reconstruction method to render 3D volume of the sample from a series of 2D projection images (tilt series) at different projection angles⁷⁸. Unlike CT that the detector rotates around the patient, we tilt the sample stage while the detector stays still. The mathematical foundation of tomography reconstruction is the Fourier central slice theorem: the Fourier transform of a 2D projection of a 3D sample is the same as the 2D slice oriented at the same angle of the 3D Fourier transform of the original sample. In principle, the sample can be oriented at random direction in the tilt series, but the conventional approach is to collect tilts ranging from +/- 60° (70° for higher kV microscopes) with small and equal increment (1° or 2°). For better angular coverage, sometimes a second tilt series is taken with the specimen tilt around a second axis perpendicular to the first one⁷⁹⁻⁸¹. After collecting the tilt series, cross-correlation (fiducialless^{82,83}) and feature-tracking (fiducials^{84,85}) based alignment algorithm is employed to transform each image so that their common tilt axis is in the center of each image. The final reconstruction is usually done in real

space using Filtered Back Projection (FBP) or Simultaneous Iterative Reconstruction Technique (SIRT)⁸⁶. Recently, novel algorithms (MBIR, CS-ET, Penalized-Maximum-Likelihood⁸⁷⁻⁹¹), with constraints from *a priori* knowledge of the sample have been developed to address issues with low SNR and missing angular information. Note that both TEM and STEM can be used in ET, but STEM provides near quantitative contrast in HAADF mode with high signal-to-noise-ratio (SNR) and contrast and therefore is ideal for tomography data collection⁹².

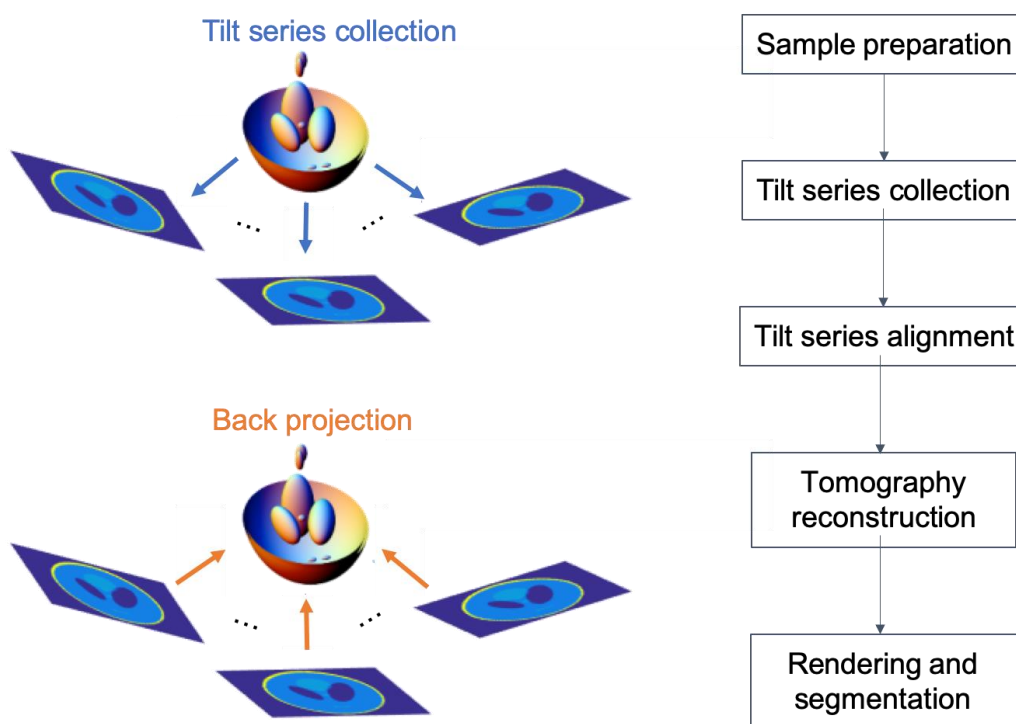


Figure 1.2 Principle and workflow of electron tomography for biological samples. The sample is generally tilted from -70° to 70° or -60° to 60° and the projection image at each tilt is collected sequentially. The tilt series is then aligned and reconstructed for 3d structure.

Volume/surface rendering can be employed to assist visualization, and image segmentation is generally performed to identify useful features.

1.3.3 Challenges of Utilizing Electron Microscopy in Characterizing Chromatin

Ultra-Thick Sample

The sample thickness suitable for imaging is determined by the material lattice structure and the energy of the incident beam. As the beam travels through the sample, the beam will be broadened due to scattering events and deteriorate the resolution and decrease the signal to noise ratio of the final image. The inelastic mean free path of a 300 keV electron in graphite is about 360 nm. As a result, the sample thickness of an EM sample is on the order of ~100 nm or less⁹³. There is some specialized EM in which the electrons are accelerated to MeV to study thick samples with thickness over 1 μ m, but the application is not wide-spread due to the trade-off between image resolution and contrast^{94,95}. For chromatin study, it is important to characterize the organization entirely along the z-direction. The thickness of a typical nucleus of a mammalian cell is about 6 μ m, orders of magnitude greater than the suitable sample thickness. Consequently, the cells are sectioned to thin slices before imaging. In the case of a whole cell reconstruction, dozens of hundreds of serial sections are collected in order⁹⁶. Despite the tremendous amount of technical challenges in performing such experiments before imaging, there are fundamental limitations on sectioning. On each section surface, artifacts associated with sample preparation such as knife marks, ridges, chatter, and crevasses are almost inevitable^{97,98}. The thinner the sections, the more surface they have, and the more likely they are to exhibit artifacts that cannot be removed in post-

processing⁹⁹. It's been reported that using scanning transmission electron microscopy (STEM), sections of biological samples of close to 1 μm has been successfully imaged in 3D, and the whole cell can be characterized only through a few iterations¹⁰⁰⁻¹⁰². However, the artifacts are likely to be introduced, and a method capable of achieving whole cell imaging without sectioning is still in demand.

Low Intrinsic Contrast and Low Staining Specificity

Chromatin, like many other biological samples, is known as a “weak phase” object. The majority of the elements (carbon, hydrogen) in the chromatin has very low electron density, which results in few electron scattering events and low contrast images. Without any staining, the chromatin can be imaged either in dehydrated form or frozen hydrated form, as there is enough density difference between the sample and surrounding (vacuum or frozen water). However, as sectioning is usually required, the cells or tissues are embedded in resin, the density difference is much lower, and electron-dense stains are indispensable to provide sufficient contrast¹⁰³⁻¹⁰⁵.

Osmium tetroxide, uranyl acetate (UA), and lead citrate are the primary contrast agents in EM for biological samples, and they can be introduced before embedding or used as post-staining. Osmium is used routinely as a fixative; it reacts with unsaturated carbon bond and primarily stains lipids¹⁰⁶. The uranyl ions bind to proteins and lipids with sialic acid carboxyl groups such as glycoproteins and ganglioside and to nucleic acid phosphate groups of DNA and RNA. Gangliosides are glycolipids and are concentrated on cell surfaces^{107,108}. Glycoproteins are abundant in all membranes and part of the glycocalyx. Therefore, UA delivers good contrasting results of membranes, nucleic acids, and nucleic acids containing protein complexes such as

ribosomes. Lead citrate interacts with reduced osmium to further enhance contrast since it allows the attachment of lead ions to the polar groups of molecules¹⁰⁹. Lead citrate also interacts, to a weaker extent, with UA and therefore lead citrate staining is employed after UA staining.

While the heavy metal solution can increase the overall image contrast significantly, the target of those labeling is ubiquitous. Unless there are distinctive morphological features, it is impossible to pinpoint cellular substance based on their molecular profile just from electron micrographs. Identifying gene function is particularly difficult as the same gene can be turned on and off based on the cell cycle, promoter-enhancer interaction, and other biochemical aspects. In the past decades, affinity probes targeting at both protein and nonprotein structures have been developed to add dimensions to the subject that electron microscopy can study. Till this day, it is still transforming our knowledge by allowing the identification of a more extensive collection of cell and tissue component¹¹⁰. Among those, immuno-gold and metabolic labeling stand out for chromatin study¹¹¹⁻¹¹⁴. In particular, ChromEMT, which labels DNA specifically, has provided solutions to a long-standing question of whether a 30 nm fiber exists as a fundamental chromatin structure³². We believe that utilizing even combining the two labeling technique has the potential to revolutionize the field and provide invaluable information in relating chromatin organization to its function in regulating gene transcription.

Beam Damage

The risk of ultrastructural damage under electron illumination is a challenge that must be acknowledged and minimized when investigating any sample. Bombarding a specimen with relativistic electrons at high current densities can quickly modify a stable specimen or move a

dynamic process out of equilibrium¹¹⁵. There are two major sources of damage when observing a material at high integrated doses. Firstly, the ionization of a sample atom by an inelastic scattering event with an incident electron. Local structure plays a crucial role in the downstream effect of inelastic scattering, as in conducting materials an additional electron can be donated quickly. In insulating materials, such as chromatin, an ionization event is much more likely to result in bond breakage and mass diffusion at room temperature. Given the enormous thickness of the cell and the need to image through thick samples, the beam damage is especially relevant: 1. the electrons have higher tendency to experience inelastic scattering along the trajectory, 2. the heat generated from inelastic scattering is more likely to be trapped inside the sample.

To reduce beam damage in chromatin imaging, one cannot simply weaken the incident beam or shorten the exposure times, as the likelihood of observing the desired elastic or inelastic scattering event on a detector or spectrometer is related to the incident beam current: the smaller the electron dose, the lower the image signal-to-noise ratio. In landmark work, Glaeser examined the effect of low-flux electron beams on the achievable information and resolution in electron micrographs of biological specimens¹¹⁶. He found that the dose limiting resolution (DLR), or the maximum resolution achievable at an accelerating voltage can be written as the ratio of the elastic scattering cross section (σ_s) and the damage cross section (σ_D):

$$DLR = \sqrt{\frac{\sigma_D}{\sigma_s}} \quad (1.2)$$

In the case of chromatin without staining, the image contrast is due to slight shifts in phase (weak phase object approximation), and a critical factor in determining the spatial resolution, there is a trade-off between the electron dose and the signal-to-noise ratio. Consequently, conditions to

maximize the ratio of detectable elastic scattering to damaging inelastic events has to be optimized with great care^{117,118}.

Besides optimizing the imaging condition, another approach is to image the sample at cryogenic temperature to inhibit diffusion. While the physics of electron scattering does not change, the diffusion rate is lowered significantly, and the free-radicals generated during bond-breakage cannot roam free as in the case of room temperature imaging. Cryo-imaging is essential to image frozen-hydrated sample; it is also beneficiary in terms of reducing beam damage for resin-section samples and should be applied whenever possible.

In a completely different background, compressive sensing (CS) was initially formulated to reduce the number of bits required to transmit data from sensors to the processing center without losing information¹¹⁹. As shown in 1.3, the data to be measured (x) is coded by a sensing matrix (H), and the data acquired (y) is a superposition of the coded information and some noise.

$$y = Hx + \varepsilon \quad (1.3)$$

In TEM, x denotes the electron amplitude on a camera pixel, and H is its conversion into a digital value y . For STEM, x denotes the number of electrons scattered or transmitted, H represents the conversion to the photomultiplier tube as the probe raster scans the sample, and y is the digital value recorded. For both scenarios, H is an identify matrix, and x and y are substantially equivalent, there is no compression in the process. It is possible to reduce the dimension of H if x is appropriately sparse. As in the following example:

$$Hx = y, \quad (1.4)$$

$$\begin{bmatrix} 1 & 3 & 1 & 2 \\ 2 & 3 & 4 & 4 \\ 6 & 7 & 0 & 12 \end{bmatrix} \begin{bmatrix} 1 \\ 3 \end{bmatrix} = \begin{bmatrix} 7 \\ 14 \\ 42 \end{bmatrix}, \quad (1.5)$$

which is equivalent to:

$$\begin{bmatrix} 1 & 2 \\ 2 & 4 \\ 6 & 12 \end{bmatrix} \begin{bmatrix} 1 \\ 3 \end{bmatrix} = \begin{bmatrix} 7 \\ 14 \\ 42 \end{bmatrix} \quad (1.6)$$

In this sense, both the sensing matrix H and output y has reduced dimensions, or “compressed”. However, it is impossible to recover x from y and H , as all three vectors in **1.7** satisfy the equation. The prior knowledge that x is sparse does not provide information on where x is sparse.

$$\begin{bmatrix} 1 \\ 0 \\ 0 \\ 3 \end{bmatrix}, \begin{bmatrix} 7 \\ 0 \\ 0 \\ 0 \end{bmatrix}, \begin{bmatrix} 0 \\ 0 \\ 0 \\ \frac{7}{2} \end{bmatrix} \quad (1.7)$$

It is crucial to design a full rank sensing matrix H ; performing CS effectively comes down to intelligent engineering of the sensing matrix H ¹²⁰. Practically, many algorithms have been proposed to compressively acquire signal to reduce acquisition time in optical microscopy, MRI imaging, and X-ray tomography¹²¹⁻¹²³. In the past five years, a wide range of work has been reported for the application of CS in electron microscopy and reduce the electron dose and acquisition time¹²⁴⁻¹²⁶. In tomography, the proposed method will inevitably harm the reconstruction resolution as the sensing matrix is spardse in the angular domain, which is

intrinsically nonsparse¹²⁷. Future work to implement the idea of CS or sparse imaging correctly can potentially reduce the beam damage and push for higher resolution.

1.4 Scope of the Dissertation

This thesis will describe several methods utilizing electron microscopy or imaging processing to design new methods of interrogating chromatin organization with a focus on quantitative characterization. In principle, many of the techniques delineated henceforth are equally applicable to many other biological systems if the primary goal of imaging involves thick specimen, low contrast, and beam sensitive sample, quantification of mass-density distribution, and 3D tomography reconstruction. Chapter 2 will first review the challenges in performing electron tomography on an unstained entire mammalian cell, will then introduce the optimization of imaging setup based on Rayleigh criteria and depth of field in STEM. The resolution limit under the optimized imaging condition will be discussed, and a real experiment demonstration on an entire human cheek cell will be presented. As in Chapter, unlabeled cheek cell provides only the mass-density distribution of everything inside the nuclear plasma. Chapter 3 will then highlight the combination of STEM tomography with an advanced labeling method in which the DNA will be specifically targeted. Adding the molecular specificity into the quantitative HAADF imaging contrast, we investigated the chromatin structure in real mass density at a resolution sufficient to resolve individual nucleosomes and linker DNAs. Utilizing the hybrid method, ChromSTEM, we observed that the chromatin self-organized into spatially separable packing domains with a fractal intern structure. The size of the packing domains ranges from 100kb to 400kb, comparable to the size of topologically associated domains (TADs). With real 3D reconstruction, we can quantify

the chromatin organization in its full glory, but the yield of conventional electron tomography is not high enough to address the significant inter-cellular chromatin heterogeneity across cell populations. On the other hand, tomography generally involves prolonged radiation and can potentially introduce beam damage. In order to reduce the experiment cycle and the beam damage, we will then shift gears slightly in Chapter 4 and discuss a novel algorithm to obtain the statistical mass-density distribution of chromatin in an unstained mammalian cell from a single STEM projection image and correlative AFM height map as an alternative to the method introduced in Chapter 2. To fast track the deterministic 3D imaging, we will introduce a practical sparse-imaging sampling scheme for STEM tomography in Chapter 5. The advantage in reducing beam damage and acquisition time will be discussed, and reconstruction quality through conventional tilt series and CORT will be compared. Finally, Chapter 6 will summarize the thesis and highlight some critical potential items for future work for multi-scale, multi-omics, correlative chromatin characterization.

CHAPTER 2 LABEL-FREE 3D IMAGING OF MAMMALIAN CELLS USING SCANNING TRANSMISSION ELECTRON TOMOGRAPHY

2.1 Imaging Thick Biological Sample

While many biological structures are linear or two dimensional, such as microtubules and DNA fibers, the spatial organization of these structures adopts complex three-dimensional (3D) architecture, and an intact but dynamic 3D structure is essential to maintaining cellular functions. To investigate the role of physical construction in controlling biochemical processes, it is essential to resolve the 3D organization in its full glory. For example, interrogating the role of ER in matter transportation to and from the nucleus is only feasible by reconstructing its three-dimensional membrane network¹²⁸⁻¹³⁰. The length scale of cellular biological complex ranges from a few nanometers (nucleotide) to several microns (organelles), which imposes an additional requirement for complete characterization: resolution. To meet both needs, electron tomography becomes the technique of choice.

Electron tomography has been performed routinely for thin biological samples since its invention. However, the limited mean-free path of electrons constrained the thickness of samples can be viewed with an electron microscope to be no more than several micrometers⁹³. In tomography, as the sample positions at high angles, the penetration depth scales proportional to the cosine of the tilt angles, and approach infinity when it is parallel to the electron beam. Practically, a cryo- or resin-section with 100 to 200 nm in thickness of a larger biological sample is prepared by ultramicrotomy for electron tomography, and the tilt range is from -70° to 70° . Due to the phenomenon intra-cellular heterogeneity, a cross-section that accounts for less than 1/10 of

the whole sample is rarely representative. To observe the structural features of the biological samples along the z-direction, serial sectioning followed by electron tomography is usually required. However, this approach is extremely time-consuming, as hundreds of sections are needed for a typical mammalian cell with 10 μm in thickness. More importantly, serial sectioning is technically challenging as knife marks, ridges, and crevasses are almost inevitable, and when it occurs, artifacts will be introduced into the images⁹⁹. The thinner the sections, the more surfaces we will have, the more artifacts will be introduced in the reconstruction of the whole cell. In this sense, imaging thicker samples directly will not only reduce the time needed but also avoid sectioning-related artifacts significantly.

2.2 Challenges in Imaging Thick Biological Samples

Beam Damage

The first challenge in conducting electron tomography in thick biological samples is the beam damage over prolonged electron exposure. Many review articles are devoted to the beam damage in electron tomography of biological samples^{70,131-133}. Electron microscope radiation has the primary effect of producing intense ionization in organic materials, which results in the formation of free radicals and ions, which causes bond scission and molecular fragment formation. This damage is more pronounced in thick samples, as the free radicals and ions are “trapped” inside the sample, causing more damage than to thin samples.

The influence of beam damage has two different influences on tomography reconstruction. First of all, the bond breaking will result in sample shrinkage. The decrease in thickness in real space causes the increase of spacing in reciprocal space, which is the same as reducing the number

of pixels sampled in the reciprocal space. The effects of missing information will be discussed in detail in the “missing wedge” session. As the radiation damage continues to accumulate, light element atoms like H and O will be broke and results in loss of mass. The physical change of sample morphology will introduce obscure artifacts that cannot be removed in post-processing.

Resolution Deterioration

Due to scattering, the electron changes trajectory and energy after interacting with the sample (both elastic and inelastic scattering) and continuously coarsen the resolution as the sample thickness increases. Scanning transmission electron microscopy (STEM) showed improved resolution for thick samples as a result of reduced chromatic aberration for lacking objective lens and therefore is the technique of choice. In general, the focal plane for a covered STEM electron probe should be placed in the middle of the sample with thickness t , and the corresponding resolution is determined by the surface probe size (PS) following:

$$PS = d + t \tan \alpha, \quad (2.1)$$

where d is the size of the probe at the center of the sample (Figure 2.1). According to the Rayleigh criterion, the depth of field (DOF) is calculated from the wavelength of the incident beam λ and convergence angle α :

$$DOF = 0.61\lambda / \sin\alpha. \quad (2.2)$$

The Raleigh criterion points out the intrinsic trade-off between the lateral resolution and depth of field in STEM imaging. On the one hand, the larger the convergence angle, the smaller the surface probe size, and the higher the lateral resolution. On the other hand, the larger the convergence angle the probe has, the smaller the depth of field is, and the fewer parts of the sample can be imaged on focus at large tilt angles.

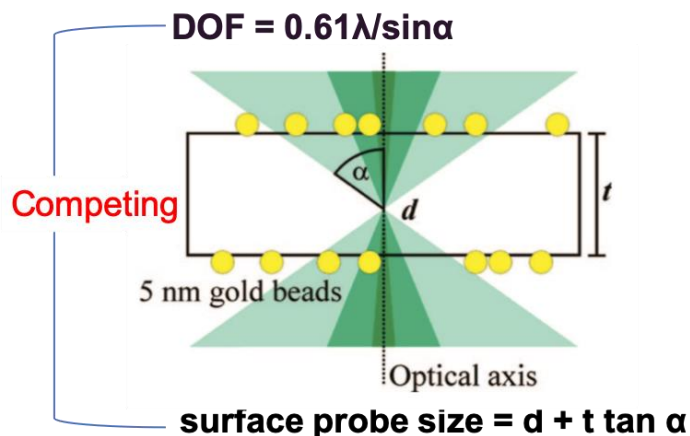


Figure 2.1 Intrinsic trade-off between lateral resolution and depth of field (DOF) for STEM imaging for thick samples. The DOF is inversely related to the convergence angle while the lateral resolution is positively correlated with the convergence angle. At high tilt, a small DOF will limit the region in the sample in focus.

2.3 Solutions to Image Thick Biological Samples

Imaging at Cryogenic Temperature to Reduce the Effects of Beam Damage

Noticeably, knock-on damage, and radiolysis, which are the primary beam damage mechanisms for biological samples, happen at all temperatures. However, by decelerating the speed of diffusion, it is possible to reduce the damage caused by radiation¹³⁴. It is reported that by lowering the temperature to liquid nitrogen (98K), the structural alterations can be considerably reduced. Modern-day electron tomography for biology study is routinely conducted at cryogenic temperature to reduce the beam damage to the sample.

Optimizing imaging condition sample orientation

The ideal convergence angle should provide sufficient lateral resolution on each surface as well as the sufficient depth of field so that the entire sample can be in focus at a large tilt angle. Depending on the sample thickness and imaging field of view, it is essential to optimize the electron probe convergence angle before tomography data acquisition. In addition, the sample positioning also plays an important role. In theory, the focal plane should be placed in the middle of the sample such that the lateral resolution at both of the sample surface is the same. In reality, the focal plane is usually placed on the top surface. To compensate for the uneven lateral resolution through z-direction, during the second tilt series, not only the sample should be rotated 90° on the x-y plane, but also flipped upside-down¹⁰⁰.

2.4 Materials and Methods

2.4.1 Entire Cheek Cell Preparation for STEM tomography

Cells from buccal mucosa (cheek cells) were collected using a Cytobrush (CooperSurgical Inc.), suspended in 1 mL 1x PBS and spun for 5 min at 1500 rpm (Fisher Scientific accuSpin; Micro17). The supernatant was aspirated, and the pellet was resuspended in PBS. Droplets of 30 μ L of the cell suspension were deposited on TEM grids in a moisture chamber for cell attachment. The chamber was kept in a cell incubator for 30 min; then the sample was fixed with 2.5% glutaraldehyde and 2% formaldehyde in PBS for 20 minutes at room temperature. After fixation, the grids were rinsed in DI water. The sample was then mixed with 5% colloidal gold nanoparticles (mean diameter of 200 nm, Sigma-Aldrich) before plunge-frozen with a Vitrobot (Vitrobot Mark III FEI). The colloidal gold nanoparticles were later used as the resolution reference in optimizing microscope setup and fiducial markers in tilt series alignment. The frozen sample was freeze-dried

in a turbo-freeze drier (K775X, Emitech) to remove water from the sample without alternating the structure. The tilt series was imaged at low temperature in a cryo single tilt holder (Gatan Inc.)

2.4.2 Optimization of Electron Microscope Setup

A 200kV STEM (HD2300, HITACHI) was employed for all the image collection. Each image has a pixel size of 73 nm and a pixel dwell time of 10 μ s. We tested the effects of convergence angle by varying the electron probe size (10mrad and parallel) for cheek cells tilted at 0° and 60°. We discovered that at the current magnification, the parallel probe was able to resolve the gold nanoparticles over the whole cell at both orientations, while the probe with large convergence angle was unable to capture the edge of the cell at high tilt angle Figure 2.2.

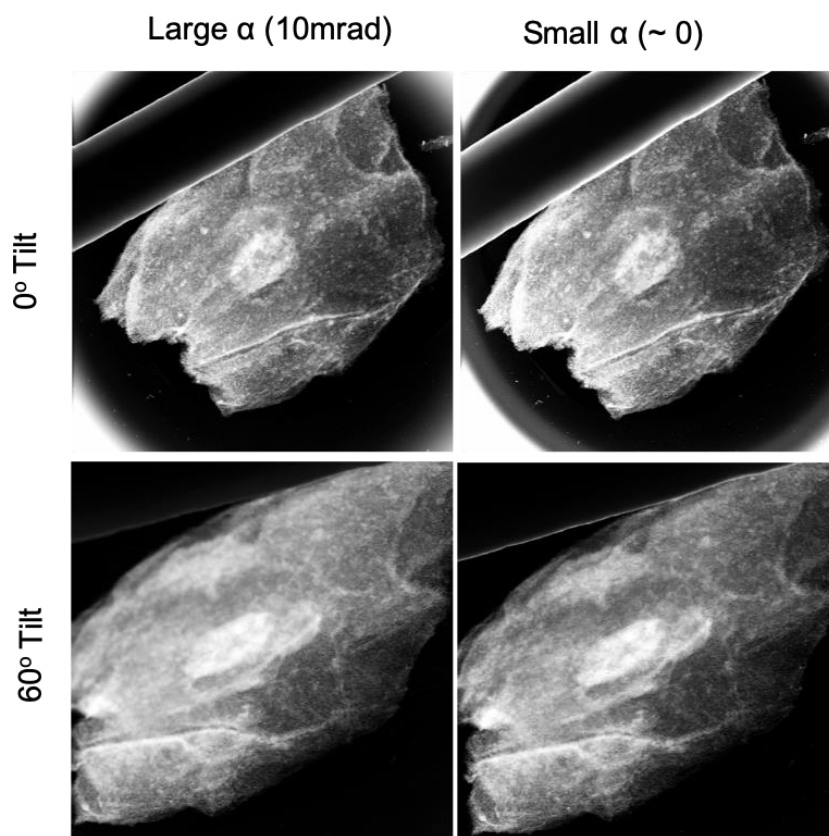


Figure 2.2 Effects of convergence angle in image quality at different tilt angles. A convergence angle of 10 mrad and parallel probe ($\sim 0^\circ$) was employed for sample oriented at 0° tilt and 60° tilt. For the low tilt angle, under current magnification, the resolution is identical for both probes. For the high tilt angle, the 10 mrad convergence angle provided a small DOF, and the edge of the cell was not in focus. In contrary, the parallel probe was able to capture the entire cell in focus.

We further analyzed the resolution of the parallel probe through the full-width-half-maximum (FWHM) of the first derivative of the line profile of the image intensity across a 30 nm

gold nanoparticle at high magnification (Figure 2.3). We found that the resolution was 7.4 nm at current scanning condition, indicating that at lower magnification with a pixel size of 73 nm, the resolution is solely limited by the pixel size, not the probe size. Consequently, the parallel beam is ideal for tomography data collection for the whole cheek cell.

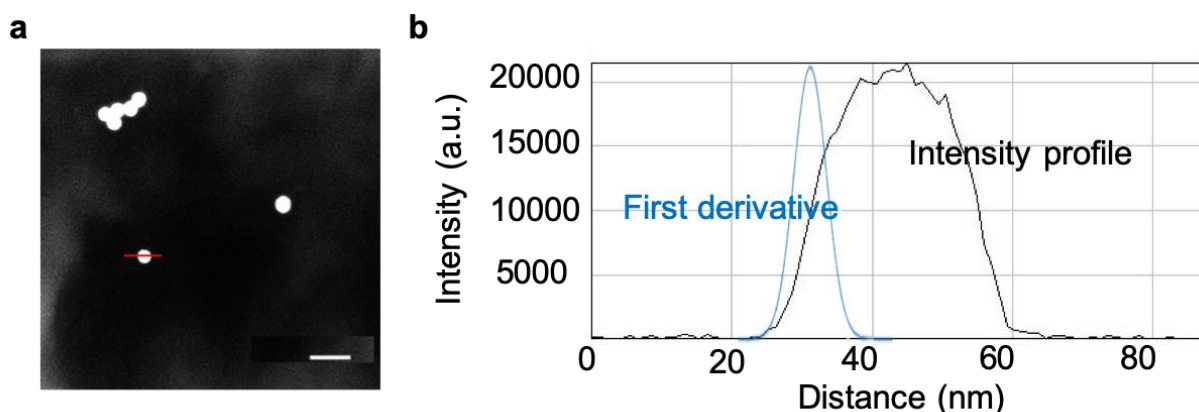


Figure 2.3 Estimation of the resolution of a parallel probe at higher magnification. We obtained the image resolution by the full-width-half-maximum (FWHM) of the first derivative (b, blue curve) of the intensity line profile (b, black curve) across a gold nanoparticle (a, red line). Scale bar: 100 nm for (a).

2.4.3 Dual-tilt Tomography Reconstruction

Dual-tilt tomography tilt series collection was conducted at low temperature (-166°C for the first axis and -100°C for the second axis) with parallel electron probe to reduce artifacts introduced by “missing wedge”, beam damage, and out of focus at high tilt angles. After the first tilt series

acquisition, the sample was manually flipped upside-down and rotated around 90° under liquid nitrogen (Figure 2.4). For both tilt series, tilting angle ranged from -60° to 60° with 2° increment.

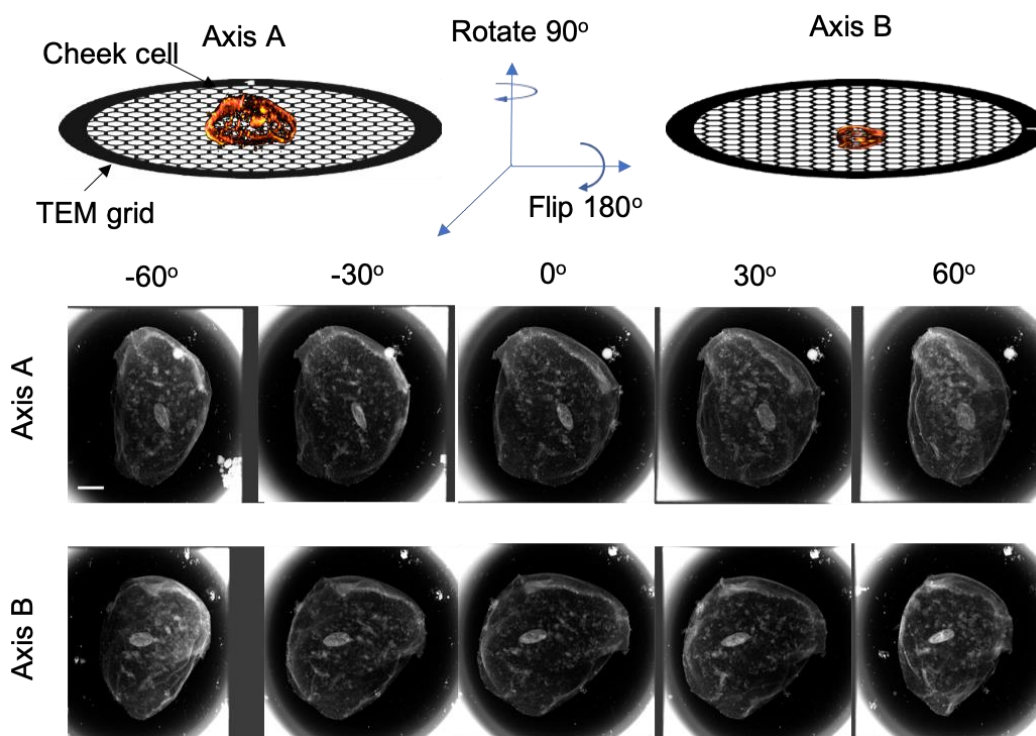


Figure 2.4 STEM tomography tilt series of a whole cheek cell. Top panel: The cheek cell was deposited on the top surface of the TEM grid for the first tilt series (Axis A). Later, the sample was manually flipped upside-down and rotated 90° laterally for the second tilt series (Axis B). Middle and bottom panel: examples of HAADF images of the sample at different tilt angles with respect to Axis A and B. Scale bar: $10\ \mu\text{m}$.

The fiducial marker assisted alignment was performed in IMOD for each tilt series independently, penalized maximum likelihood (PML) algorithm was employed to reconstructed

3D structure from each a tilt series in Tomopy, and combination of the tomograms was again conducted in IMOD (Figure 2.5 a)^{63,135}. 3D surface rendering was performed to visualize the distribution of organelles in space using Volume Viewer in ImageJ (Figure 2.5 b)¹³⁶. We identified multiple features from the virtual 2D slices from tomography reconstruction, including vesicle, liposomes, and nucleus ((Figure 2.5 c-e). Compare to the ultra-thin resin-sections of cheek cells with heavy metal staining (Figure 2.5 f-h), the image contrast and morphological features are similar. However, the final tomography contains 163 virtual 2D slices, and each slice is 73 nm in thickness. We calculated the thickness of the whole cell to be around 12 μm . To obtain the same information by serial sectioning at a similar axial resolution, one needs 163 continuous sections, which is extremely challenging and will introduce artifacts associated with sectioning to the data.

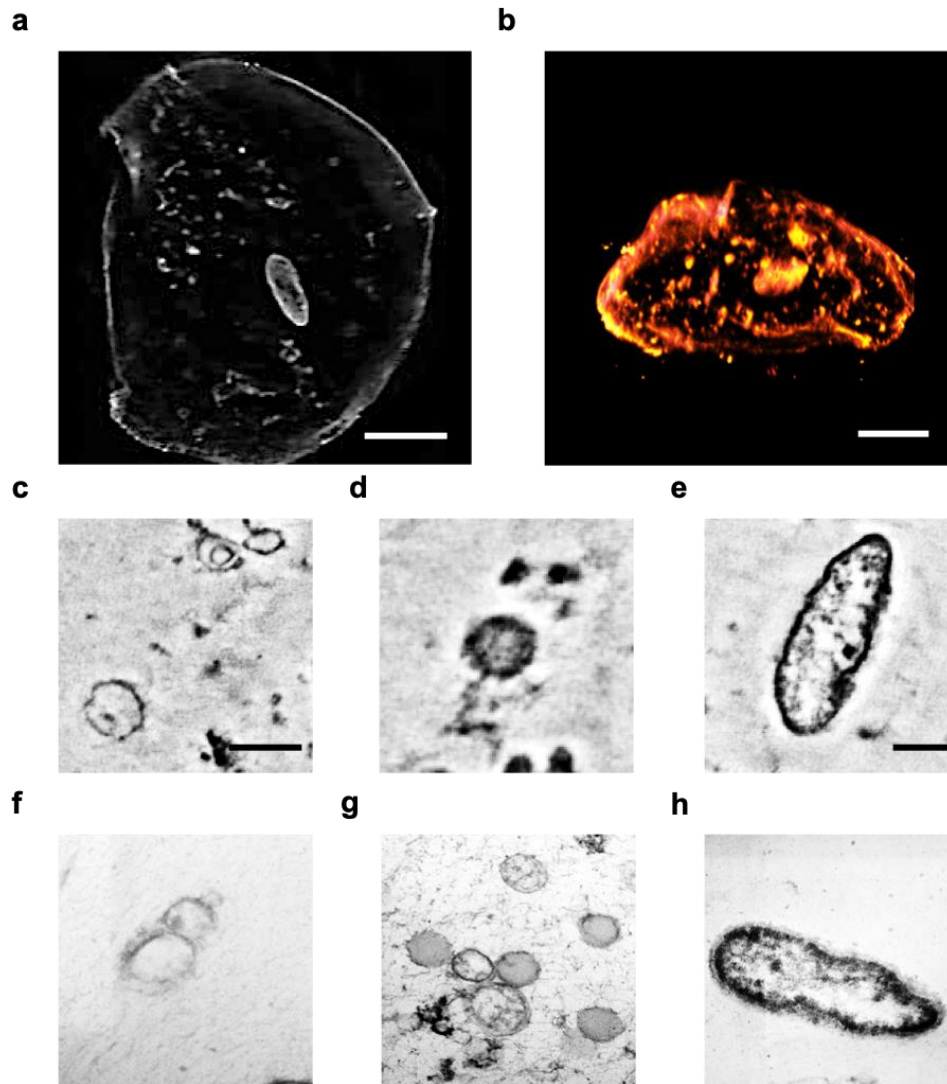


Figure 2.5 Tomography reconstruction of an entire human cheek cell. (a) One virtual 2D slice with a nominal thickness of 73 nm in the middle of the cell. Scale bar: 10 μm . (b) Volume rendering of the tomography, x-z (side) view. Scale bar: 5 μm . (c-d) Organelles resolved in the virtual 2D slices (contrast inverted). (c) Vesicles. (d) Liposomes. (e) Nucleus.

(f-h) Bright field STEM imaging of a 70 nm thick resin-section of cheek cell. (f) Vesicles. (g) Liposomes. (h) Nucleus. Scale bar: 1 μm for (c-d), (f-g); 5 μm for (e) and (h).

2.5 Discussions and Conclusions

For the second tilt series, we observed ice crystals forming on the sample surface, which were deposited during sample repositioning (Figure 2.6 a). To remove the ice crystals without damaging the sample, we slowly raised the temperature of the holder from -164°C to -100°C . Under the low vacuum environment, similar to freeze-drying, the ice sublimed during the process (Figure 2.6 b). At -100°C , the water molecules were mobile, indicating the diffusion was resumed. The heating might lead to the mobility of the free radicals generated by radiolysis and cause sample alterations or beam damage. For better preservation of the sample, before the second tilt series collection, the sample should be cooled down to at least -160°C in the microscope.

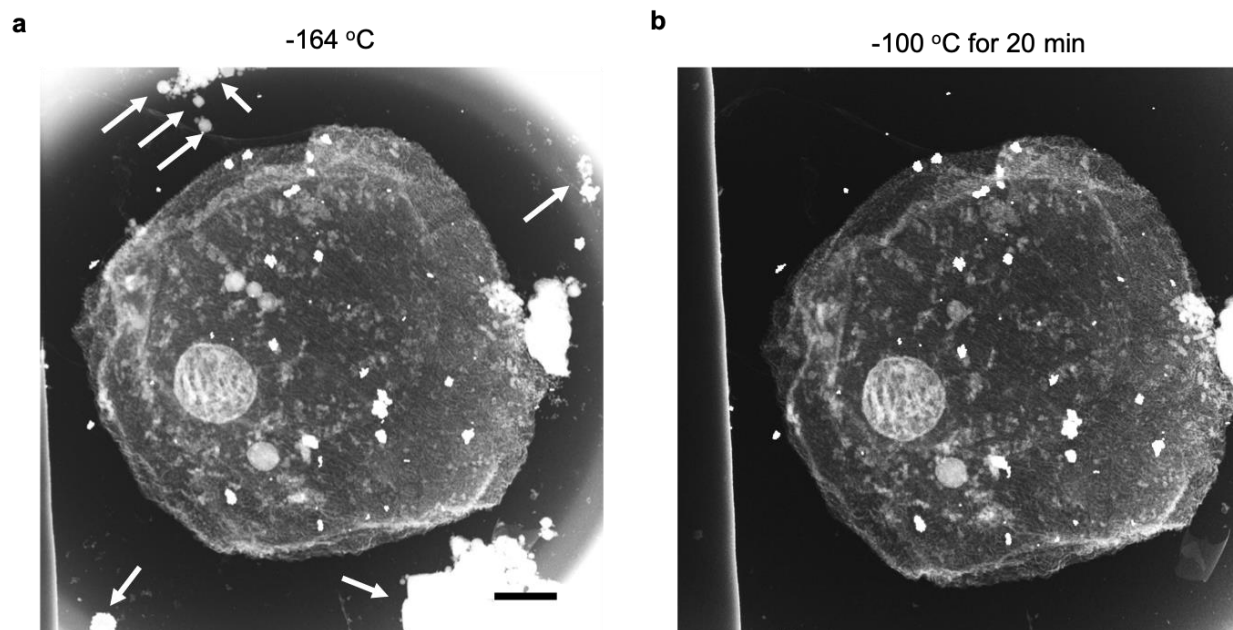


Figure 2.6 Subliming ice crystals at ultra-high vacuum in the electron microscope chamber. (a) Ice crystals (arrows) formed during sample repositioning and kept stable at -164°C inside the electron microscope chamber. Scale bar: $5\ \mu\text{m}$. (b) Increased the temperature to -100°C for 20 min, the ice sublimated without damaging the sample.

To estimate the possible sample structural alterations induced by prolonged electron radiation, we recorded HAADF images before and after tomography tilt series acquisition at 0° tilt. The image recorded (Figure 2.7 b) after the second tilt series acquisition was rotated 90° to match the lateral orientation with the image recorded before the first tilt series (Figure 2.7 a). We performed a rigid transformation (translation and rotation) and overlaid the two images (Figure 2.7 c). Qualitatively, after collecting 122 images of the same sample, under current imaging condition and cryogenic temperature, the morphology of the sample stays mostly intact. As

previously mentioned, the stage temperature was raised in between two tilt series to eliminate icicle condensation. The icicles created during plunge-freezing (bottom right corner in Figure 2.7 a) also sublimed during this process. Quantitatively, we measured the distance between 16 pairs of gold fiducial markers on the surface of the cheek cell before and after tilt series collection (Figure 2.7 d red points). We fitted the distribution of pairwise distances to a linear equation in the form of $y = x$ (Figure 2.7 d blue line). As the calculated r^2 in the linear regression is 0.998, we concluded that the level of sample shrinkage due to beam damage was minimal.

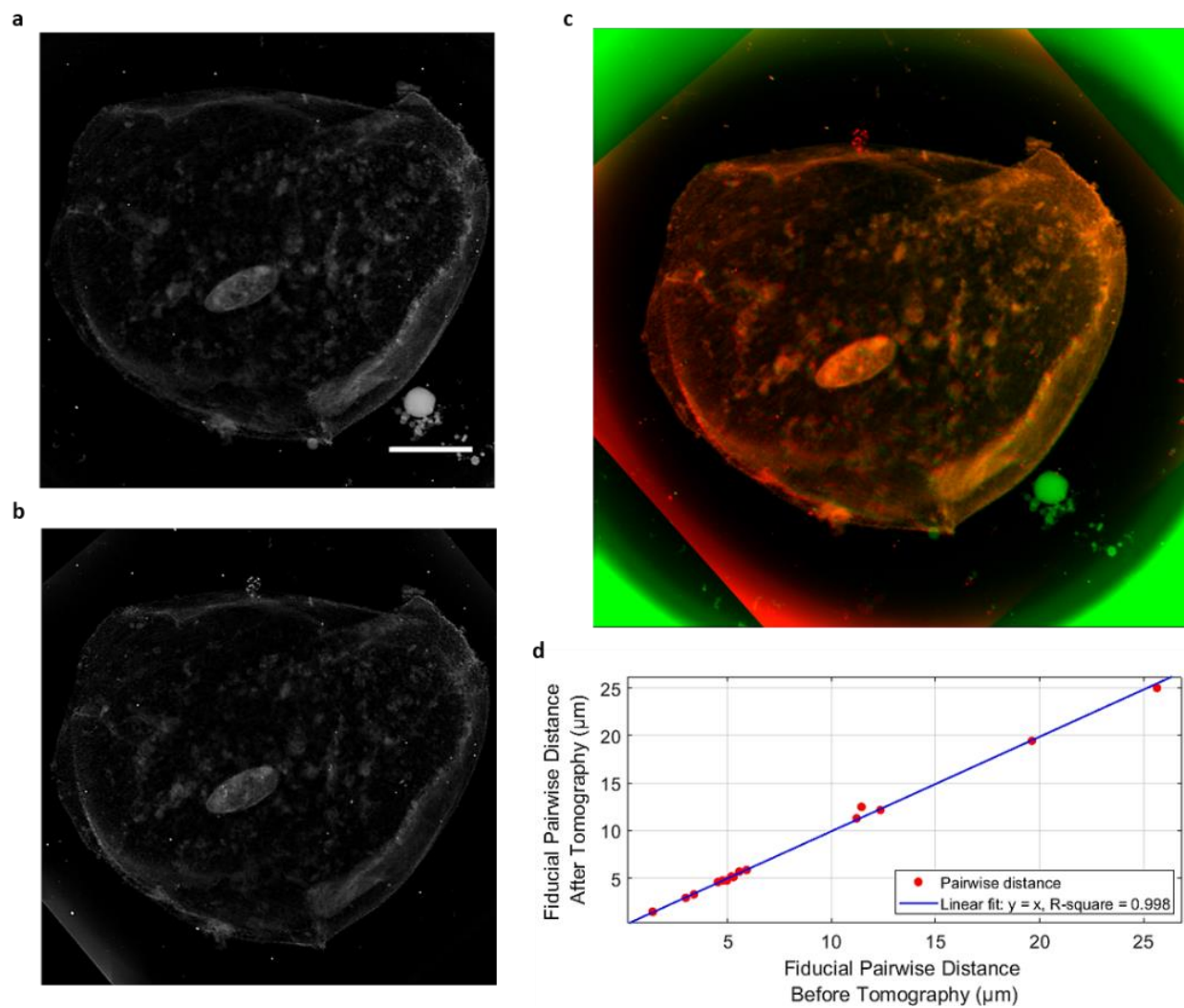


Figure 2.7 Comparing sample morphology before and after dual-tilt series collection. (a) Before the first tilt series collection. (b) After the second tilt series collection. In both images, the sample was oriented at 0° tilt. The second image was rotated 90° laterally to match the orientation of the first image for direct visual comparison. Scale bar: $10\ \mu\text{m}$. (c) Overlay of the two images. Green: (a), red: (b). (d) Pairwise distances between 16 pairs of fiducial

markers on the cheek cell before and after tilt series acquisition. The data points were fitted to a linear function: $y = x$.

The cheek cell has a moderate solid content (~30% in the cytoplasm and ~50% in the nucleus). After removing the water by freeze-drying, the dehydrated sample is extremely porous. Even though the thickness of the sample is around 12 μm , most of the volume is empty. The actual thickness of the mass condensed is around 1 μm in thickness, which makes the imaging possible without losing the spatial resolution. In this specific experiment, the image resolution is 73 nm laterally, and the axial resolution is worse than 73 nm due to stretching of the tomography caused by “missing cone”. However, the resolution in all dimensions can be improved if the tilt series collection is conducted at higher magnification. In addition, to reduce the stretching artifacts, multiple axis tilting can be performed. The processing is similar to dual-axis tomography, with more than two sets of independent tomograms to be combined.

Notice that the sample was prepared by the freeze-drying method, and the freeze-dried sample can experience structural alterations such as shrinkage and collapse. However, the sample ultrastructure is preserved better compared to the alternative method such as chemical fixation with serial ethanol dehydration followed by either resin embedding or critical point drying (CPD)¹³⁷. Furthermore, the tomography of the whole cell does not require serial sectioning by ultramicrotomy to provide structural information in full 3D. We believe this method has potentials to open doors to investigate intra-cellular heterogeneity with higher throughput and statistical

accuracy, and should be employed in fields including structural biology, epi-genomics, and tissue-engineering, among others.

CHAPTER 3 MULTI-SCALE QUANTIFICATION OF 3D GENOME ORGANIZATION USING SCANNING TRANSMISSION ELECTRON MICROSCOPY: CHROMSTEM

Chromatin organization over a wide range of length scales plays a critical role in the regulation of gene expression and deciphering these processes requires high-resolution, three-dimensional, quantitative imaging of chromatin structure *in vitro*. Herein we introduce ChromSTEM, a method which utilizes high angle annular dark field imaging and tomography in scanning transmission electron microscopy in combination with DNA-specific staining for electron microscopy. We utilized ChromSTEM to quantify chromatin structure in cultured cells and tissue biopsies through local DNA distribution and the scaling behavior of chromatin polymer. We observed that chromatin is densely packed with the average volume concentration over 30% with heterochromatin having a two-fold higher density compared to euchromatin. Chromatin was arranged into spatially well-defined nanoscale packing domains with fractal internal structure and genomic size between 100 and 400 kb, comparable to that of topologically associated domains. The packing domains varied in DNA concentration and fractal dimension and had one of the distinct states of chromatin packing with a differential ratio of DNA content to the chromatin volume concentration. Finally, we observed a significant intercellular heterogeneity of chromatin organization even within a genetically uniform cell population, which demonstrates the imperative for high-throughput characterization of chromatin structure at a single cell level.

3.1 Previous Work on 3D Chromatin Imaging

Regulation of gene transcription is essential in sustaining normal cell function, controlling cell differentiation and determining cell fate, and transcriptional alterations have been implicated in a variety of diseases including cancer and cardiovascular, developmental, neurological, and autoimmune disorders¹³⁸⁻¹⁴⁰. While early studies, which focused on the molecular mechanisms of transcriptional regulation based on a linear model of genome organization, provided significant knowledge of the genome regulation, they also demonstrated the substantial limitations of this approximation¹⁴¹⁻¹⁴⁷. Recent studies have unambiguously shown that genes can interact with multiple distal elements within distances up to several Mb away, suggesting machinery of transcriptional regulation based on the three-dimensional (3D) chromatin structure¹⁴⁸⁻¹⁵¹. While the genetic information is encoded in the linear sequence, the appropriate gene transcription requires complex 3D genome organization.

A number of methods have been developed to analyze 3D chromatin structure, including chromatin conformation capture (e.g., Hi-C), neutron scattering, soft x-ray tomography (SXT), and super-resolution microscopy¹⁵². These techniques have provided critical insights into the principles of 3D chromatin structure. However, they have fundamental limitations such as the inability to quantify the spatial distribution of chromatin (C-based, neutron scattering) or limited resolution (30-50 nm for SXT, super-resolution microscopy)¹⁵³⁻¹⁵⁷. To precisely image chromatin down to the level of a single nucleosome (11nm) and DNA strands (2nm) and map the 3D chromatin architecture within the nucleus, electron microscopy (EM) remains the technique of choice.

Recently, Ou et al. reported a new transformative approach, which utilizes “click-EM” staining that specifically labels DNA and multi-axis transmission electron microscopy (TEM) tomography, for chromatin imaging with a nominal resolution of 1.6 nm in 3D (ChromEMT). Using ChromEMT Ou et al. demonstrated that chromatin is a disordered 5 to 24 nm diameter polymer chain, rather than the classically considered hierarchically folded assembly^{32,156}. As TEM imaging contrast is non-linear (confounded by phase, diffraction, and mass-thickness contrast), the application of TEM-based imaging to quantify chromatin packing in terms of physical mass-density distribution is challenging. Furthermore, it is difficult to perform ChromEMT for the whole cell, as it would require dozens of serial-sections to cover a mammalian nucleus (~6 μm thick). The challenge becomes even more daunting when a comparative analysis of several cells or cell types exposed to differential conditions is required. The complexity is further exacerbated by the phenomenon of genomic and transcriptional intercellular heterogeneity, which most cell populations exhibit, and which would necessitate the analysis of an ensemble of cells.

3.2 ChromSTEM Platform Formulation

3D chromatin organization governs gene transcription by controlling genome connectivity, DNA accessibility, and transcriptional heterogeneity. Emerging evidence shows that the proper positioning of the chromatin within the nucleus also plays an indispensable role in maintaining normal transcriptional function¹⁵⁸. To develop a quantitative and high-throughput method for high-resolution, 3D chromatin imaging, we adapted the ChromEMT framework to incorporate STEM high angle annular dark field (STEM HAADF) imaging. This hybrid method, ChromSTEM, allows quantitative imaging through Z-contrast, which originates from Rutherford scattering by

$I \sim Z^{1.7}$, where I is the image contrast, and Z is the atomic number of the atom on the electron trajectory. In the case of ChromSTEM, the osmium bound to the chromatin dominates the image contrast, and the observed image intensity is proportional to the DNA mass-density. We then demonstrate the utility of ChromSTEM by reconstructing the 3D chromatin structure of adenocarcinoma human alveolar basal epithelial (A549) cells at a nominal voxel resolution of 3 nm. We combined the 3D data with ultra-thin section imaging and developed a statistical method to accurately quantify chromatin packing through DNA density distribution, chromatin volume concentration (CVC), chromatin polymer mass-scaling, and nuclear compartment positioning for the whole nucleus. We quantified the packing properties of the euchromatin and heterochromatin compartments. We also observed that chromatin is organized into spatially separated 100 - 200 nm packing domains, with internal fractal structure and genomic size comparable to topologically associated domains (TADs). Across the genome, packing domains varied significantly in their fractal dimension, DNA content, CVC, and packing density heterogeneity.

3.2.1 Overview of the ChromSTEM Platform

Utilizing the ChromSTEM platform, one can obtain quantitative information on the native 3D chromatin architecture. Figure 3.1 shows the roadmap towards a comprehensive analysis of the chromatin organization.

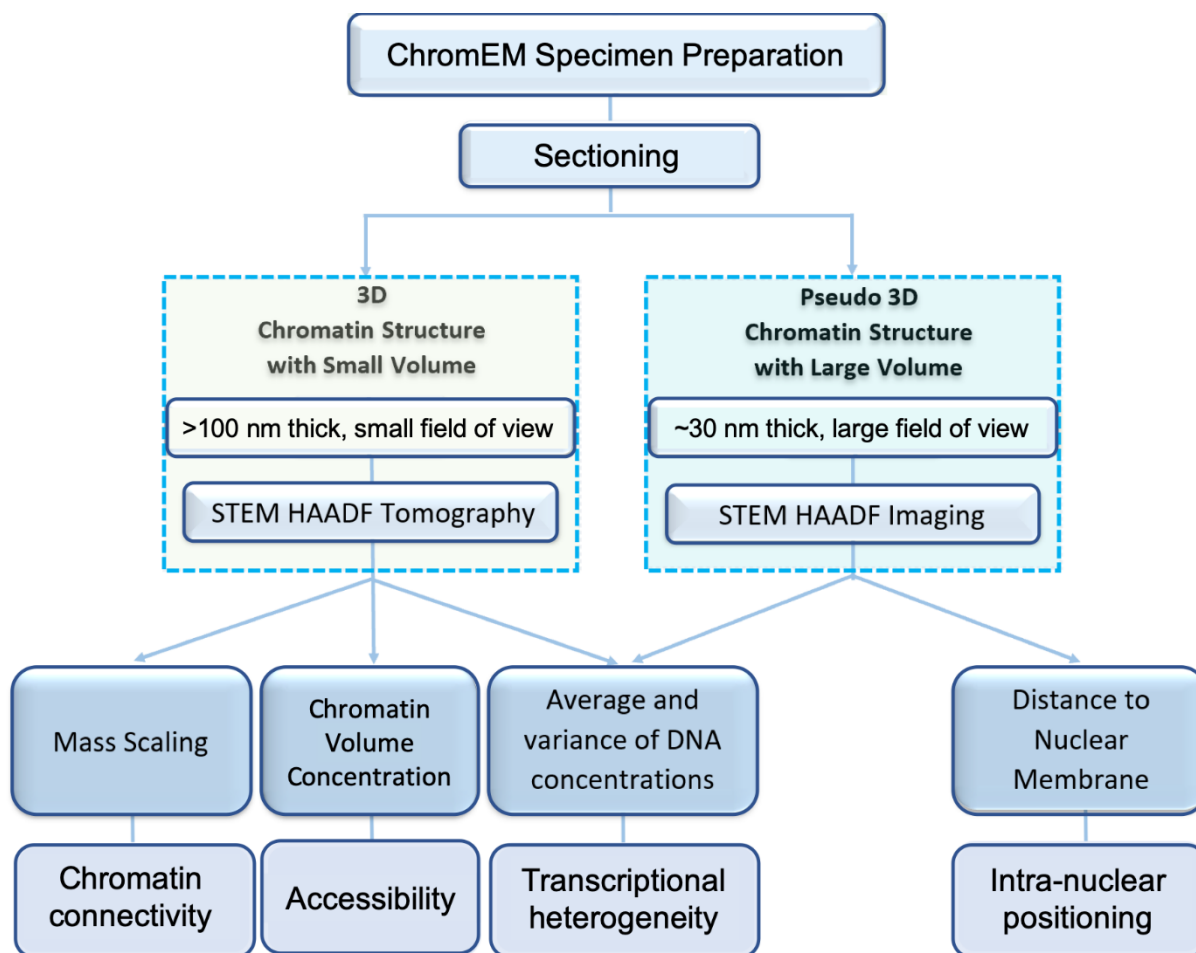


Figure 3.1 Multi-scale quantification of the chromatin organization through ChromSTEM. The ChromSTEM platform includes several experimental techniques to assess chromatin 3D organization by directly measuring the chromatin mass scaling, chromatin volume concentration (CVC), the average and the variance of DNA concentration, the mass scaling exponent (D), and the distance to the nuclear membrane. To estimate chromatin connectivity and accessibility, a 3D tomography reconstruction of semi-thick samples ($\sim >100$ nm thick) can be deployed. The analysis of the spatial distribution of the chromatin throughout the nucleus is achieved by ChromSTEM mapping of a stack of ultrathin sections (~ 30 nm). Both

tomography and thin section projection can be employed to measure chromatin heterogeneity.

3.2.2 ChromSTEM sample preparation

Cell culture and tissue biopsy collection

The A549 adenocarcinomic human lung epithelial cells were grown to reach confluency of 60% in DMEM with 10% FBS and 1x penicillin/streptomycin in 35 mm MatTek dishes (MatTek Corp) at 37°C at 5% CO₂. Animal procedures were performed at NorthShore University Health System, with the approval of the Institutional Animal Care and Use Committee (IACUC). A healthy Fisher 344 rat (150–200 g; Harlan) was euthanized, and the biopsy was harvested from the ovary and immersed in EM fixative immediately at room temperature for 20 min then transferred to a fresh fixative solution and stored at 4°C overnight.

Biological sample culture and harvesting

The A549 cells were prepared using the ChromEM method published previously, and lists of reagents and step-by-step protocols can be found in the supplementary information. The biopsy was embedded in low melting point agarose (Thermo Fisher) and 40 µm thick sections were prepared using a vibratome (VT1200 S Leica) on ice. The sections were deposited onto a glass-bottom petri-dish (MatTek Corp) and treated cultured cells for ChromEM preparation.

ChromEM sample preparation

After fixation, the samples were bathed in blocking buffer for 15 min before stained by DRAQ5TM (Thermo Fisher) for 10 min. The cells were rinsed and kept in blocking buffer before photo-bleaching and submerged in 3-5'-diaminobenzidine (DAB) solution (Sigma Aldrich) during photo-bleaching on the cold stage. After photo-bleaching, the cells were rinsed in 0.1M sodium cacodylate buffer thoroughly. Reduced osmium solution (EMS) was used to enhance the contrast in STEM HAADF mode, and the heavy metal staining lasted 30 min on ice. Serial ethanol dehydration was performed, and during the last 100% ethanol wash, the cells were brought back to room temperature. Durcupan resin (EMS) was used for embedding after infiltration, and the blocks were cured at 60°C for 48 hrs.

For photo-oxidation, an inverted microscope (Eclipse, Nikon Inc.) 100x objective with LED lamp was employed. A cold stage was developed in-house from a wet chamber equipped with humidity and temperature control. For all analysis in the paper, we performed photo-oxidation for 7 min for each region, and fresh DAB solution was used for every time. For the control experiment, we photo oxidized part of the nucleus by illuminating only the corner of the cell. As expected, the nucleus is partially stained, and the boundary between the labeled and unlabeled region adopted a circular shape, the same geometry as the laser spot (Figure 3.2).

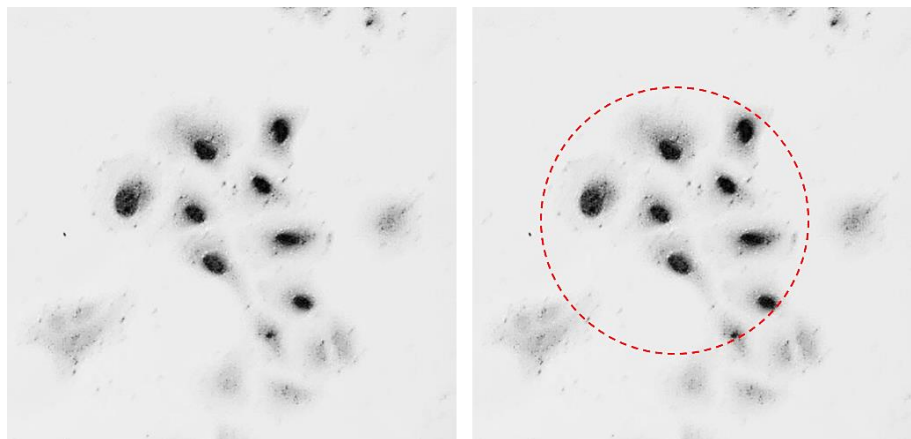


Figure 3.2 Partially photo-oxidized nucleus. The boundary of the labeled regions matches the geometry of the laser spot.

We investigated the influence of photo-oxidation time by illumination two regions in the same dish for 7 min and 25 min, respectively (Figure 3.2). We did not observe a significant difference in the statistical characteristics of CVC between the two.

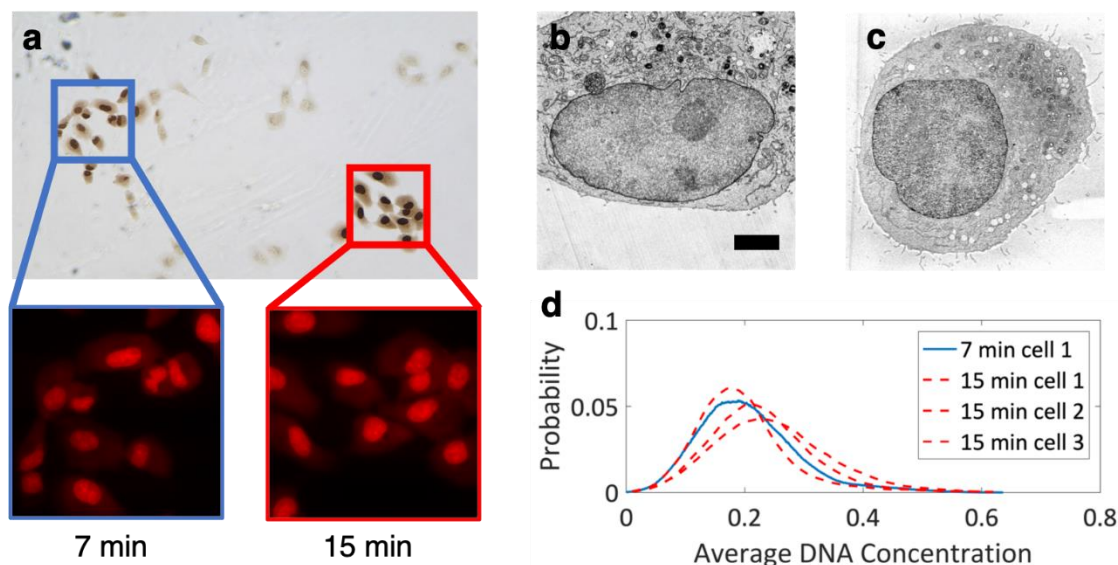


Figure 3.3 Different in staining A549 cell by varying photo-bleaching time. To test the consistency of photo-bleaching, we experimented the process with different illumination time. (a) Photobleaching for 7 min (blue square) and for 15 min (red square). The resulting staining is significantly more substantial in the long photo-bleaching spot. (b) STEM HAADF image (contrast inverted) of the 30 nm section for one cell in the 7 min spot. Scale bar: 2 μm . (c) A TEM image of the 30 nm section for one cell in the 15 min spot. For the TEM images, we first converted the image contrast to mass-thickness using Beer's law, then calculated the average DNA concentration, and normalized the histogram to the same range as the STEM image. (d) Comparison of the histogram of the average DNA concentration for one cell in the 7 min spot (solid blue line) and three cells in the 15 min spot (red dash lines). We observed that the average DNA concentration of the 7 min cell lied in the range of the 15 min cells. Considering cell to cell variations, we concluded that within the time frame,

there is no significant influence of the length of photo-bleaching in the analysis of the chromatin packing.

100 nm thick sections of an A549 cell were made by ultramicrotomy (UC7, Leica) and deposited onto a plasma-treated slot grid with carbon/Formvar film (EMS). 10 nm colloidal gold nanoparticles were deposited on both sides as fiducial markers for ChromSTEM tomography. Ultrathin sections with a nominal thickness of 30 nm for A549 cells and 40 nm for tissue were made and deposited onto a plasma-treated mesh grid with Formvar/carbon film (EMS) for ChromSTEM imaging.

EM data collection and tomography reconstruction

A 200kV STEM (HD2300, HITACHI) with HHADF mode was employed for all image collection. For tomography, the sample was tilted from -60° to 60° with 2° increments on two roughly perpendicular axes. The pixel size was chosen to be 2.9 nm to resolve the fiducial markers. Each tilt series was aligned with fiducial markers in IMOD and reconstructed using Tomopy with a penalized maximum likelihood algorithm for 40 iterations independently. IMOD was used to combine the tomograms to suppress artifacts, and the nominal voxel size is 2.9 nm. The ultrathin sections were imaged at 0° tilt angle with a pixel size of 5.4 nm.

To estimate the possible beam damage during prolonged imaging, we recorded the tomography region before and after dual-tilt series collection and overlaid the two images (Figure c). Qualitatively as indicated by the spatial distribution of the fiducial markers, the sample did not experience significant morphological changes such as stretching and deforming. Quantitatively,

distances between 8 pairs of gold fiducial markers were measured, and the values before and after tomography acquisition were plotted against each other. We fitted the data to a linear function $y = x$, and the r^2 was 0.999, indicating the lateral deformation at current image resolution is neglectable. However, it is still possible that thinning could happen along the z-axis, and the sample should be imaged at cryogenic temperature whenever possible.

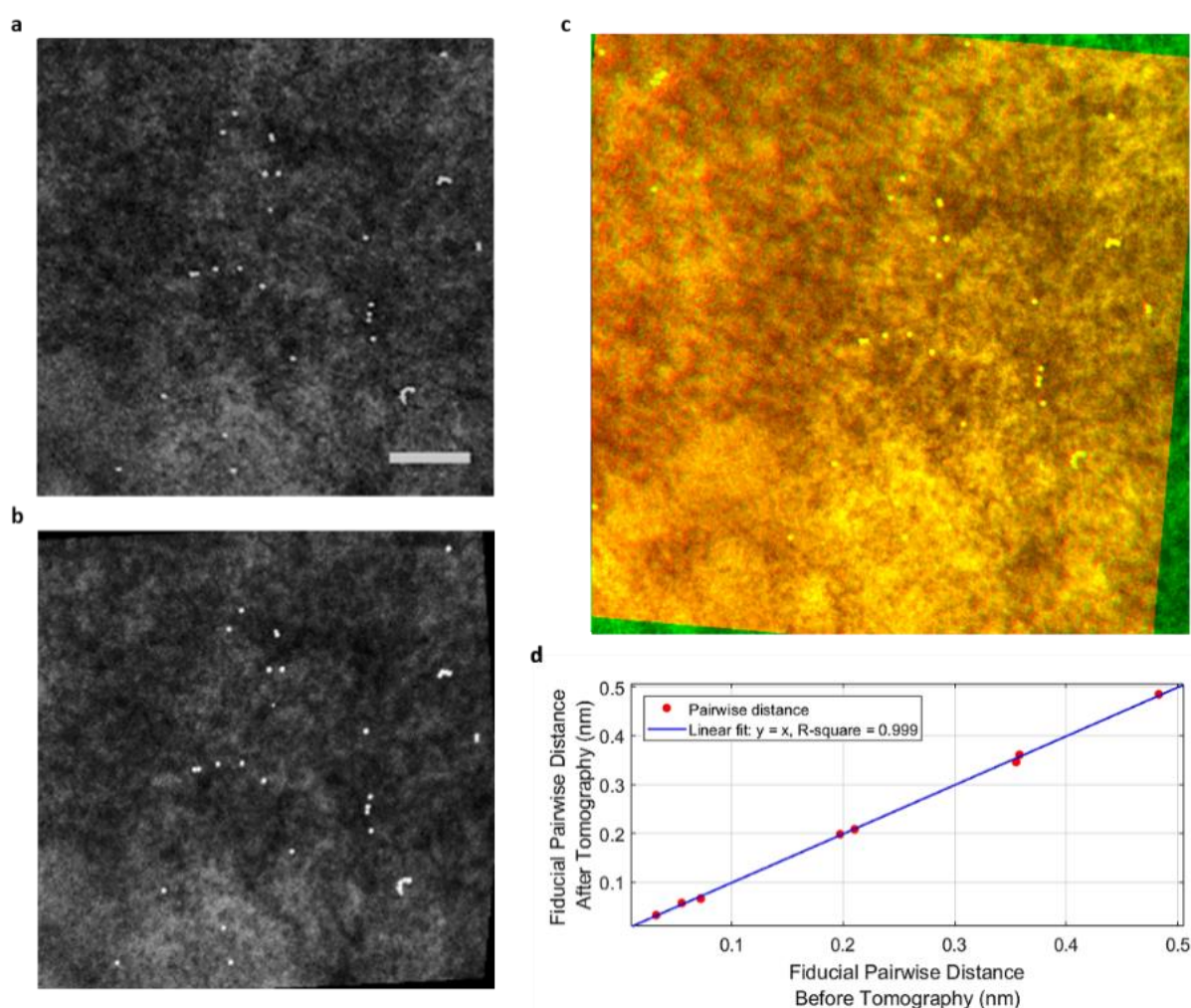


Figure 3.4 Tomography region before and after dual-tilt series collection. (a) The chromatin region before the first tilt-series acquisition. (b) The same region after the second tilt-series

acquisition. Scale bar: 200 nm. (c) Overlay of the two images. Green: (a). Red: (b). (d) Fiducial pairwise distances before and after tomography acquisition.

3.2.3 ChromSTEM Tomography of Cell Nucleus

Following the ChromEM protocol reported previously, we labeled the DNA of A549 cells, and fluorescence images were acquired (Figure 3.4 a, b) during photo-oxidation. After resin embedding, the labeled regions can be identified based on image contrast in bright field optical micrographs: the photo-oxidized cells appeared significantly darker than the non-photobleached cells (Figure 3.4 c). Dual-tilt STEM tomography in HAADF mode was performed for part of the nucleus containing a hetero/euchromatin interface on a 100 nm resin section (Figure 3.4 d). We observed continuous variations of the image contrast inside the nucleus, different from the near binary image contrast from the conventional EM staining method. Each tilt series was aligned with fiducial markers in IMOD and reconstructed by a penalized maximum likelihood (PLM-hybrid) algorithm in Tomopy¹⁵⁹. The two sets of tomograms were combined in IMOD to suppress missing cone artifacts (Figure 3.3)¹³⁵.

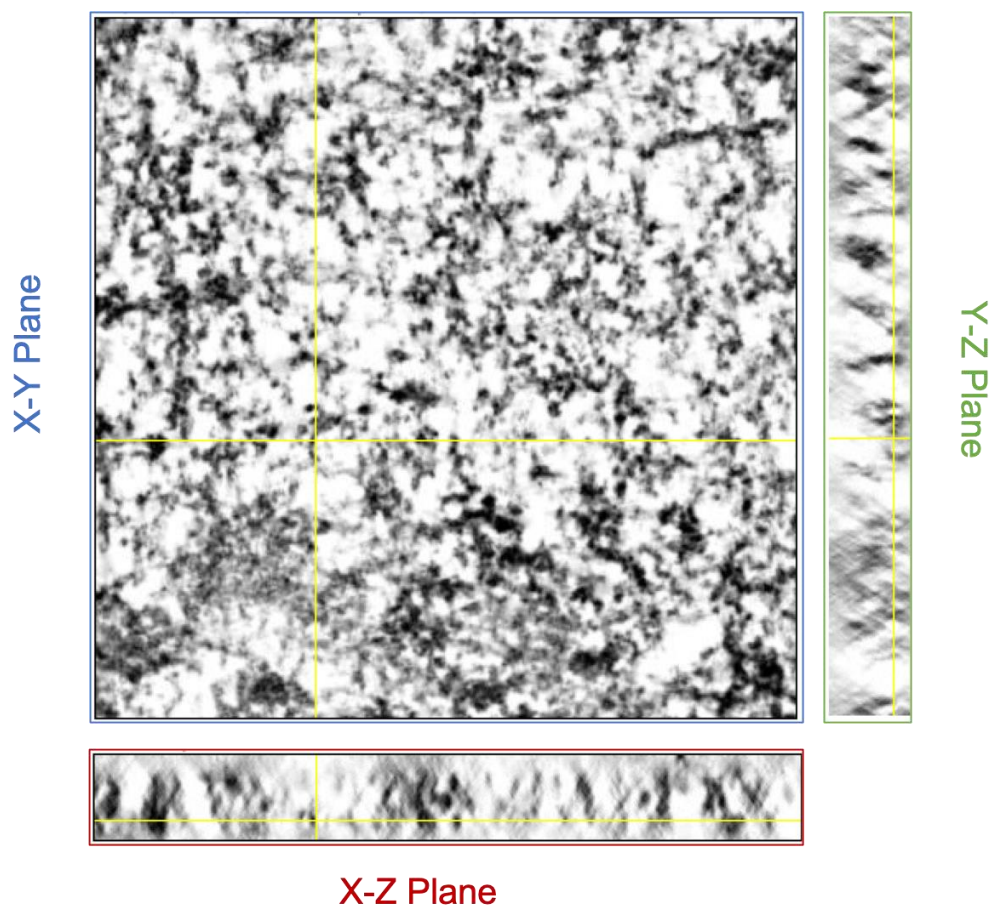


Figure 3.5 Orthogonal views of chromatin after tomography reconstruction of an A549 cell. In the tomography experiment and reconstruction, dual-tilt and penalized maximum likelihood algorithm were employed to suppress the artifacts introduced by the missing cone. In the X-Z and Y-Z plane, the “X” shaped artifacts can still be seen in the tomograms, but the individual nucleosomes can be easily identified, and the stretch in the Z direction is not severe. The quality of this tomography is not as high as the ones used in Ou’s ChromEMT work, as only two axes were used in our work but eight in his work. However, based on the CVC analysis, our tomography exhibits an almost identical histogram like the one shown in

Ou's paper, indicating our tomography has sufficient quality for studying the local chromatin packing for 100 nm super-voxels.

The final tomography (Figure 3.4 h) has a nominal voxel size of 2.9 nm with clearly resolved nucleosomes (Figure 3.4 i) and linker DNA (Figure 3.4 j). We also identified several distinct higher order supranucleosomal structures such as stacks and rings (Figure 3.4 k, l). We rendered the 3D volume of the chromatin in the volume viewer in FIJI (Figure 3.4 f, g). The voxel intensity of the tomogram was used for color-coding. The chromatin chain was comprised of 11 - 18 nm "core" regions with high DNA density (Figure 3.4 g, pink) surrounded by the 3 - 8 nm "shell" with low DNA density (green). The total diameter of the chromatin chain (core and shell) ranged from 14 to 26 nm, supporting the size of the fibrous polymer previously identified using ChromEMT.

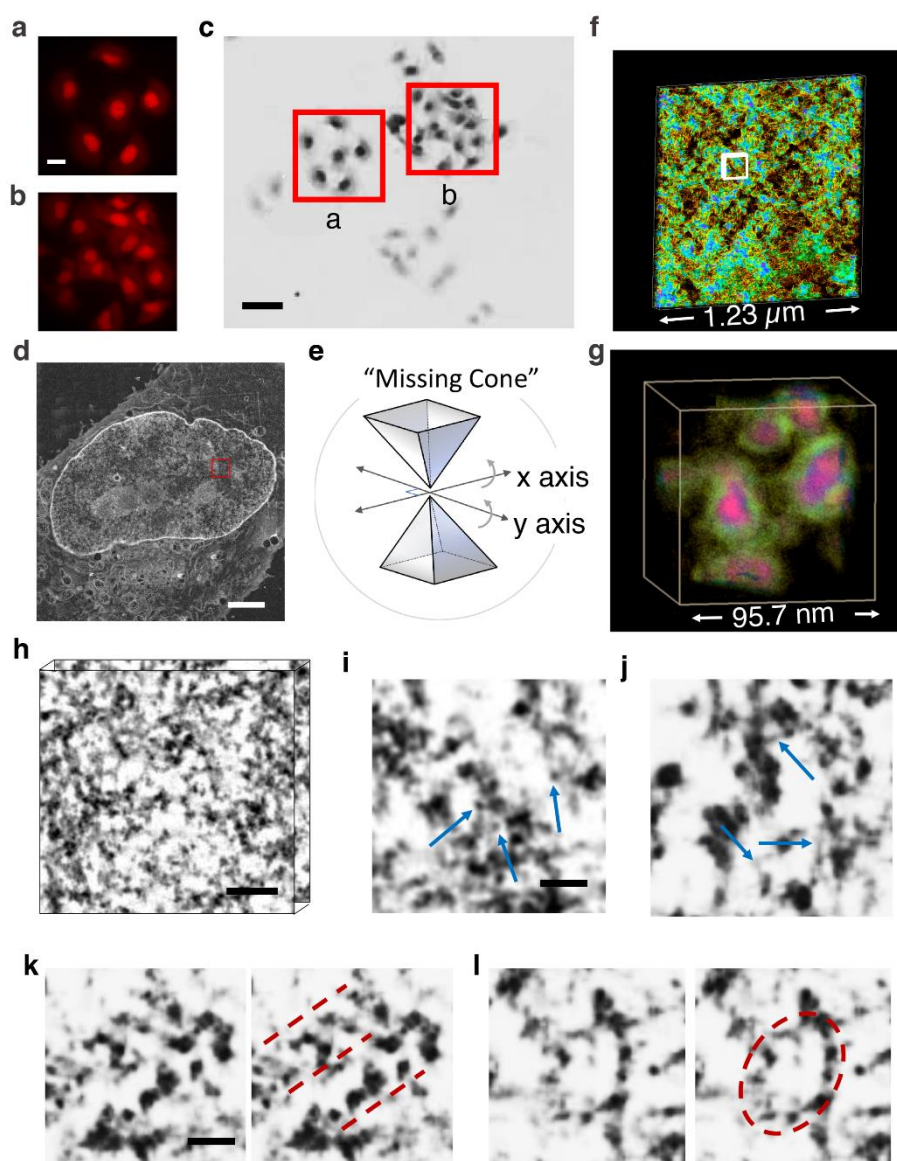


Figure 3.6 ChromSTEM tomography reconstruction of the chromatin of an A549 cell. (a-b) The DRAQ5 photo-oxidation process takes 7 min for each region of interest. Scale bar: 10 μm . (c) The labeled regions were more stained than the nearby regions (red squares; the letter corresponds to the regions in the left panels). Scale bar: 20 μm . (d) STEM image of A549 cell in HAADF mode. Scale bar: 2 μm . (e) Schematics for dual-tilt tomography. The sample

was tilted from -60° to 60° with 2° increment on two perpendicular axes. (f) 3D rendering of the chromatin organization, the pseudo color was based on the intensity of the tomograms. (g) A magnified view of the region labeled by a white square in (f). In (g), pink and green represent high and low DNA density regions, respectively. (h) 3D tomography of the A549 chromatin. Scale bar: 120 nm. (i-l) The fine structure of the chromatin chain: Nucleosomes (blue arrows in (i)), linker DNA (blue arrows in (j)) supranucleosomal stack (red dashed line in (k)) and ring (red dashed circle in (l)). Scale bar: 30nm.

3.2.4 ChromSTEM Imaging of Tissue Biopsies

It is of notice that the cell morphology *in-vitro* can be different from that of the same cell types in tissue bed. For this reason, it is crucial to extend ChromSTEM imaging platform to tissue biopsies as well. Unlike single-layered cultured cells, the tissue biopsy spans a few millimeters in all dimensions. Such significant volume, thickness, in particular, exert extreme challenge in labeling due to diffusion inefficiency inside the tissue. To overcome this issue, we developed a protocol to pre-process the tissue sample to adapt ChromSTEM sample preparation and demonstrated on a mouse ovary tissue biopsy. Upon harvesting, the tissue biopsy was embedded in low-melting temperature agarose and sectioned to 40 μm thick sections and deposited into a petri-dish treated as a cultured cell for the following ChromSTEM protocol. Though through 40 μm , there will be a few layers of cells, we did not observe significant differences between the staining strength in each layer, and the image quality is highly comparable to that of cultured cells.

Fluorescence image of the 40 μm section of mouse ovary tissue was shown in Figure 3.5 a. The DRAQ labeled double strand DNA specifically. The photo-oxidized area was identified after resin embedding using optical microscopy in the bright field due to the darker contrast (Figure 3.5 b, red dashed line). Overall, the tissue bed contains various cell types, as seen in Figure 3.5 (c-j). Particularly, oocyte (g), columnar (h), theca (i) cell showed typical morphological characters. Like A549 cell prepared by ChromSTEM reported in the previous section, the contrast inside the nucleus for the tissue biopsy is continuous, as opposed to the binary contrast in conventional TEM staining.

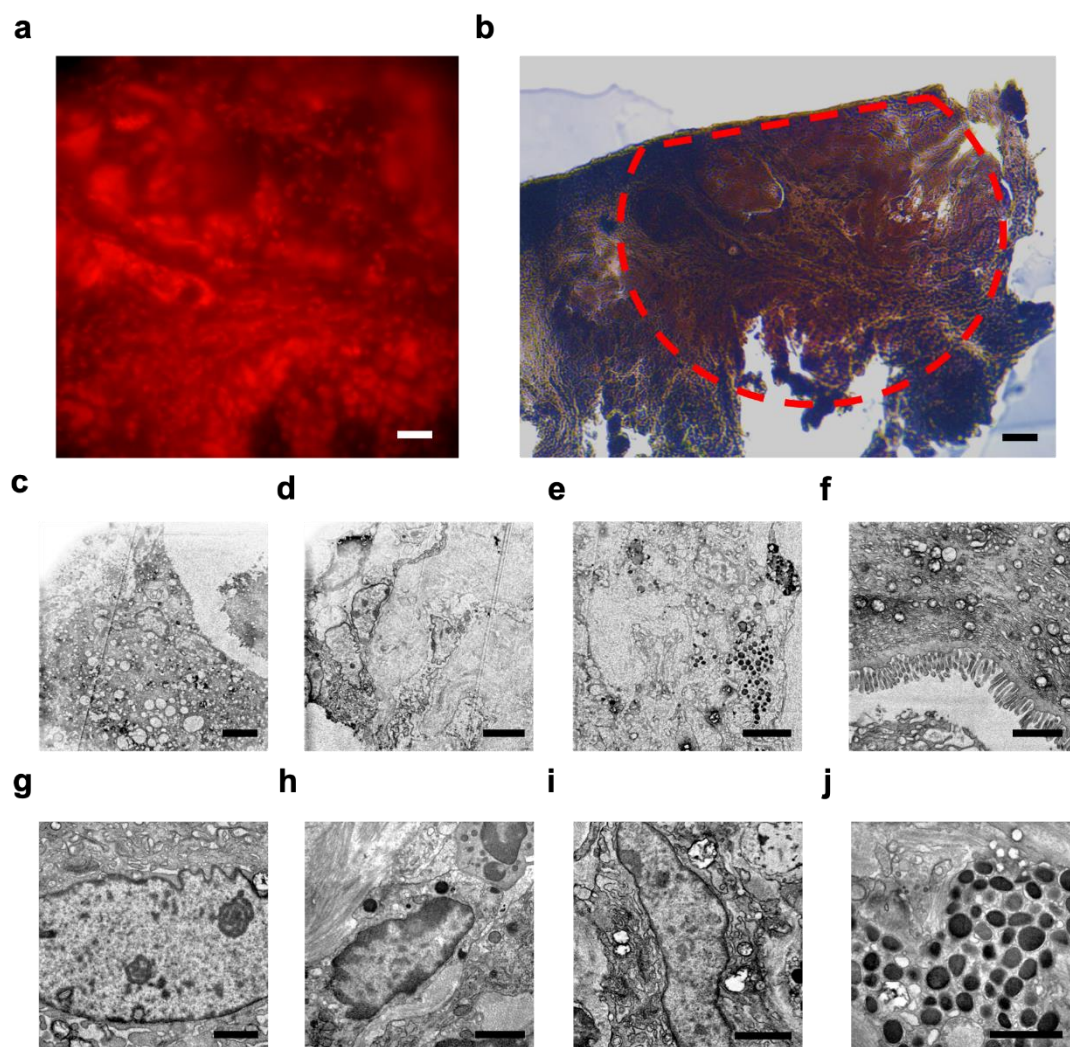


Figure 3.7 ChromSTEM of mouse tissue biopsy. We modified the original protocol for cultured cells to tissue samples. Semi-thin agarose sections of the tissue were prepared, and DRAQ5 was employed to label the double strand DNA specifically. (a) Fluorescence image of a 40 μm thick agarose section during photo-oxidation. Scale bar: 100 μm . (b) After resin embedding, the photo-oxidized region was clearly identifiable due to dark contrast. The red dashed line marked the region with photo-oxidation. Scale bar: 200 μm . (c-j) STEM imaging of the tissue prepared by ChromSTEM on a 120 μm resin section. Different morphologies of

the tissue bed were preserved, and four types of commonly seen cell types in the ovary were observed. Scale bar: (c-e) 5 μm , (f-j) 2 μm .

3.3 Quantifying 3D Genome Organization Using ChromSTEM

Three major methods were employed in quantifying the 3D chromatin architecture through ChromSTEM: mass-scaling analysis, DNA packing density analysis, and chromatin positioning analysis. In all three metrics, we identified nanoscale chromatin domains or clusters that can be separated spatially.

3.3.1 Internal Structure of Chromatin Packing Domains

Topologically associated domains (TADs) are functionally defined, sub-Mbp scale genome structures that might be comprised of several chromatin loops. TADs are believed to play a critical role in gene transcription by increasing interactions between loci located within the same domain and, equally importantly, insulating genes from genomic regions located in neighboring domains¹⁶⁰. Whether TADs are physical elements of chromatin packing or statistics of an ensemble of chromatin states across a cell population has been a subject of an ongoing debate¹⁶¹. While most experimental HiC data have been acquired at the cell population level (with the exception of lower resolution single-cell HiC)¹⁶²⁻¹⁶⁴, TAD-like nanocompartments and nanoclusters have been reported with super-resolution techniques at the single cell level^{165,166}. Given its high spatial resolution and the ability to image a population of cells, ChromSTEM has the potential to address some of these controversies.

In polymer physics, the mass-scaling is the relationship between the material M within concentric circles of radius r and the radius r . For a fractal structure, the mass scales as $(r) \propto r^D$, where D is the power-scaling exponent or fractal dimension. In reality, the fractal structure can be altered by the physical-chemical environment, and the critical length scale where the mass-scaling deviates from power law is defined as the fractal domain radius. Similar to other polymeric systems, the scaling behavior of chromatin describes the relationship between the physical size (radius r) of a chromatin region and the genomic length (chromatin mass or the number of base pairs, M) contained within it: $M \propto r^D$, where D is the chromatin packing density scaling or the fractal dimension of a given chromatin domain. D of an unconstrained free polymer in equilibrium may range from $D = 5/3$ (for an excluded volume polymer) to $D = 3$ (for space-filling polymer) depending on the balance between the free-energy of polymer-polymer and polymer-solvent interactions. D is further modulated by constraining processes, such as chromatin loops. If a polymer forms a number of spatially uncorrelated domains, the mass-scaling of the supradomain structure (i.e., r is greater than the domain size) is also 3, but the structure is no longer fractal at these length scales. Importantly, the mass-scaling is translationally invariant, regardless of the choice of the center of the concentric circles. To characterize the domain structure, we performed the mass-scaling analysis.

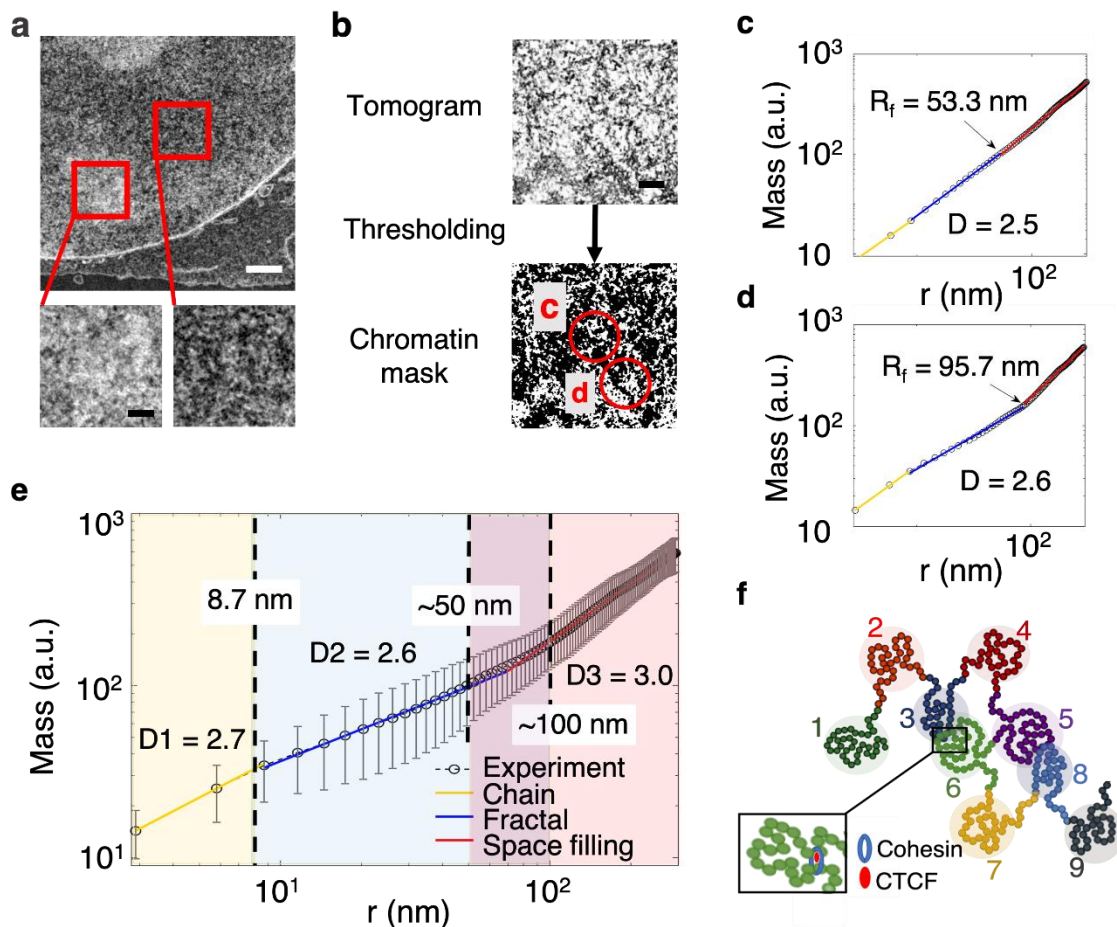


Figure 3.8 The internal structure of chromatin packing domains. (a) STEM HAADF image of an A549 cell nucleus shows that the chromatin is organized into compartments (light and dark image contrast), which consist of smaller domains (insets). Scale bar: 1 μ m; inset scale bar: 300 nm. (b) For each virtual 2D slice, automatic thresholding was applied to create a binary chromatin mask. The mass scaling analysis was performed inside a circle with a radius of 300 nm. Scale bar: 120 nm. (c-d) Examples of the mass scaling curve for chromatin regions highlighted by red circles c and d in (b). In (c-d), Mass is defined as the mass of chromatin that is enclosed by a ring with inner radius r and the width of 2.9 nm (1 pixel). Three distinct

regimes of mass scaling can be identified: the chromatin chain regime (yellow data points and regression line), the packing domain with a fractal internal structure (blue), and the supradomain structure (red). The fractal dimension (D) and the radial size (R_f , defined as the upper length scale of fractality) of domains varied across domains. (e) The average mass scaling of 4096 randomly centered regions on each of the 33 tomograms. The error bar is the standard deviation. Three regimes of mass-scaling behavior can be identified: the chromatin chain regime (yellow) with $r < 8.7$ nm, fractal regime (blue) with the average fractal dimension $D = 2.6$ and 8.7 nm $< r < 50$ nm, space-filling regime of spatially uncorrelated packing domains (red) with scaling exponent = 3 and $r > 100$ nm. In between the fractal region and space-filling region ranging from 50 nm to 100 nm (purple), we observed a smooth increase of the scaling exponent, which indicates variability in packing domains sizes. (f) Schematic of the packing structure of chromatin that is suggested by the ChromSTEM data. The schematic shows 9 chromatin fractal packing domains, some of which might be formed by loop extrusion (inset) or non-loop extrusion mechanisms. We hypothesized that the chromatin is organized into spatially uncorrelated and segregated packing domains with various sizes and fractal dimensions. While some of the domains might be spatially isolated (domains 1,2,7,9), others may interpenetrate at the domain periphery as a result of decreasing chromatin density (domains 3 and 6, 5 and 8). For both configurations,

the mass scaling outside of the domain is the same as the dimensionality of the space the chromatin is embedded in, 3.

Figure 3.6 a shows a HAADF image of an A549 cell nucleus, which indicates that the chromatin organized into multiple packing domains (insets). Prior to mass-scaling analysis, the chromatin position was segmented by automatic thresholding with Li's method in FIJI as previously reported (Figure 3.6 b)¹⁶⁷. For each scaling analysis, concentric circles with radius from 2.9 nm (1 pixel) to 290nm (100 pixels) were employed, and non-zero pixels were chosen as the origin of the mass-scaling on the binarized chromatin mask. As the stack is only 100 nm thick, we employed mass-scaling on each virtual 2D slice then averaged through z-direction to get average mass-scaling for the local region. We plotted the chromatin mass enclosed by a ring with inner radius r and a single pixel width (discrete increment of the mass-scaling) as a function of r for different chromatin regions (Figure 3.6 c-d, red circles in (b)). From the average mass-scaling curve estimated from 4096 randomly centered chromatin regions (Figure 3.6 e), three regimes of the power-law scaling behavior can be identified: the chromatin chain region (yellow, $r < 8.7$ nm), the fractal region (blue, $8.7 \text{ nm} < r < 50 \text{ nm}$, $D = 2.6$), and the space-filling region (region, $r > 100 \text{ nm}$, $D = 3$). The transition between the fractal to the space filling region ranges from 50 to 100 nm (purple), suggesting that at the supranucleosomal scale chromatin is organized into spatially uncorrelated ($D > 3$ at the supradomain scale) fractal packing domains with different sizes (100 - 200 nm in diameter) and fractal dimensions ($D < 3$ within domains) (Figure 3.6 f). While some domains are spatially isolated, others appear to be interpenetrating as a consequence of decreasing chromatin density at the domain periphery (Figure 3.7).

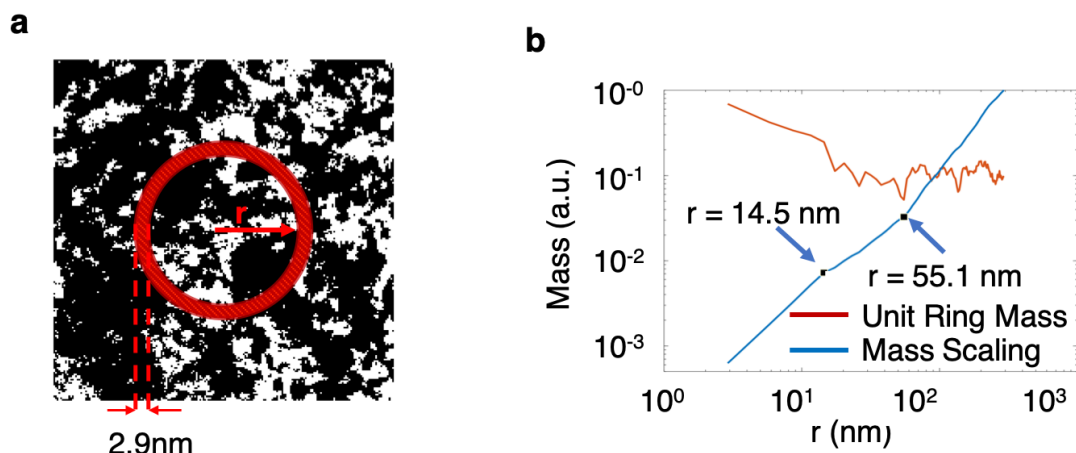


Figure 3.9 Mass-scaling and density scaling. (a) The mass scaling of the fractal region was calculated as described. The density distribution was the unit mass on the ring with inner radius r and bandwidth of 2.9 nm (1 pixel). (b) The mass scaling and unit ring mass (density) for the mask in (a). Two transitions are present. In $r < 14.5$ region, the density decreases following a power law. In $14.5 \text{ nm} < r < 55.1 \text{ nm}$, the density keeps dropping but with oscillations but overall following the same scaling as expected from a mass fractal. At $r = 55.1 \text{ nm}$, the density increases sharply. In $r > 55.1 \text{ nm}$, the density oscillates but maintains the baseline. This behavior indicates the interpenetration of the domains.

3.3.2 ChromSTEM Analysis of Nanoscale Chromatin Packing Domains

We further investigated the local chromatin domain structure shown by the mass-scaling curve by calculating CVC, the average DNA concentration, the size of the packing domains, and the DNA content fraction for the domain.

Calculating Average, Variance of DNA Concentration and CVC

As STEM HAADF contrast originates from Rutherford scattering, the tomography intensity is proportional to and can be converted to the physical mass of DNA. We normalized the tomogram to its highest intensity to extract the DNA concentration in each voxel. We assumed the highest voxel intensity corresponded to dehydrated DNA ($2\text{g}/\text{cm}^3$), or the voxel was permeated only with DNA. Then the new voxel intensity corresponds to the fraction of the voxel is DNA (0.5 mean 50% space is occupied by DNA with a density of $1\text{g}/\text{cm}^3$). Then we employed a moving 3D cube (95.7 nm in each dimension and stride of 2.9 nm) to analyze the local chromatin packing. We mapped the mean and the variance of DNA concentration within the cube on the normalized tomogram (Figure 3.10 a-b, e-f). We adopted the definition of CVC from previous work³², and obtained the CVC using the same cube dimension on the binarized chromatin mask by calculating the fraction of non-zero voxels in each cube (Figure 3.10 g). For ultrathin sections, the moving cube (a square with thickness) was anisotropic, the height of the cube was limited by the section thickness. Nonetheless, the lateral dimension of the square was chosen such that the volume stayed the same as the one used in tomography data: we used 170 nm wide square for 30 nm sections and 147 nm for 40 nm sections. We calculated the average and the variance of DNA concentration from normalized STEM projection images and proofed that no or minimal error was introduced compared to true 3D analysis (Figure 3.8).

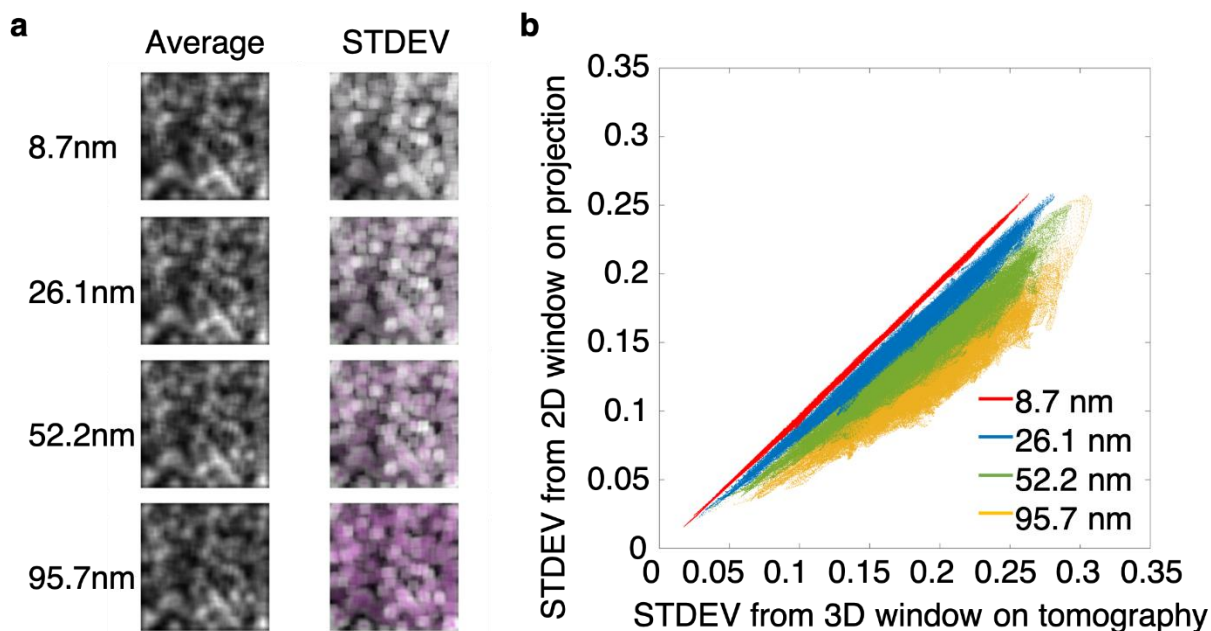


Figure 3.10 Influence of projection at varying thicknesses to the average and the standard deviation of the DNA concentration. We projected various numbers of the virtual 2D slices after tomography reconstruction to form “projections” and calculated the 2D average and the 2D standard deviation (STDEV) of DNA concentration using a 2D window with 95.7 nm on each side. For each projection (thickness), the 3D average and the 3D STDEV were calculated using a 3D window with 95.7 nm in x and y and the thickness of the projection in Z. In theory, the 2D and the 3D average of DNA concentration should remain the same, while the 2D STDEV will be a non-monotonic underestimation of the 3D STDEV. (a) We coded the 2D metrics magenta and the 3D metric green and overlaid them for different thickness. For each pixel, a perfect match of the two will result in black and white contrast; a mismatch will result in colored contrast. As expected, for all thickness, the average from 2D and 3D window matched perfectly. While for STDEV, the mismatch increases rapidly as the

thickness of projection increases. (b) The STDEV calculated from the 2D window on the projection was plotted against the STDEV calculated from the 3D window on the tomography to quantify the extent of underestimation given this chromatin structure at different thicknesses. From 8.7 nm to 95.7 nm, the ratio of 2D STDEV to 3D STDEV kept decreasing, indicating at a larger thickness, the STDEV is more severely underestimated. Meanwhile, the spread of the curve at larger thickness is also significantly wider, indicating non-monotonic, irreversible smearing of the STDEV. However, at small thickness (ultra-thin section) such as 8.7 nm, the slope is 1, and the spread is minimal, indicating almost no smearing of the STDEV. For 26.1 nm projection, the slope is 0.9 with an r^2 equals to 0.99 in the linear regression, suggesting that the STDEV from the projection is sufficiently accurate to serve as the proxy of the real STDEV from tomography with a pre-factor difference.

To render more physical value, we first estimated the range of average DNA concentration for the whole nucleus on the thick section with tomography data (Figure 3.9) and scaled the average DNA concentration from ultrathin sections to have the same range, and we employed the same pre-factor in rescaling the variance of DNA concentration.

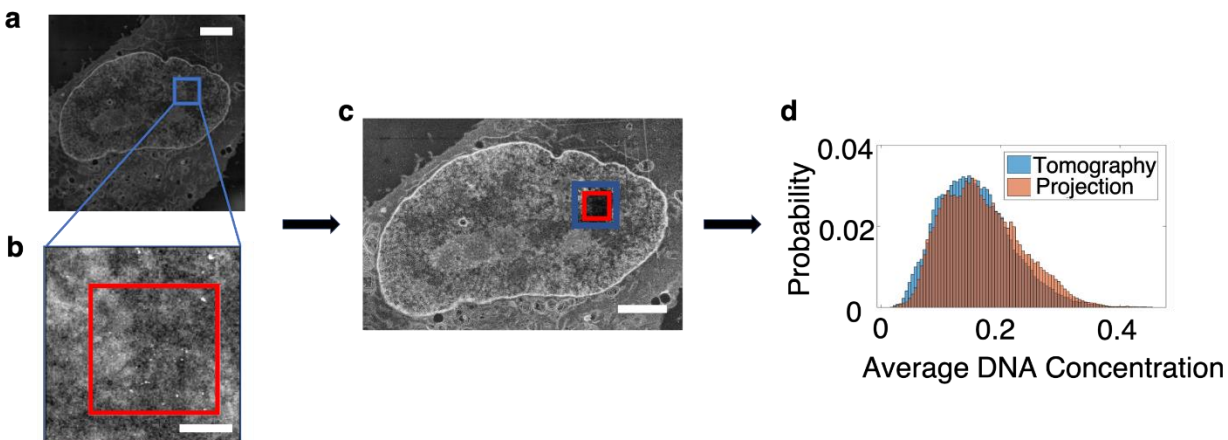


Figure 3.11 Alignment of the tomography region to the whole nucleus and the normalization of the average DNA concentration of A549 cells. To quantify the DNA concentration for the entire nucleus, the tomography region was registered to the whole nucleus using cross correlation with openCV2 packing in Python, and the average DNA concentration calculated from the whole nucleus image was normalized to the average DNA concentration calculated directly from the tomography. (a) A larger ROI (blue square) including the tomography region, was selected for the automatic registration. Scale bar: 2 μm . (b) The tomography region (red square) was registered to the ROI. Scale bar: 500 nm. (c) Overlay the tomography region (red square) and the ROI (blue square) onto the whole nucleus image. Scale bar: 2 μm . (d) The histogram of the average DNA concentration of the tomography region but calculated from the whole cell projection (orange) was normalized to the average DNA concentration calculated from the tomography (blue). The coefficients were used to normalize the DNA concentration for the whole nucleus. We observed small discrepancies for the average DNA concentration calculated from the tomography and projection even after

normalization. We believe the difference in noise level at two image condition might be the reason. Importantly, the majority of the histograms match perfectly.

Domain Size

From tomography data, we identified nanoscale packing domains with similar average or variance of DNA concentration. To estimate the size of the domains, we manually selected 23 domains and calculated the full-width-half-maximum of the line profile across the domain (Figure 3.10 c). To obtain the fractal dimension of each domain, we first segment the domains from the DNA concentration map using intensity thresholding and watershed algorithm.

Domain Fractal Dimension and Radius from Mass-Scaling Analysis

Similar to mass-scaling analysis for the entire field of view, for each domain, we calculated the average mass-scaling curve centered on every non-zero pixel within the domain for each slice in the binarized 2D chromatin mask. We quantified the average fractal dimension by calculating the power law exponent on the average mass-scaling curve and coded every pixel using the same fractal dimension within that domain (Figure 3.10 i). We estimated the fractal domain radius by finding the spatial separation with 1% deviation from the power-law scaling on the average mass-scaling curve. Violin plot was employed to show the distribution of fractal dimension and fractal domain radius for 44 domains (Figure 3.10 l-m).

DNA Content Fraction Analysis

The CVC is the fraction of space chromatin occupied, and the average DNA concentration is the fraction of space DNA occupied. We divided the average DNA concentration by the CVC for the same moving cub to calculate the fraction of DNA on chromatin (Figure 3.10 h). We plotted the average DNA concentration vs. CVC for each pixel and performed linear regression considering all data points to separate two packing schemes (Figure 3.10 j): DNA-poor (above the regression line) and DNA-poor (below the regression line).

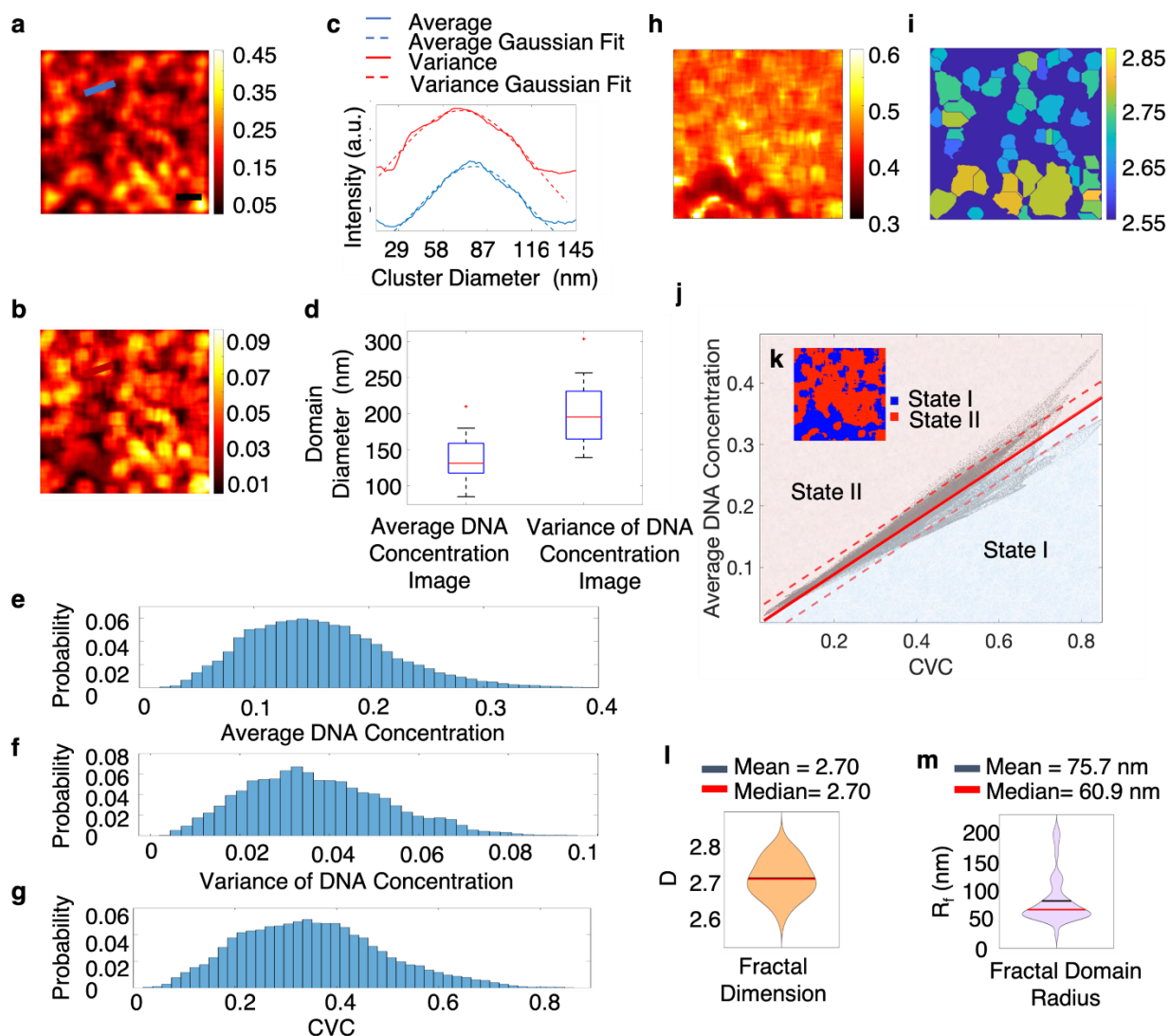


Figure 3.12 Chromatin is organized into spatially separated nanoscale packing domains. (a) The average DNA concentration and (b) the variance of DNA concentration both show chromatin packing domains. Scale bar: 100 nm for (a,b,h,i). (c) The diameters of the domains were estimated as the full width at half maximum (HWHF) fitted from the line profile across the domain (blue line in (a) and red line in (b)). (d) Box plot of the domain diameter measured based on the maps of the average and the variance of DNA concentration. Histograms of (e)

the average DNA concentration, (f) the variance of the DNA concentration, and (g) the CVC. (h) The map of the DNA content fraction defined as the ratio of the local average DNA concentration and the CVC. (i) The fractal dimension D for packing domains identified in (a). (j) We identified two distinct states of chromatin packing with differential DNA content fraction (DNA rich vs. DNA poor domains). Redline: the linear regression of the entire dataset. DNA content fraction state I (blue) lies below the regression line, indicating low DNA fraction. State II (red) lies above the regression line, indicating high DNA fraction. The dashed line represents the 95% confidence interval of the linear regression. (k) Segmentation of chromatin based on DNA fraction. Chromatin regions with low DNA fraction (blue) and high DNA fraction (red) in (k) correspond to states I and II in (j), respectively. From the mass-scaling curve for each of the 43 domains segmented by watershed algorithm from (a), we quantified the fractal dimension (l) and fractal domain radius (m).

The CVC histogram shows (Figure 3.10 g) that the most probable CVC for A549 cells is 0.34, which is in good agreement with Ou's measurements for an interphase human small airway cell (SEAC)³². To estimate DNA concentration, we assumed that the highest voxel intensity in the tomograms corresponds to pure unhydrated DNA ($\sim 2 \text{ g/cm}^3$)³² and normalized all tomograms by the highest voxel intensity value. After normalization, DNA concentration 1 corresponds to DNA occupying 100% of the voxel volume or $\sim 2 \text{ g/cm}^3$. The average DNA concentration ranged from 0.006 to 0.38 with the most probable concentration at 0.14, and the variance of DNA concentration ranged from 0.0025 to 0.09 and peaked at 0.0342 (Figure 3.10 e, f).

The tomography data clearly shows significant variability in local chromatin packing. In order to assess chromatin heterogeneity across the entire nucleus, we analyzed ChromSTEM images of 30 nm cross-sections of the whole nucleus of the same cell on which the tomography was performed. The average DNA concentration (Figure 3.10 b) ranged from 0.5% to 62%, and the probability distribution showed a plateau of most probable DNA concentrations from 11% to 22%. The variance of DNA concentration (Figure 3.10 d) ranged from 0.5% to 5.5% and peaked at 1.8%.

The spatial distribution of the domains with similar average DNA concentration (Figure 3.10 a) highly correlated with that of the domains with a similar variance of the DNA concentration (Figure 3.10 b) (0.8 pixel-to-pixel Pearson's correlation coefficient). The size of each domain was estimated as the full width at half maximum (FWHM) of the line profile across the domain (Figure 3.10, a blue line, b red line, c). Twenty-three domains were analyzed. The average diameter was 137.0 +/- 5.27 nm and 199.1 +/- 8.14 nm for domains defined based on their average DNA concentration and DNA concentration variance, respectively.

Notice that the highest CVC is 0.8 while the highest average DNA concentration is 0.4, indicating that the additional ~50% of the chromatin volume should be occupied by non-DNA molecules such as protein, which were not stained by the chromEM method. We then investigated the congruency of the CVC and the DNA concentration properties of chromatin in terms of DNA content fraction by dividing the average DNA concentration by CVC in the same moving cube (Figure 3.10 h). Linear regression was performed for data from all locations in the chromatin (Figure 3.10 j, regression line: solid red, 95% confidence interval: dashed red). As shown in Figure 3.10 k, the chromatin appears to fall into one of the two states: the DNA-poor (Region I) and the

DNA-rich (Region II) based on whether the DNA content fraction is greater than the slope of the regression line. Nearly all packing domains could be classified into one of the two states (DNA-poor vs. DNA-rich), although the difference was more pronounced for domains with high average DNA concentration. Indeed, the boundaries of domains defined based on their average DNA concentration and the DNA content fraction were nearly identical (Figure 3.11). The mechanism behind such differential chromatin packing is unclear but might be related to phase separation^{34,168}.

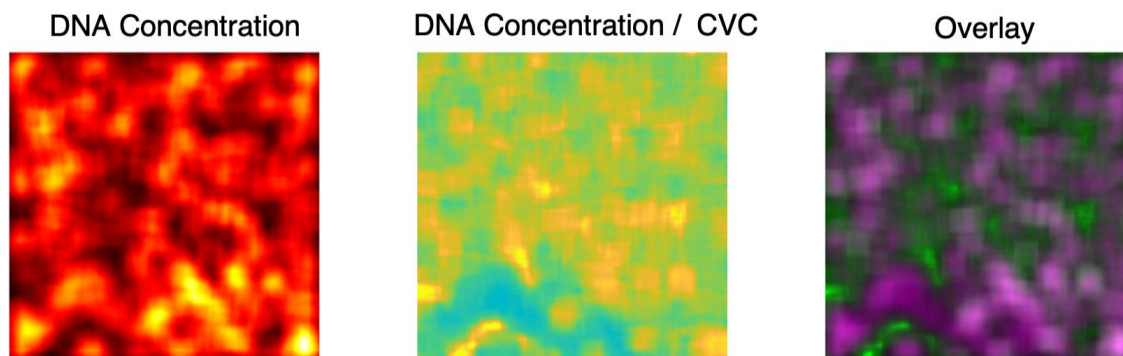


Figure 3.13 Comparing cluster boundaries in the DNA concentration and the DNA concentration / CVC. To investigate the spatial distribution of cluster identified independently in the DNA concentration map (left) and the DNA concentration/CVC ratio map (middle), we overlaid the two maps with false coloring (right). In the overlay image, the magenta denotes the DNA concentration, and the green represents the DNA concentration/CVC ratio. Qualitatively, the clusters have similar boundaries and spatial distribution. However, the cluster with high DNA concentration can have an arbitrary value

of DNA concentration/CVC ratio, which leads to low pixel-to-pixel cross-correlation coefficient (-0.13).

For the fractal dimension D (Figure 3.10 i, l) and the upper size of domain fractality R_f (Figure 3.10 m) for packing domains segmented by watershed algorithm from the average DNA concentration map. D was obtained from the mass-scaling curve ($M(r) \propto r^D$), and R_f was estimated as the largest r for which the mass-scaling curve does not deviate from the power-law by more than 1%. Both mean and median D for all 43 domains was 2.7 ± 0.008 . The mean and median R_f was 152.1 ± 12.28 nm and 127.6 nm, respectively, in agreement with the domain size estimated from the average DNA concentration. In terms of the genomic size for the packing domains, given that the mean DNA concentration within a 95.7 nm^3 cube is 0.157 ($\sim 0.314 \text{ g/cm}^3$), the average molecular weight for single nucleotide is 325 Daltons, and the radius of the domain is 50 - 100 nm, we estimated that the packing domains contain 100 to 400 kb, comparable to the typical size of TADs.

3.3.3 Comparison of Chromatin Packing for Different Nuclear Compartments

Although it is frequently assumed that heterochromatin is denser compared to euchromatin, the difference in DNA density in these compartments is a subject of an ongoing debate. Some studies suggest that heterochromatin is significantly denser than euchromatin with implications that the transcriptional suppression in heterochromatin might in part be due to its higher density, which limits molecular diffusion processes. Other studies suggest that heterochromatin is only marginally denser than euchromatin¹⁶⁹. To provide quantitative data to address this question, we

developed a segmentation method to identify heterochromatin by thresholding the average DNA concentration map from both the tomography data and the 30 nm cross sections of the nucleus. We quantified the heterochromatin volume percentage within the A549 cell nucleus using STORM (Figure 3.12).

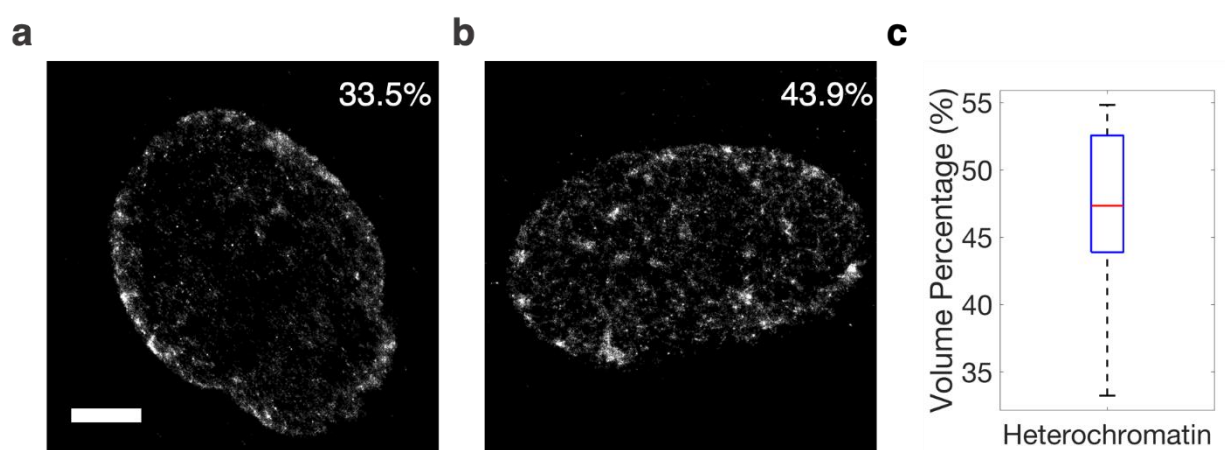


Figure 3.14 STORM of A549 to quantify heterochromatin volume concentration. To quantify the average volume percentage of heterochromatin for A549 cell, the H3K9me3 and anti-H3K27me3 were labeled, and STORM images were taken for multiple cells. The ratio of pixels with signal and total pixels of the nucleus was used to represent the average heterochromatin volume percentage. (a) and (b) Examples of STORM images with 43.8% and 54.2% heterochromatin, scale bar: 3 μ m. (c) Distribution of heterochromatin volume percentage for 4 cells at in total 10 different focal planes, the average heterochromatin volume concentration is calculated to be 47% and used in heterochromatin segmentation from the average DNA concentration map.

On average, the heterochromatin accounts for 47% of the total chromatin. Assuming the heterochromatin is denser than the euchromatin, we calculated that the threshold of average DNA concentration that provided a 47%-53% split for A549 cells was 0.2. Regions with the average DNA concentration above 0.2 were considered heterochromatin and the rest euchromatin.

With this segmentation, the mean DNA concentration of heterochromatin (0.28) was approximately 2-fold higher than that of euchromatin (0.15). We also compared the variances of DNA concentration (Figure 3.13 g) and CVC (Figure 3.13 h) for the tomography data and the variance of DNA concentration (Figure 3.13 k) and the distance between euchromatin and the nuclear envelope (Figure 3.13 l) for the cross-section data. The latter will provide a complete view of the chromatin intra-cellular heterogeneity. In both cases, heterochromatin showed a larger mean-variance than euchromatin. Regarding CVC, we observed a small overlap between heterochromatin and euchromatin. We also found that heterochromatin primarily resided along the inner nuclear membrane, with a small portion scattered across the whole nucleus: more than half of heterochromatin was adjacent to or within 500 nm from the nuclear envelope while only 7% of the euchromatin located within that range.

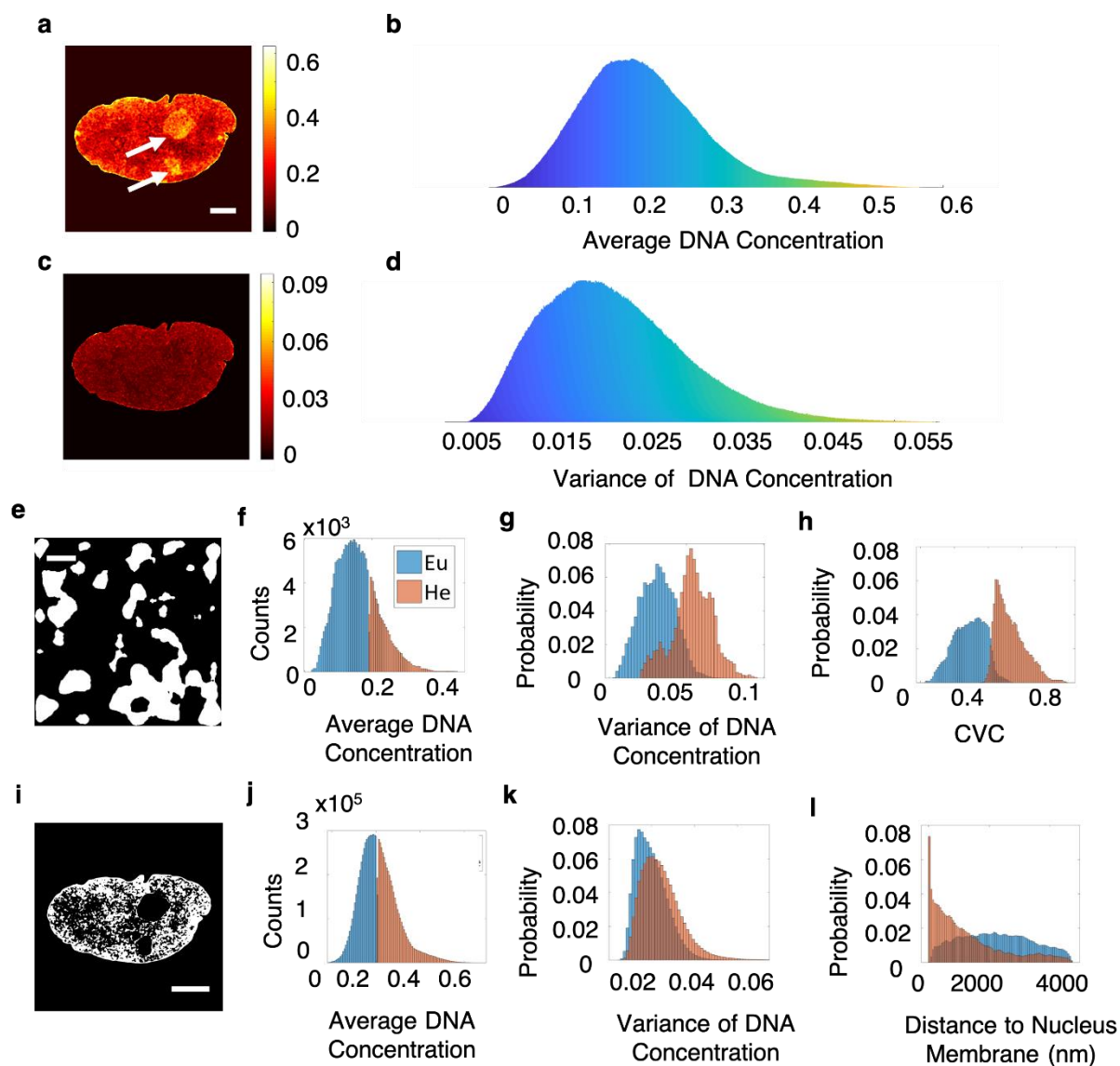


Figure 3.15 Packing properties of chromatin in different nuclear compartments. (a) The spatial and (b) the statistical distribution of the average DNA concentration calculated for a 30 nm section of A549 cells. Scale bar: 2 μ m for (a) and (c). The nucleoli are clearly identifiable (white arrows in (a)). (c) The spatial and (d) the statistical distribution of the variance of the DNA concentration for the same sample. (e) Mask for heterochromatin segmentation based on the tomography data. Scale bar: 200 nm. (f-h) Differences in the

average DNA concentration, the variance of the DNA concentration, and the CVC between euchromatin (blue) and heterochromatin (orange). (i) Mask for heterochromatin segmentation for the cell in (a), the nucleoli were removed from the mask. Scale bar: 3 μm . (j-l) Differences in the average DNA concentration, the variance of the DNA concentration, and the distance to the nuclear envelope between euchromatin (blue) and heterochromatin (orange).

3.3.4 Comparison of Chromatin Packing for Different Nuclear Compartments in Mouse Ovary

It is becoming increasingly accepted that cell behavior *in situ* might, in many instances, be different from that in a cell culture, which may potentially apply to chromatin structure and function. We, therefore, demonstrated the ability of ChromSTEM to quantify chromatin structure in tissue samples. 40 μm sections of mouse ovary tissue embedded in agarose were labeled following the ChromEM protocol, and 120 nm resin section was imaged with STEM HAADF contrast (Figure 3.14 a-e). Contrary to the findings in the A549 cells, we observed a clear differentiation in image contrast between euchromatin and heterochromatin, with the heterochromatin appearing significantly brighter than the euchromatin. The average DNA concentration was calculated for each cell and normalized to have the same range as the average DNA concentration of the A549 nucleus (Figure 3.14 f). The normalization did not influence the shape of the DNA concentration histograms. We calculated the probability distribution function of the average DNA concentration (Figure 3.14 f, red line), and the DNA concentration for euchromatin and heterochromatin (Figure 3.14 g). Of note, in all cells measured in the mouse

ovary, the probability density function of DNA concentration had a bimodal shape, as opposed to a single peak in case of the A549 cells. The most probable average DNA concentrations for euchromatin and heterochromatin were 0.195 and 0.468, respectively. Thus, DNA in heterochromatin can be almost 3-fold denser than that in euchromatin, and 2.4 times denser on average. This data indicates that the density of heterochromatin and euchromatin may have significant cell-to-cell variability even for the cells of the same type, suggesting the need to study chromatin organization across cell populations for accurate statistical conclusions.

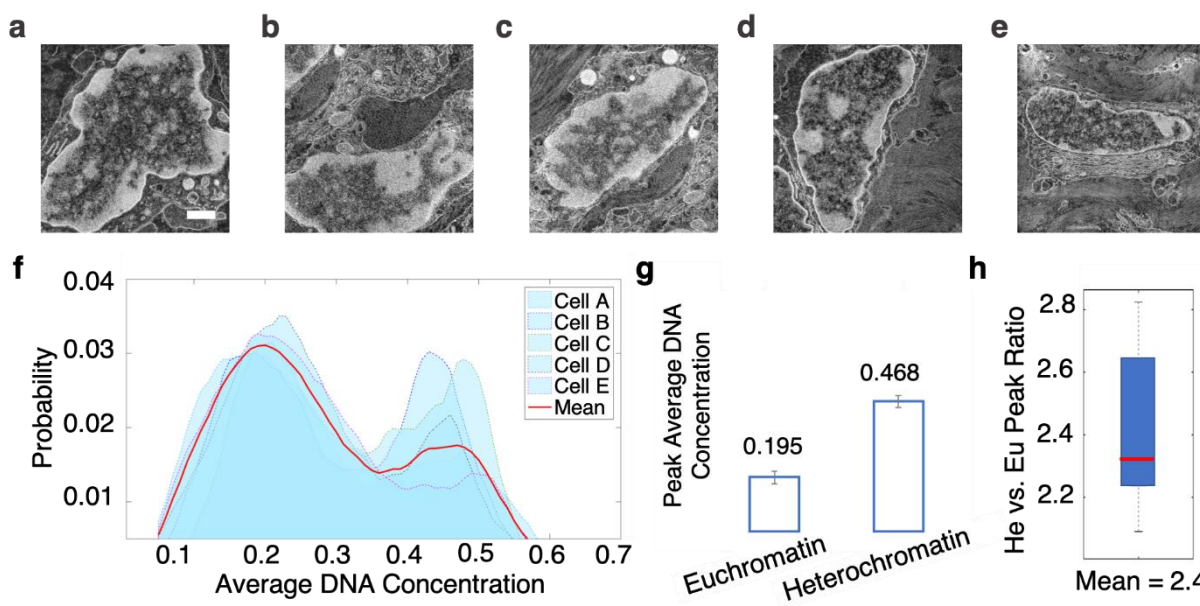


Figure 3.16 Differences in DNA concentration between euchromatin and heterochromatin of cells in the mouse ovary. (a-e) Neighboring cells in the mouse ovary tissue processed with the ChromEM staining. Scale bar: 1 μm . (f) The average DNA concentration for each cell (blue area) and the mean DNA concentration of the five cells (red line). (g) The most probable DNA concentration for euchromatin and heterochromatin. (h) The distribution of

the ratio between the most probable DNA concentration within heterochromatin (He) and euchromatin (Eu) in each cell. On average, DNA concentration in heterochromatin is 2.4 times higher than that in euchromatin.

3.4 Discussions and Conclusions

We developed a novel imaging platform to study 3D genome organization, ChromSTEM, by incorporating STEM tomography and imaging with Z-contrast into the original ChromEMT framework that provides contrast through DNA-specific staining. Importantly, obtaining the average and the variance of DNA concentration from the analysis of thin sections has minuscule error compared to the information gained from 3D tomography (Figure 3.8), which demonstrates the potential of the ChromSTEM platform for high-throughput chromatin analysis through thin section imaging. We demonstrated the versatility of ChromSTEM by quantifying the local chromatin packing structure and positioning through statistical metrics such as the scaling of the chromatin polymer, CVC, the average and the variance of DNA concentration, the DNA content fraction, and the localization of low- and high- density chromatin within the nucleus for cells *in vitro* as well as *ex vivo* tissue. Although the assumption that the ChromEM staining is stoichiometric does not hold at small length scales (single nucleotide) due to the diffusion inefficiencies of the dyes, in this work we utilized the binarized chromatin mask for the mass-scaling analysis. Moreover, the average and the variance of DNA concentration were estimated within a super-voxel. At the super-voxel level (100 nm on each side), we can assume the staining strength is uniform. Enhancing staining efficiency will improve the precision of ChromSTEM significantly at small length scale and should be the focus of future research.

Utilizing ChromSTEM, we observed a “core-shell” structure of the chromatin chain (Figure 3.4 i) with the diameter comparable to that of the disordered polymer chain reported using ChromEMT by Ou et. al. At the supranucleosomal level, we identified a high spatial heterogeneity of CVC that ranged from 6% to 74% and peaked at 34%, again, in agreement with the previous ChromEMT results. We also identified spatially distinct packing domains with 100 - 200 nm in diameter and quantified their internal CVC and the average and the variance of DNA concentration. Importantly, the domains could be divided further into two types based on their DNA content fraction: DNA-rich vs. DNA poor. DNA-poor domains are expected to have a substantially higher fraction of other molecular constituents such as proteins. Although these two alternate states of chromatin domains appear to exist in both euchromatin and heterochromatin, the difference between the two states was more pronounced in heterochromatin.

For most polymeric system, the 3D conformation can be described by several critical length scales: 1. the size of the basic chain size; 2. a 3D structure formed by the basic chain, which is typically characterized by a fractal (power-law) scaling; 3. the upper boundary of the fractal packing. While a polymer with uniform properties along its linear chain would typically form a single fractal conformation, polymers with linear properties that vary along their linear chain may form multiple fractal domains with distinct internal structure, in part driven by phase separation. As histone states, DNA methylation, loop formation, and DNA supercoiling may influence chromatin conformation. It is likely that chromatin is an example of the latter (Figure 3.6 f). We utilized ChromSTEM to elucidate the 3D conformation of chromatin across all these length scales and also to better understand the origin of the high heterogeneity of DNA density. We observed a three-regime power-law relationship between chromatin physical and genomic size (Figure 3.6 b):

the chain region ($r < 8.7$ nm, $D = 2.7$), the supranucleosomal fractal domain (r above 8.7 nm and below 50 - 100 nm, $D < 3$, with D varying across domains with the average $D = 2.6$), and the space filling supradomain region ($r > 100$ nm, mass-scaling = 3). Both the length scale of the transition from the fractal to the space filling region, as well as D , varied across domains, supporting the existence of multiple fractal chromatin structures. The average genomic size of the fractal domains was 100 to 400 kbp, comparable to the median size of a TAD. Similar values of D and domain sizes were reported by small angle neutron scattering and fluorescence correlation spectroscopy¹⁶⁹. Models predict that such fractal structure imposes moderate diffusion hindrance by euchromatin, which is independent of the size of a diffusing molecule up to 100 nm diffusion range and should allow most biological macromolecules and even large macromolecular complexes access their targets within euchromatin¹⁷⁰. On the other hand, the high DNA concentration and CVC of heterochromatin is likely to significantly reduce chromatin accessibility, which may foster a transcriptionally silent state. This is also consistent with Molecular Brownian Dynamics simulations of transcription that have shown a dramatic suppression of diffusion of transcription factors in chromatin when its CVC exceeds 50%¹⁷⁰.

At the chromatin compartment level, our data indicate that heterochromatin has a substantially (more than 2-fold) higher DNA concentration compared to euchromatin, which potentially addresses a perplexing question of the differences in density between euchromatin and heterochromatin with some of the prior studies suggesting that euchromatin is considerably denser than heterochromatin while others arguing that the two compartments may have comparable density. In future studies, precise segmentation of chromatin compartments based on labeling histone markers using the correlative 3D optical super-resolution and electron microscopy will need to be

performed to further improve the measurement of chromatin compartments. Future studies may also elucidate whether the two types of DNA-rich vs. DNA-poor domains correspond to functionally distinct states of chromatin such as the gene-rich or gene-poor subtypes.

**CHAPTER 4 RECONSTRUCTION OF 3D AUTOCORRELATION FUNCTION FROM
2D AUTOCORRELATION FUNCTION: CORRELATIVE SCANNING
TRANSMISSION ELECTRON MICROSCOPY AND ATOMIC FORCE
MICROSCOPY**

Essentially all biological processes are highly dependent on the nanoscale architecture of the cellular components where these processes take place. Statistical measures, such as the autocorrelation function (ACF) of the 3D mass-density distribution, are widely used to characterize cellular nanostructure. However, conventional methods of reconstruction of the deterministic 3D mass-density distribution, from which these statistical measures can be calculated, have been inadequate for thick biological structures, such as whole cells, due to the conflict between the need for nanoscale resolution and its inverse relationship with thickness after conventional tomographic reconstruction. To tackle the problem, we have developed a robust method to calculate the ACF of the 3D mass-density distribution without tomography. Assuming the biological mass distribution is isotropic, our method allows for accurate statistical characterization of the 3D mass-density distribution by ACF with two data sets: a single projection image by Scanning Transmission Electron Microscopy (STEM), and a thickness map by Atomic Force Microscopy (AFM). Here we present validation of the ACF reconstruction algorithm, as well as its application to calculate the statistics of the 3D distribution of mass-density in a region containing the nucleus of an entire mammalian cell. This method may provide important insights into architectural changes that accompany cellular processes.

4.1 Previous Work on 3D Characterization of Mammalian Cells

Abnormal changes in chromatin ultrastructure are a hallmark of many pathological processes, including carcinogenesis, diseases of cell differentiation, and apoptosis. One of the main statistical methods to characterize these alterations is the autocorrelation function (ACF) of the 3D spatial distribution of nuclear mass-density¹⁷¹. In recent studies, a significant increase in correlation length and changes in the shape of chromatin mass density ACF¹⁷² have been reported in cancer as independent prognostic factors for cancer survival and detection^{173,174}. This difference in nanoscale ACF, in conjunction with advances in modeling light scattering¹⁷⁵, allowed optimizing imaging modalities for early cancer screening and diagnosis¹⁷⁶.

Conventionally, ACF is calculated directly from the deterministic 3D mass-density distribution within a sample volume. To get the deterministic nanoscale 3D mass-density distribution, electron tomography (ET) using Z-contrast is routinely conducted for thin biological samples¹⁷⁷⁻¹⁷⁹. However, as the sample thickness (volume) increases, the resolution of a reconstructed tomogram decreases rapidly, as dictated by the Crowther criterion^{180,181}. To achieve sub-10 nanometer resolution, an alternative method is to employ time-consuming and experimentally challenging serial sectioning and conduct ET on each slice.

4.2 The Workflow of the Reconstruction Method

In this study, we developed a novel algorithm under the assumption of a statistically isotropic mass density distribution in a biological sample in order to recover the ACF from a single projection image and a thickness map. The method enables measuring ACF without the need to

know the 3D mass-density arrangement, and thus avoids the need for tomographic reconstruction. On the one hand, the spatial resolution of the ACF obtained by this method is not limited by the Crowther's criterion. On the other hand, the time required is significantly less than the thin-slice serial sectioning method for the entire cell nucleus with high axial resolution. The comparison between the conventional method and our method conceptually is shown in Figure 4.1. As a demonstration for this method, we implemented the algorithm using data obtained with STEM and AFM, and successfully reconstructed the nuclear ACF of a human buccal cell.

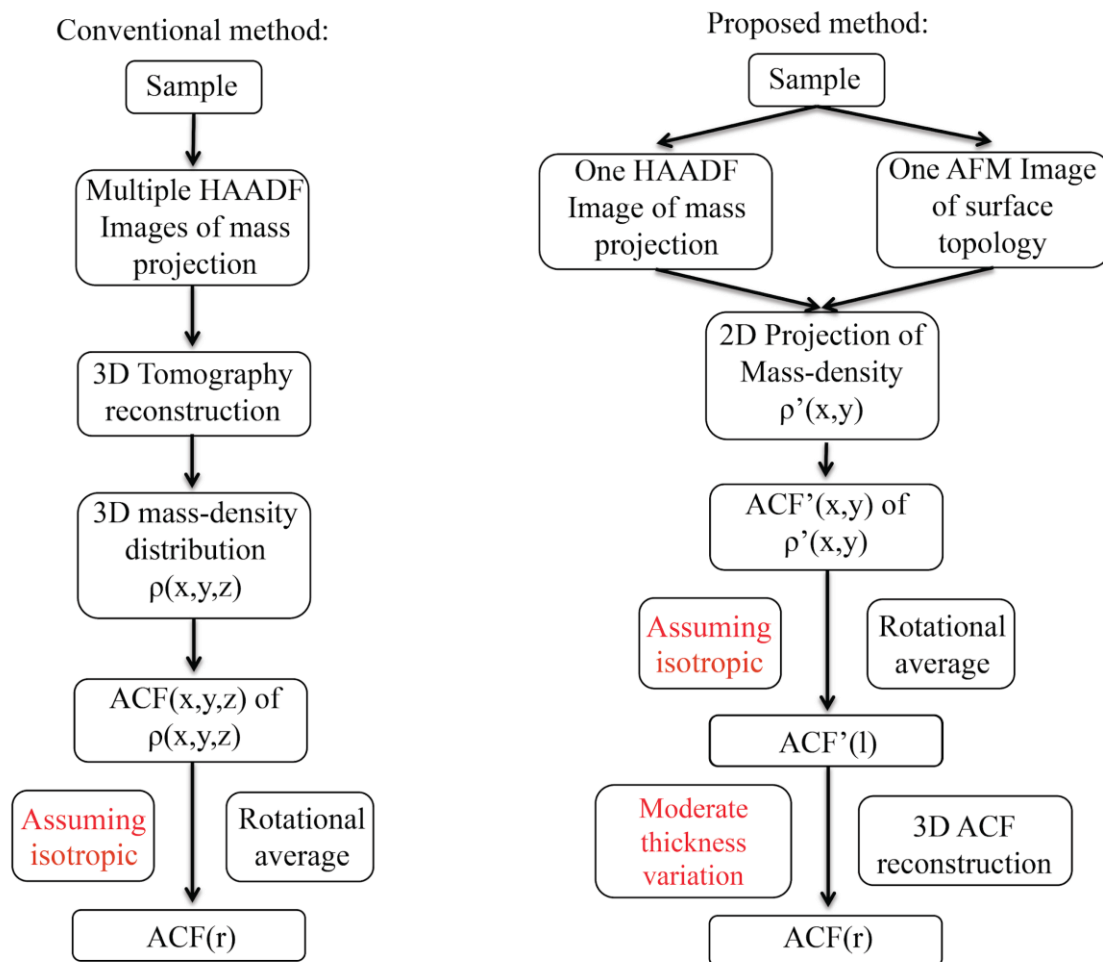


Figure 4.1 Comparison between workflows calculating ACF using the conventional method and the method in this paper. As only one EM image is required in the proposed method, the experimental time and beam damage will be greatly reduced. The resolution of ACF from the new method is not constrained by Crowther's criterion. In addition to assuming the sample is isotropic, the proposed method also assumes the sample thickness is uniform within

the region of interests. However, the error introduced by this assumption is not significant for most biological samples.

4.3 Mathematical Formulation and Numerical Validation of the Algorithm

3D Mass-Density ACF Reconstruction Algorithm

The ACF of the 3D mass-density distribution $B_\rho(\mathbf{r})$ bounded by the size of the sample is a convolution of the ACF of unbounded density spatial distribution $B_r(\mathbf{r})$ and ACF of the top-hat function $A_f(\mathbf{r})$

$$B'_\rho(\mathbf{r}) = \int B_\rho(\mathbf{r}')A_f(\mathbf{r} - \mathbf{r}')d\mathbf{r}', \quad (4.1)$$

where $\mathbf{r} = (l, z) = (x, y, z)$ is the radial distance. Note that $A_f(\mathbf{r} - \mathbf{r}') = Ld(l - l')T(\frac{z - z'}{L})$, with constant L being the thickness of the sample (assuming the sample has uniform thickness) and $T(z)$ is a triangular function, (1) can be rewritten as (4.2)

$$B'_\rho(\mathbf{r}) = \frac{1}{L} \int B_\rho(l, z')T(\frac{z - z'}{L})dz, \quad (4.2)$$

Let $z = 0$, and replace z' with z , we get

$$B'_r(l) = \frac{1}{L} \int B_r(r)T(\frac{z}{L})dz \quad (4.3)$$

The right-hand side of (4.3) is exactly the equation for ACF of 2D distribution of averaged density in the z dimension (projection), so $B'_r(l)$ is indeed the ACF of the density projection in 2D.

Assuming the medium to be geometrically isotropic, we can reconstruct B_r from B'_r by solving (4.3) discretely.

$$B_r = \frac{1}{2Dz} B'_r M^{-1} \quad (4.4)$$

In (4.4) Dz is the step size of discretion, $B_{r,j} = B_r(i \cdot Dz)$, $B'_{r,j} = B'_r(i \cdot Dz)$, $i = 1, 2, \dots, \frac{L}{Dz}$, is the discrete form of $B_r(\mathbf{r})$ and $B'_r(\mathbf{l})$ respectively. $M_{i,j} = r \times T(\sqrt{r_j^2 - l_i^2} / L) / \sqrt{r_j^2 - l_i^2}$ and $M_{i,j} = 0$ for $i > j$, $r_i = j \cdot Dz$, $j = 1, 2, \dots, \frac{L}{Dz}$, and $l_i = i \cdot Dz$, $i = 1, 2, \dots, \frac{L}{Dz}$.

Numerical Validation of the Algorithm and Error Analysis for Sample with Non-Uniform Thickness

Two assumptions were used in the derivation of the algorithm: 1. Sample mass-density distribution is statically isotropic, 2. Sample thickness is uniform. We validated the algorithm numerically using a sample with an isotropic density distribution and a uniform thickness profile. However, for the second assumption, we found out that only small errors will be introduced if we use the mean thickness of the sample for L , given there is a moderate thickness variation, which is true for most biological samples. In other words, the uniform thickness assumption can be dropped while still maintaining the accuracy of reconstruction.

Firstly, we generated two media to demonstrate an ideal sample for the algorithm and a sample where the algorithm would fail. To generate those two samples, one inhomogeneous medium with random mass-density fluctuations was generated using MATLAB (MathWorks, Inc.) and then processed differently¹⁹⁰. The dimension of the inhomogeneous sample is $6 \times 6 \times 6 \mu\text{m}^3$. The dimension of the inhomogeneous sample is $6 \times 6 \times 6 \mu\text{m}^3$. The spatial correlation of the mass

density distribution is described by an exponential function: $B_\rho(r) = \sigma_\rho^2 e^{-r/lc_\rho}$, where σ_ρ^2 is the variance and lc_ρ is the correlation length. In the modeling, we used a σ_ρ of 0.25g/cm^3 and a lc_ρ of 100nm . As the length scale of ACF is much smaller than the dimension of the sample, even if we trimmed half of the sample, the mass-density distribution in the $6 \times 6 \times 3 \mu\text{m}^3$ volume is still isotropic enough (Figure 4.2 a, c). This isotropic sample with uniform thickness is ideal for the algorithm. However, if we compressed the original sample along the z-direction, the mass-density distribution in the compressed medium is no longer isotropic (Figure 4.2 b, d), and the algorithm will fail in such sample.

Thus, we chose the isotropic medium (Figure 4.2 a) for numerical validation of the algorithm. We compared the ACF measured directly from this medium with that reconstructed using our algorithm from the 2D projected image¹⁸².

Finally, as real biological samples do not usually have a uniform thickness, we need to estimate the error of the algorithm for samples without uniform thickness. We generated media similar to the one used in validation but with different thickness variations. We used the mean thickness of the medium in the reconstruction algorithm. The reconstructed ACF was compared to the measured ACF.

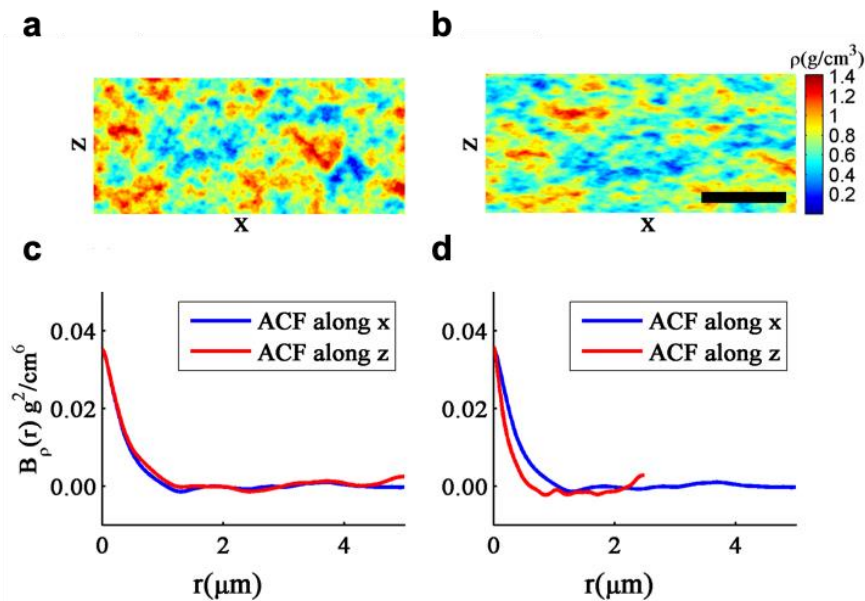


Figure 4.2 Statistically isotropic and anisotropic medium. (a) An isotropic sample with (c) ACF along all direction identical. (b) An anisotropic sample with (d) ACF different along z- and x-axis. Scale bar: 2 μm .

4.4 Materials and Methods

4.4.1 Sample Preparation

Cells from buccal mucosa (cheek cells) were collected using a Cytobrush (CooperSurgical Inc.), suspended in 1 mL 1x PBS and spun for 5 min at 1500 rpm (Fisher Scientific accuSpin; Micro17). The supernatant was aspirated, and the pellet was resuspended in PBS. Droplets of 30 μL of the cell suspension were deposited on TEM grids in a moisture chamber for cell attachment. The chamber was kept in a cell incubator for 4 hours; then the sample was fixed with 2.5% glutaraldehyde and 2% formaldehyde in PBS for 20 minutes at room temperature. After fixation,

the grids were rinsed in DI water before dehydration in a series of graded ethanol. After dehydration, the samples were critical point dried (Tousimis) for STEM imaging.

4.4.2 Quantitative High Angle Annular Dark Field Imaging Through Z-contrast

For samples with a thickness smaller than the electron mean free path, there is a simple linear relation between image contrast $I(x,y)$ in HAADF mode and projected mass

$m(x,y)$ (4.5)

$$I(x,y) = AI_0 \langle \sigma_e \rangle m(x,y), \quad (4.5)$$

where I_0 is the intensity of the incident beam, $\langle \sigma_e \rangle$ is the average elastic cross-section, and A is a constant associated with protein type and microscope settings. By using samples of similar chemical composition with known thickness and density under the same microscope settings, we can calibrate the value of the pre-factor A . For thick biological samples, this relation is affected by absorption and inelastic scattering. By selecting electrons scattered to sufficiently high angle, it is possible to screen out inelastically scattered electrons and maintain the linearity.

To find the rightful imaging condition, we used 5 μ m polystyrene beads as our standard sample as opposed to tobacco mosaic virus. This is because both the chemical composition and the thickness of polystyrene beads are close to the whole cheek cell sample. A STEM (Hitachi HD2300) was used for cell imaging, and all images were taken at 200 kV acceleration voltage with condenser aperture of 75 μ m with a probe current of about 0.7 nA. Polystyrene beads were imaged at different collection angles of the ADF detector as we changed the projection lens current from

1.065 mA to 1.10 mA. Conversion from the projection lens current to the detector collection angle can be found in Table 4.1.

Table 4.1 Camera length, inner and outer semi-collection angle at different projection lens current

<i>Projection Lens Current (mA)</i>	<i>Camera Length (Arbitrary Unit.)</i>	<i>Inner Semi-Collection Angle (mrad)</i>	<i>Outer Semi-Collection Angle (mrad)</i>
1.065	85.7±1.50	72.3	380.2
1.067	86.9±1.29	71.4	375.6
1.070	87.2±1.12	71.1	374.3
1.075	89.2±1.34	69.4	366.3
1.086	90.4±2.04	68.5	361.8
1.091	91.4±0.83	67.8	358.4
1.095	92.7±0.74	66.9	353.9
1.100	93.2±1.25	66.5	352.0
1.125	100.0±1.05	62.0	330.0

We then calculated the linear coefficient between the HAADF image contrast and projected mass of the polystyrene beads at each projection lens current. In order to determine the optimal collection angle, several images of polystyrene beads were taken under different projection length

at a fixed brightness/contrast condition. Projected mass of each pixel, $m_{bead}(x,y)$ was calculated as in Figure 4.3 using the following equation:

$$m_{bead}(x,y) = \rho_{bead} \cdot 2\sqrt{R^2 - r^2} \cdot d^2 r, \quad (4.6)$$

where $\rho_{bead} = 1.05 \text{ g/cm}^3$. For pixels with identical projected mass (identical radial distance to the center of the bead), we averaged the intensities of these pixels to eliminate the influence of noise. Averaged intensity over mass was linearly fitted, and linear coefficients were plotted over the projection lens current. We chose the projection lens current (1.065 mA) which provides a linear coefficient over 0.95 and a good signal-to-noise-ratio for all following experiments.

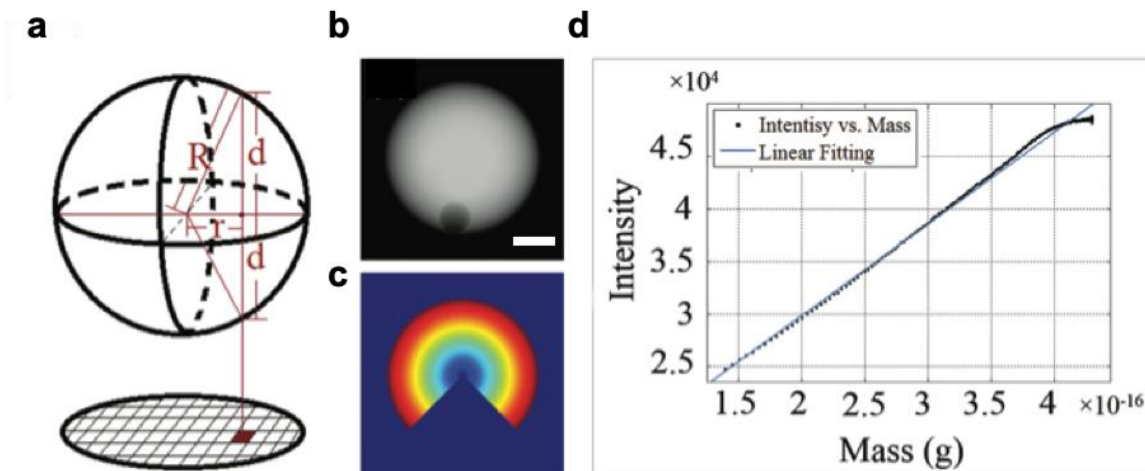


Figure 4.3 Calculation of projected mass in a specific pixel area. (a) R is the radius of the bead, which can be measured as the diameter of the projected circle. r is the distance of the pixel to the center of the circle. d is the thickness of the beads projected to the pixel, $d = 2\sqrt{R^2 - r^2}$. (b) A HAADF image of a polystyrene bead taken under low projection lens

current. Scale bar: 1 μm . (c) The radial distance of different pixels to the center of the polystyrene bead. The intensity of pixels in the same band is averaged. The region with non-polystyrene material was not considered and resulted in a “wedge”. (d) The intensity over mass plot and linear fitting of the bead shown in (b).

4.4.3 Correlative Atomic Force Microscopy (AFM)

A thickness distribution with comparable resolution to the STEM images was required to convert the mass-projection to a density projection. To measure the thickness map, AFM was conducted on the same area of the cell.

In order to create a smooth and rigid substrate for AFM measurement, the grid was glued to a glass slide by epoxy (Devcon 5-minute epoxy). The grid was placed on a region of epoxy much larger than itself and allowed to settle, ensuring the changes in cell height due to the curvature of the epoxy were minimal. To clean the sample surface, the grid was cleaned together with a substrate in a plasma cleaner (South Bay Technology PC 2000). A 2.5 nm Pt film was coated on top of the sample by a high vacuum coater (Leica EM ACE600).

Sample thickness was determined at room temperature by peak force tapping mode using a Bruker Bioscope Catalyst AFM with silicon OTESPA-R AFM probes (Bruker AXS). The low magnification SE and BF images were used to assist co-localization, as SE image provides topographic information of the cell and is more similar to the AFM topographic image, and BF image shows the exact location of the nucleus. To accurately co-register the AFM and STEM images, we conducted the following 3-step algorithm:

1. Locating the center of high magnification nucleus image in low magnification SE image (Figure 4.5 a). The reason to use SE image is that both SE and AFM provide topographic information, and thus the image contrasts are similar. However, from SE image alone, it is impossible to identify the exact location of the nucleus, so we overlapped the high-resolution nucleus image with low magnification TE (bright field) image, and the low magnification TE image with SE image by cross-correlation. Using the translation with the highest cross-correlation, we located the exact region where the high magnification nucleus was taken in SE image.

2. Locating the AFM probe on the sample. We manually engaged the tip to a region with easily identifiable feature (a ridge on the cell membrane) and scanned a small portion of the feature with a pixel size of 5 nm (Figure 4.5 b). While the scanning was still ongoing, we exported the AFM image and aligned it with SE image using affine transform in the MATLAB Image Processing Toolbox. As the probe position is known in the AFM image, and thus known in the SE image (Figure 4.5 c red dot).

3. High-resolution AFM thickness mapping over the region with a nucleus (Figure 4.5 c). We selected roughly the center of the nucleus on the SE image (blue dot) and calculated the offsets between the red and blue dots. Then we moved the probe to the red dot using the control software without withdrawal. A 6 μm -by-6 μm square was scanned with a lateral resolution of 12 nm to cover the entire nucleus. After one full scan, the probe was moved again to another region (yellow dot), a large area with the background and partially overlapped with the nucleus thickness map (background map) was measured. The new offsets and scanning angle were recorded for later registration. Aligning the nucleus thickness map and the background map, we were able to calculate the absolute thickness over the region enclosed the nucleus.

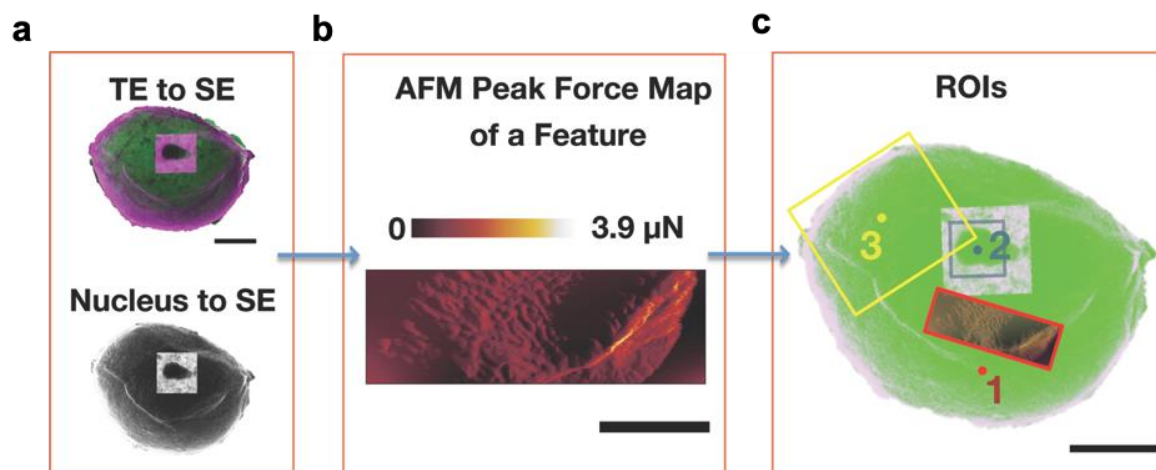


Figure 4.4 AFM experiment flow-chart. (a) We first registered TE image to SE image by cross-correlation, then we registered nucleus to SE image. Scale bar: 10 μm . (b) A small area of features was scanned with low resolution and registered to the SE image. Scale bar: 3 μm . (c) Position of the AFM probe (red dot position 1) while scanning (b), (b) was overlaid on the SE image. Position of the probe while scanning the nucleus (blue dot position 2), and position of the probe while scanning the reference (yellow dot position 3) Scale bar: 10 μm .

4.4.4 Mass and Thickness Mapping for a Human Cheek Cell

The STEM images of a human cheek cell sample (Figure 4.6) were captured under ZC to obtain mass projection. The intensity of grayscale HAADF images is proportional to local mass. The cell images showed clear micro-ridges surface features for cheek cells (typical for squamous epithelial cells). The mass content was low in the upper left corner of the cheek cell in both HAADF and BF images. The significant uneven mass distribution indicated extraction of cellular material, possibly occurred during the serial ethanol dehydration process. For the polystyrene

beads, the linear coefficient between HAADF image intensity and mass projection was calculated to be 0.99. This again proved the validity of using HAADF for mass mapping even for a thick biological sample.

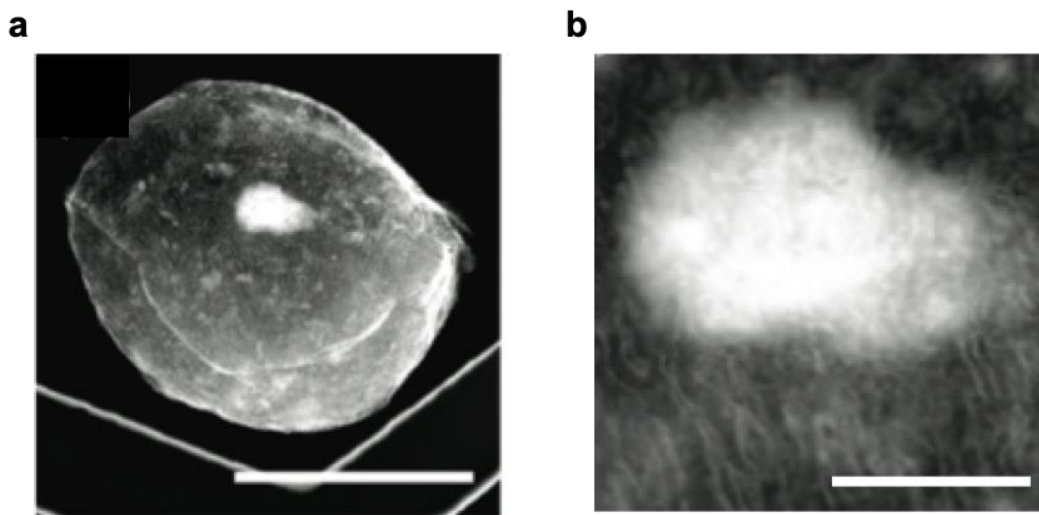


Figure 4.5 STEM images of the same cheek cell. (a) HAADF image of the entire cell. Scale bar: 20 μm . (b) Nucleus region of the same cell. Scale bar: 3 μm .

The AFM images of the selected 6 μm -by-6 μm region with the cell nucleus, the background, and their relative position are shown in Figure 4.7. The mean thickness difference between Figure 4.7 a and Figure 4.7 b of the overlapping area is 4.97 μm . Adding to the relative thickness map, we calculated the absolute thickness of a region over the nucleus. Based on the AFM measurement, we learned that part of this specific cheek cell could be as thick as 11 μm . We also noticed that the nucleus region was not the thickest. In general, the nucleus region is supposed

to be thicker than the cytoplasm region for cheek cells. This observation indicated that the membrane was folded during sample preparation.

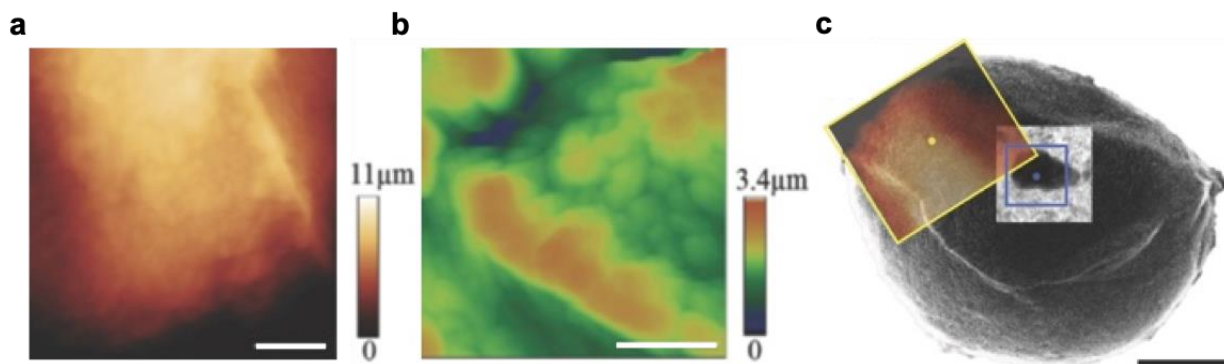


Figure 4.6 Regional thickness distribution measured by AFM. (a) AFM measurement on a large area as reference height. (b) AFM measurement performed on a smaller region enclosing the nucleus, with a lateral resolution of 11 nm to reveal the fine topographic detail. (c) The relative position of the two images. Scale bar: (a) 3 μm, (b) 50 nm, (c) 10 μm.

4.4.5 3D Autocorrelation Function Reconstruction for a Human Cheek Cell

We interpolated and scaled the thickness map so that the pixel size is the same as the mass map. As the membrane of the cell was continuous, this interpolation should give a fairly accurate result after scaling. By dividing the mass over thickness and areal, we got a density projection map $\rho(x,y)$ (**Error! Reference source not found.**). The solid content (wt%) can be calculated directly by dividing $\rho(x,y)$ by the density of condensed dry protein (1.25 g/cm^3). The average solid content in the cytoplasm and nucleus is about 30% and 50%, respectively. The calculated solid content is consistent with the outmost layer of cheek cells.

Furthermore, most optical techniques characterize the mass-density distribution of biological samples with the refractive index (RI) distribution as the variance¹⁸³, which can be calculated $\Gamma(x,y)$ by the Gladstone-Dale relation:

$$n(x,y) = n_0 + \alpha \Gamma(x,y). \quad (4.7)$$

In the equation, n_0 is 1.33, the RI of water, and α is the specific refraction increment of the intra-cellular solids with a chemistry independent value of $\sim 0.17 \text{ mL/g}$. The RI of the sample ranged from 1.4 to 1.45.

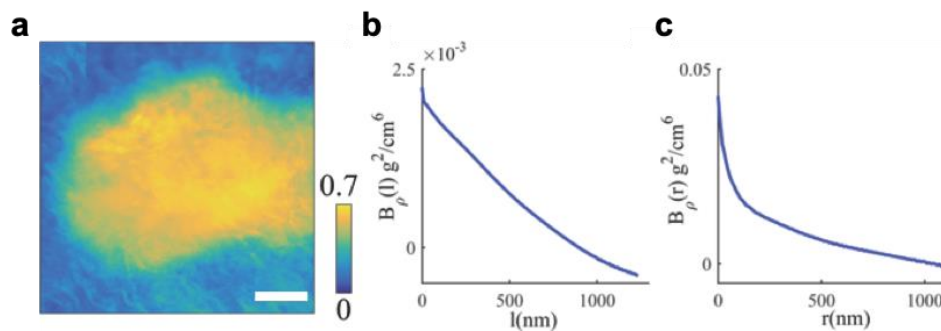


Figure 4.7 Cheek cell mass-density distribution. (a) 2D mass-density projection, scale bar: $1 \mu\text{m}$. (b) ACF of (a) and (c) reconstructed 3D mass-density ACF of (b).

With $\Gamma(x,y)$, we calculated $B_l(l)$, the ACF of the fluctuation of the mass-density and reconstructed $B_r(r)$ using the deconvolution algorithm described before. In the reconstruction, a $2.5 \mu\text{m}$ -by- $2.5 \mu\text{m}$ window over the nucleus that has the least thickness variation was used for a more accurate result. The error was estimated by numerical experiments with the same surface profile. In this specific case, the mean thickness was $7.55 \mu\text{m}$, and the RMS variance was $0.22 \mu\text{m}$,

ensuring σ_ρ^2 and lc_r errors of less than 8%. As expected, $B_\rho(0)$, the variance of the 3D mass-density distribution, is much larger than $B'_\rho(0)$, the variance of the projected mass-density distribution. This is because the averaging process along the z-axis suppressed the fluctuation in the distribution.

To characterize the shape of $B_r(r)$, we fitted the experimentally obtained ACF to Whittle-Matern family of analytical functional forms. Our results revealed a characteristic length of heterogeneity ln of 984 nm, and D_r of 2.95, indicating a fractal mass density distribution. The finding that the ACF is indicative of a mass fractal behavior ($D_r < 3$) is biologically significant, as it provided the experimental confirmation of a prior hypothesis of a mass fractal architecture of chromatin^{184,185}). The correlation length of mass-density (lc_r) is 100 nm, and the standard deviation (S_r) is 0.24 g/cm³. Since RI is linear to mass-density, ACF of RI ($B_n(r)$) has the same correlation length (lc_n) and dimension (D_n) with $B_r(r)$. The standard deviation of RI (S_n) for this specific cheek cell was estimated as 0.04 by using $S_n = S_r \times a$, which falls into the reported value range (0.04 to 0.1)¹⁷³. However, a more accurate statistical measure of the cheek cell mass-density or RI distribution requires further samples.

4.5 Discussions and Conclusions

In this work, we have developed an analytic solution to deconvolute the ACF of the 3D mass-density distribution from the ACF of its 2D projection, assuming the distribution is geometrically isotropic, and the sample thickness is uniform. We also estimated the error of the

algorithm for samples with thickness variations. We discovered that for samples with mean thickness greater than $2.5\mu\text{m}$ and thickness variation less than $3.5\mu\text{m}$, the error of the algorithm was smaller than 10%. In implementing the algorithm to a region of cheek cell containing the nucleus, we calculated the distribution of the mass-density projection from the STEM mass projection and AFM thickness map, the ACF of the 2D mass-density projection, and further reconstructed the ACF of the 3D mass-density distribution with small error.

We believe with better sample preservation method (high-pressure freezing and freeze-drying) and an updated Bioscope, the ACF reconstruction will give a more accurate statistical characterization of the nanostructure in biological samples in their native state. The nanostructure, in turn, may provide valuable information for understanding many cellular biological processes.

CHAPTER 5 INPAINTING ASSISTED CONTROLLED ROTATION TOMOGRAPHY: CORT

Electron tomography (ET) reconstructs three-dimensional (3D) volume from multiple 2D projection images at different orientation (tilt series) of a single specimen. Thanks to the several recent innovations in electron microscopy (EM), including improved sample preparation techniques and novel EM hardware and software, ET has become a powerful technique in biology, as it provides a 3D visualization of morphological features at wide length scales with nanometer resolution. However, interpreting ET results is still challenging due to the artifacts introduced during intensive sample preparation and the structural alterations caused by beam damage in prolonged imaging. Herein we presented a novel sampling strategy, controlled rotation tomography (CORT), for high-throughput tomography tilt series collection for scanning transmission electron microscopy with reduced beam damage while maintaining the reconstruction resolution. In traditional ET, the sample is parked at different orientation for each projection image collection. In CORT, the sample rotates at preset speeds continuously during image acquisition. With both synthetic data and metadata generated from real experiments, we showed that CORT can provide a more even coverage in the sinogram. Combined with inpainting in the sinogram domain and a penalized maximum likelihood (PLM) tomography reconstruction algorithm, CORT can achieve a resolution and quality of reconstruction comparable to the tomography from fully-sampled tilt series, but with a 6-fold reduction in electron dose.

5.1 Radiation Damage for Beam Sensitive Samples

Polymer samples, including most biological samples, experience beam damage under the high-energy electron beam. There are two forms of major beam damage mechanisms for organic samples: radiolysis and knock-on damage¹¹⁵. Radiolysis, on the other hand, is the predominant damage for biological samples. Among radiolysis, the secondary effects (due to secondary electrons) account for a critical part. Radiolysis arises from the inelastic scattering electrons; the energy deposited into the sample can cause the dissociation of molecules and result in the decomposition of the sample (Figure 5.1 a-b, material-loss). For knock-on damage, the momentum transferred during high-angle elastic scattering can cause the displacement of atoms within the specimen or ejections from a surface (sputtering). The threshold incident energy to displace carbon is below 100 keV, and this process does not contribute significantly to the stopping power and the resulting damage. The displacement of hydrogen does not create secondary damage and therefore not too concerning. However, the hydrocarbon generated from the sputtering process is generally re-deposited onto the surface of the remaining sample due to electron charge and result in alterations in morphology (Figure 5.1 c-g, material-gain). During the tilt series acquisition from -60° to 60° with 2° increment at room temperature, a visible layer of contamination was formed and continued to grow in the second half of the collection (red arrow, Figure 5.1 e-g).

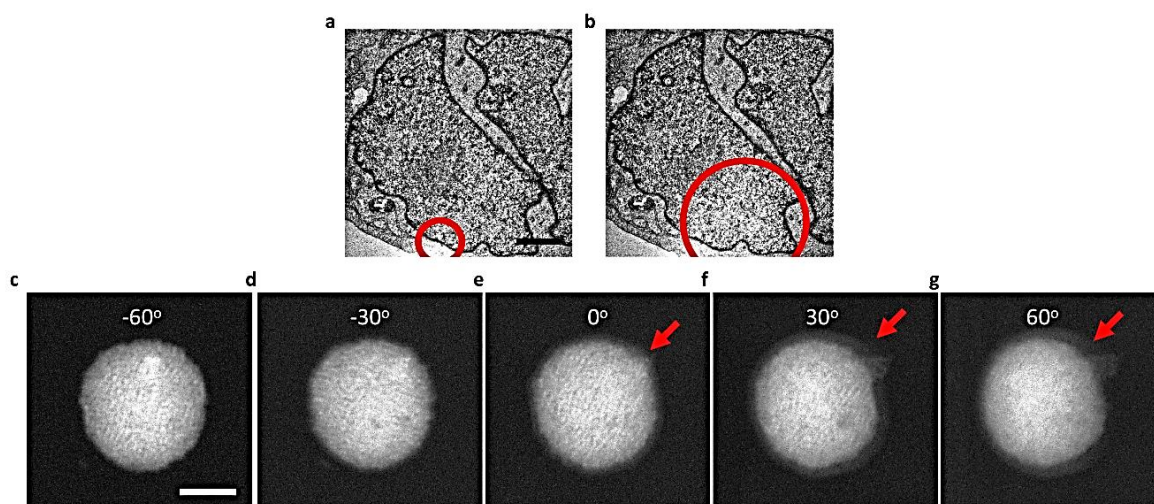


Figure 5.1 Examples of different types of beam-induced morphological changes. (a) and (b), TEM images of the same cell that experienced materials loss due to radiolysis. In (a) red line highlighted the beginning of thinning in the sample. Compared to other parts of the sample, the damaged area appears lighter, indicating less mass. Scale bar: 2 μm . In (b), the beam damaged area expanded. Radiolysis is the primary form of beam damage for the biological sample. (c) and (d), STEM HAADF images of the same lipids-iron nanoparticle construction that experienced the redeposition of hydrocarbons. After prolonged illumination ($\sim 1\text{hr}$), contamination layer formed on the sample in (c) and created a “core-shell” structure in (e-g). The contamination layer is highlighted by the arrows in (e-g). Scale bar: 100 nm in (c).

5.2 Introduction to Sparse Imaging

5.2.1 Sparse Imaging Theory

For a typical tilt series collection, a single object is usually illuminated intensively at high energy. Notably, as the sample usually adopts a “thin-slab” geometry, when tilt to high angles, the thickness that the electrons need to penetrate scales with the cosine of the tilt angle and increased drastically at high tilt (i.e., at 60 ° tilt angle, the effective sample thickness is twice the thickness of the sample in zero tilt). During prolonged illumination at high incident electron energy, the sample experiences constant beam damage. The physical morphology alterations induced by the beam damage will be passed to the tomogram reconstructed as streaking, stretching, and shadowing. To reduce the beam damage for biological samples, the rule of thumb is to make the total dosage as small as possible. However, the trade-off between dose and SNR of the detector draws a hard limit on how many doses we can reduce under current sampling scheme.

The development of the automated data acquisition procedures on EM significantly reduce the unnecessary dose during manual searching, tracking, focusing, and recording of images¹⁸⁶. However, an additional reduction of the electron dose might lead to an unseen resolution for beam sensitive samples such as supranuleosomal complex and macromolecule crowding. While it might seem impossible to limit the number of electrons passing through the sample even further without harm the image quality, recently advancement in theoretical sparse-imaging could provide a solution to this conflict^{84,187,188}. Given the *a priori* knowledge of which components are most significant, it is possible to faithfully reconstruct the ground truth from a severely undersampled image¹⁸⁹. In this “compressive-sensing” scheme, it is possible to significantly down-sample the object while maintaining the final image quality.

In STEM imaging, the converged electron probe raster scans the entire image and therefore embeds redundancy into the data. Theoretically, by “sensing” the part of the sample that is crucial and “ignoring” the other, it is possible to reduce the total electron dose without introducing any artifacts. In practice, the compressible domains and non-trivial coefficients are usually unknown, but this type of information can be estimated by taking a small number of nonadaptive measurements. This sampling method is called “sparse-imaging”, and in principle, it can greatly reduce the acquisition time as fewer pixels are collected. With this sparsely sampled image, multiple in-painting algorithms with machine learning can be employed for reconstructing the full image with high precision. For any in-painting algorithm, there are two critical requirements of a successful recovery of the full image: 1. Incoherent image contrast, 2. Nonadaptive sampling. Secondary electron (SE) image mode and HAADF are both incoherent image contrast, so in principle, both SE and HAADF images can be accurately reconstructed. The key is to design an experimental approach to sparsely sample the image in a nonadaptive (random) fashion.

In the numerical experiment, a HAADF image of a cheek cell nucleus was digitally resampled. A random set of pixels was ignored during resampling, and the percentage of the “missing pixels” was varied to investigate the theoretical limitation on how many doses can be reduced without sacrificing the image quality. A nonparametric Bayesian dictionary learning in-painting method, the Beta-Bernoulli Process Factor Analysis (BPFA) algorithm¹⁹⁰, was employed to recover the missing information. As shown in Figure 5.2 by comparing the features of the reconstructed images with the ground truth, only 20% of the pixels for a quality in-painting. This suggests that the dose reduction by sparse-imaging can be as high as 80%.

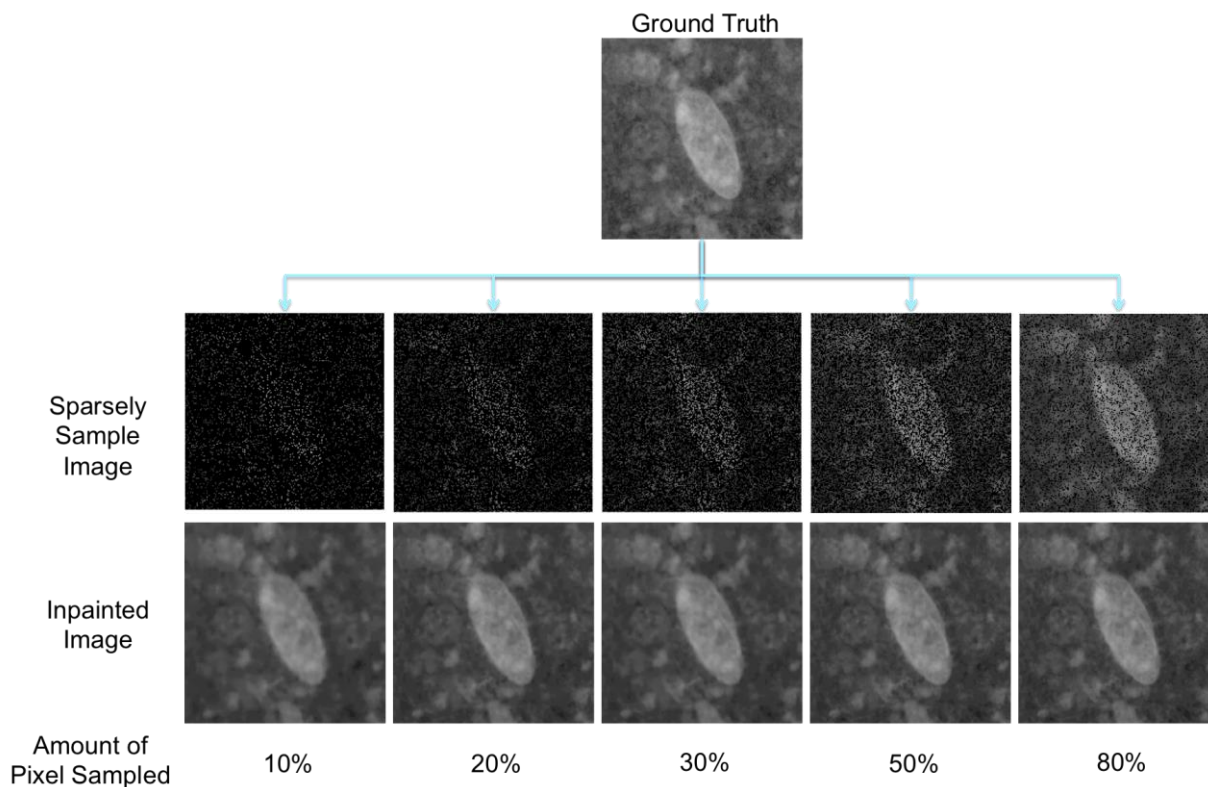


Figure 5.2 Reconstruction (lower panel) from sparsely sampled projection images (middle panel) under STEM HAADF mode. The sparsely sampled images were simulated from the ground truth (top panel) by randomly selecting pixels. The number of pixels samples varies in each column. 20% and above sampling rate provides enough information for the nonparametric Bayesian dictionary learning inpainting method BPFA to recover the full image faithfully for this particular sample.

5.2.2 Experimental Implementation of Sparse Imaging in Electron Microscopy

The first reported implementation of sparse sampling in a STEM is from Hwang's group in Argonne National Lab. Hwang et al. introduced a custom-made software to control the STEM

probe to visit only selected pixels with preset dwell time and reconstructed the full image with great accuracy. However, as there is a significant delay between the software and instrument, and the beam requires time to be stable after moving, the actual dose for sampled pixels does not decrease but increase. In other words, the pixels imaged may be more corrupted; even the total dose is reduced. As each image is reconstructed from the corrupted pixels, it's debatable how many doses this sampling implementation can reduce.

Prior to Hwang, Hujsak et al. from Northwestern University showed that a faithful reconstruction using the BPFA algorithm of SE image of collagen fibers from only 20% of the pixels in a SEM¹²⁴. The under sampling is achieved by using a high-speed beam blanker to deflect beam at pre-selected pixels, and they showed a significant decrease in total dose and sample beam damage. A similar strategy employing a beam blanker should be employed in STEM as well to reduce the total dose. In reality, it is almost impossible to operate a beam blanker to block electrons with an energy of 200keV and above in high-speed. Progress has been made to manufacture a high-speed beam blanker for STEM, but the probe stability is still a big problem. Generally speaking, the nonadaptive measurements have the character of “random” linear combinations of basis/frame elements. However, it has also been shown that even without random sampling, the reconstruction can still be near optimal with a few more measurements. In principle, there is room to design a non-random sampling strategy without additional hardware installment and reduce the dose at the same time.

5.3 CORT Methodology Formulation

Applying the concept of “sparse-imaging”, we developed a novel experimental approach for STEM to reduce the total dose. Traditionally, the sample is parked at a specific angle while the STEM probe raster scans each pixel. In our method, the sample was rotated continuously at one rate, and probe scanned at another (or many others). In each raw experimental image, different parts of the object were visited at different tilt angles. By extracting all pixels of the same angle and aligning them in the sinogram domain, a “sparsely-sampled” sinogram was formed. A 3D wavelet in-painting algorithm was used to recover the missing part of the sinogram. After inpainting, the reconstructed sinogram was treated as a fully sampled sinogram, and conventional tomography reconstruction was conducted. This sampling approach, controlled rotation tomography (CORT) can reduce sample beam damage by 6-folds, and as a generic methodology, it can be potentially applied to any scanning transmission imaging tomography such as STEM, Bio-nano probe, without modification of hardware.

5.3.1 Mathematical Formulation of CORT Sampling

In the continuous rotation sampling, the sample is rotating continuously without stopping while the electron probe raster scans the imaging area. The final image is composed of the different part of the sample at different projection angle. We derived a simple mathematical equation (5.1) to calculate what part (which pixels) of the sample will be recorded at a specific projection angle.

$$n = \text{Quotient}\left(\frac{\theta - \theta_0 + 2k\pi}{\mu_s v}\right) \quad (5.1)$$

In this equation, n is the labeling of each pixel in a raster scan fashion (Figure 5.3), θ is the specific projection angle, θ_0 is the initial angle before recording, $2k\pi$ is the periodicity of angles, k is a non-negative integer, μ_s is the pixel dwell time, and v is the sample stage rotation speed. The dividend is the actual angle covered by rotation; the divisor is the angle rotated through each pixel. As the pixel recording is discrete, we need only the quotient, not the remainder.

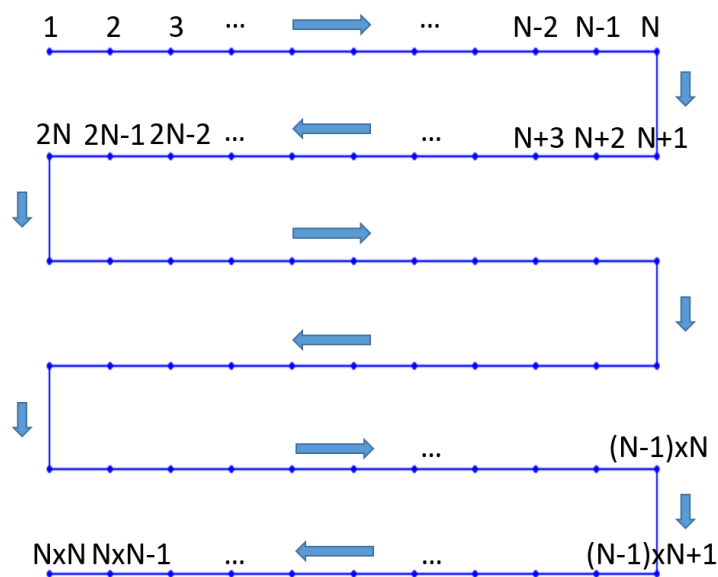


Figure 5.3 Raster scan sampling and pixel labeling. The image size is N by N pixels. Usually $N = 1024$ in a STEM image

From this equation, we can see where to introduce randomness into sampling. We want to keep μ_s constant, as we need consistent SNR. The changeable variables are the initial angle θ_0 and rotation speed v . To change the initial angle, a natural way is to freeze the beam (park the beam at one spot) at any time during recording for any preset time. The rotation speed can be changed

directly through stage control in the microscope. The randomness can be introduced by making θ_0 random, changing of v can assist this process.

5.3.2 Workflow of CORT

The resolution of a tomographic reconstruction is dictated by the number of projections taken at different orientations (Crowther's criterion). For beam sensitive organic and hybrid soft-hard samples, the incident radiation of the electron probe can induce sample damage and prevent the recording of an accurate and meaningful tilt series. To avoid morphological changed due to beam damage, only a reduced number of projections over the angular range is performed, and therefore reduce the resolution of the resulting three-dimensional structure. Herein, we introduced a novel sampling strategy that will increase the number of projection images at different orientation for the same amount of exposure time by sparsely imaging the object in real space for general scanning probe transmission microscopy. Since the amount of information between adjacent pixels in a single projection image is relatively limited, near-randomly under-sampled electron projection images are highly amenable to inpainting to restore an accurate estimation of the true projection. Our scheme can, therefore, maximize the time spent recording pixels with different angular views of the specimen, maximizing the information per unit of electron exposure.

In the conventional acquisition of a tilt series, the sample rotates in a staccato manner, meaning the sample will be parked at a certain orientation and a fully sampled image recorded. We have developed a novel sampling strategy in which the sample will not stop rotating within each image frame while the electron beam is scanning over the grid of defined pixels. The sample and the

scanning probe will move at the same time at different speeds (Figure 5.4). Multiple will be taken during imaging while the sample rotates in a preprogrammed and controlled fashion; thus, the name Controlled Rotation Tomography (CORT). In CORT, although the microscope still outputs individual images, each image frame is composed of pixels captured at different orientations. To process CORT data, the pixels that have the same orientation are sorted into the same frame to form a sparsely sampled projection image. Since typically the scanning speed of the beam is much greater than the rotation of the sample, each pixel will, therefore, be an integration of a very small range of angles observing the specimen. Before reconstructing the tomograms, inpainting algorithms (such as beta process factor analysis, 3D wavelet inpainting, etc.¹⁹¹) was used to fill in missing pixels in the sinogram. The reason to inpaint the sinogram instead of the projection is that under CORT sampling, the mask (pixels that have been visited) in sinogram will form a checkboard pattern and therefore more evenly distributed. After inpainting, the fully recovered sinograms will be used for conventional tomography reconstruction. The workflow of CORT is demonstrated in Figure 5.4.

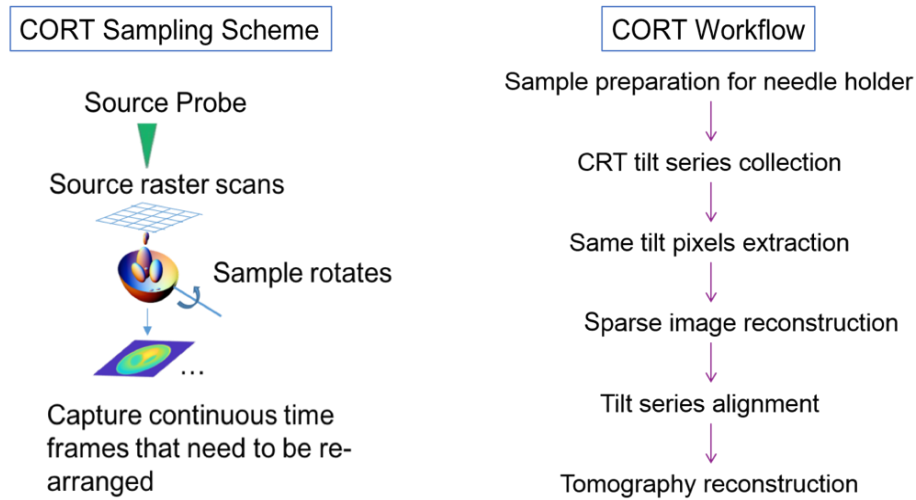


Figure 5.4 Sampling scheme and workflow of CORT. In CORT, the sample rotates non-stop during imaging. To process CORT data, pixels collected at the same sample orientation will be sorted and placed in the same image frame. The undersampled sinogram will be inpainted, and the recovered sinogram will be used in tomography reconstruction.

5.4 CORT Performance Evaluation

5.4.1 Influences of Angular Averaging

In CORT, each projection image is sparsely sampled in continuous rotation tomography. Besides, the signal is also intrinsically different. In conventional tomography, the sample is parked at a specific tilt, and each pixel is a projection of that precise angle. Here, each pixel is an averaged projection over a range of angles. The range $\Delta\theta$ is determined by $\Delta\theta = \mu_s v$. To test the influence of this angular averaging on tomography reconstruction quality, we employed the Shepp-Logan 2D phantom, calculated its 1D Radon slices, and averaged each slice by varying sizes of the mean filter. We then reconstructed the 2D image from filtered 1D Radon slices, and as well as from the

slices with the exact angles (mimic traditional experiment) as the mean of the filter slices, and compared the quality of both reconstructions with the ground truth through mean-squared error (MSE), peak signal-to-noise ratio (PSNR), and structural similarity index measurement (SSIM) (Figure 5.5). Compare to tilt series with angular averaging, the reconstruction from traditional tilt series shows sharper features, especially the three dots in a row at the bottom of the image are almost indistinguishable from each other at 4° averaging window. However, the averaging process also regularizes the noise in the reconstruction, resulting in a higher SSIM at small angles averaging. The data suggests that a rotating speed that no more than 2 degrees averaging per pixel seem to be a good starting point.

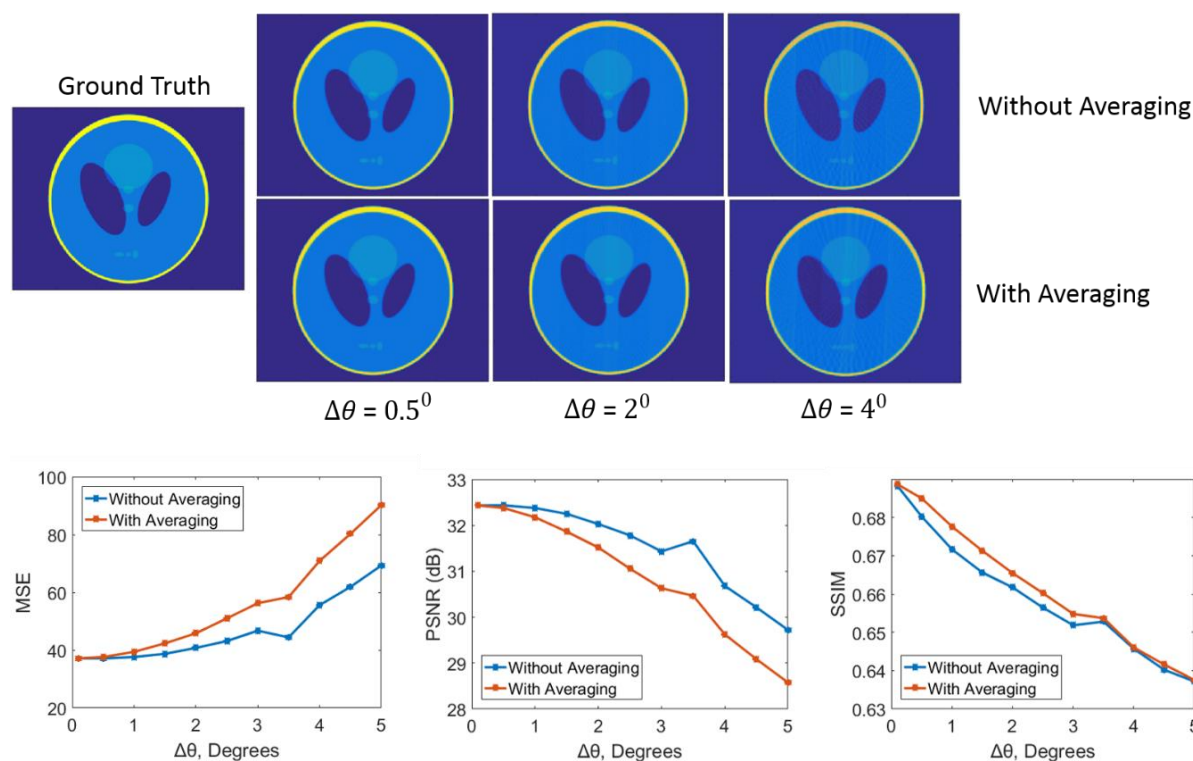


Figure 5.5 Effects of angular averaging in each pixel. Images reconstructed from tilt series with and without averaging of varying window sizes were compared with the ground truth. The reconstructed image from tilt series without averaging shows lower MSE and higher PSNR, indicating it is closer to the ground truth in terms of pixel values. However, the SSIM graph indicates that the image from tilt series with averaging is structural more similar to the ground truth at small averaging windows.

5.4.2 Intuition for CORT Data

In CORT, the sample is rotating continuously at one speed while the electron probe is scanning at a different speed. Under this scheme, the traditional definition of “projection image”

(Figure 5.6 a) does not hold, as different parts of the sample were positioned at different angles within the same CORT image frame (Figure 5.6 b). To interpret CORT data, we sorted the pixels based on their location within the CORT frame and the sample orientation when the pixel was visited by the electron probe. All pixels with the same tilt angle were selected and placed in the same image frame while maintaining their relative spatial positioning. In practice, the pixel dwell time (the scanning speed of electron probe) is on the order of a microsecond, while the sample rotation speed (the tilt speed of the goniometer) is on the order of several seconds. For spatially adjacent pixels (same line), the difference in the tilt angle is minuscule and can be safely neglected based on the previous analysis. We grouped several adjacent pixels within a small range of tilt angles and considered all pixels in the group have the same orientation. The mean tilt angle in the group was used as the nominal projection angle, and the corresponding image was the nominal projection image at this orientation. Intuitively, as the sample rotates slower than the electron probe, for each nominal projection image, some parts of the sample will be missing from the frame, and the parts visited will be in lines (Figure 5.6 c). By sorting the raw CORT data, we created the corrupted, or sparsely sampled projection images.

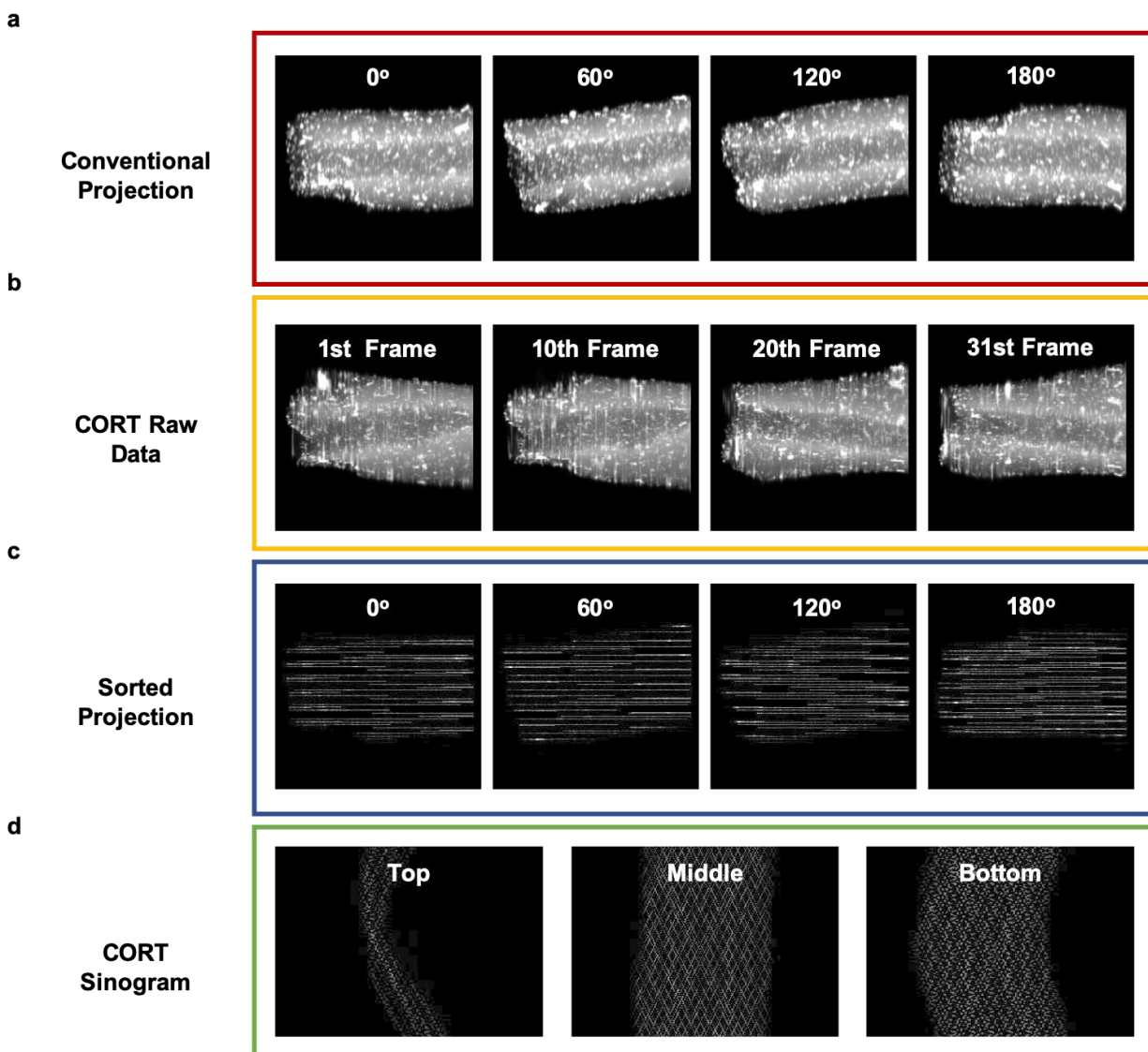


Figure 5.6 CORT data presentation as raw data, sorted projection, and sinogram. (a) The projection images of a double-walled carbon nano-tube with silver particles at different tilt angles (0° , 60° , 120° , 180°). (b) CORT raw data of 31 frames. As the sample is continuously rotated, the traditional tilt angle does not apply here. (c) Sorted CORT data can form undersampled traditional projection image at different tilt angles (0° , 60° , 120° , 180°). (d)

The sorted projection can be rotated and resliced to create undersampled sinogram of the sample (top, middle, bottom).

We further obtained the sinogram for the entire sample by re-slicing the sorted projection images. Unlike the projection images in which the visited pixels form lines, and unvisited pixels form complementary lines, the sorted sinogram shows a checkerboard-like pattern, with visited and unvisited pixels scattering throughout the whole image frame (Figure 5.6 d). Notice that for a faithful reconstruction of the unvisited pixels, the location of the visited pixels should be uncorrelated. In our case, the sinogram provides a significantly better sampling than the projection images.

5.4.3 Sample Rotation Speed and the Distribution of Visited Pixels in the Sinogram

We further investigate how the sample rotation speed influences the mask of visited pixels in the sinogram. In the numerical experiment, a 2D Shepp-Logan phantom was used to generate fully sampled and CORT- sampled sinogram. We generated 31 CORT frames with the same pixel dwell time but varying sample rotation speed. As shown in Figure 5.7, as we increased the sample rotation speed, the spatial distribution of visited pixels was more even with an exception at $v = 67^\circ/\text{s}$. Despite high speed, the sampled sinogram has a sizable void, indicating no information was collected for the projection angles within the void. Lacking sampling coverage at such high speed is due to the periodicity in equation 5.1, suggesting the importance of running *a priori* numerical experiment to optimize the imaging set up, including pixel dwell time and sample rotation speed.

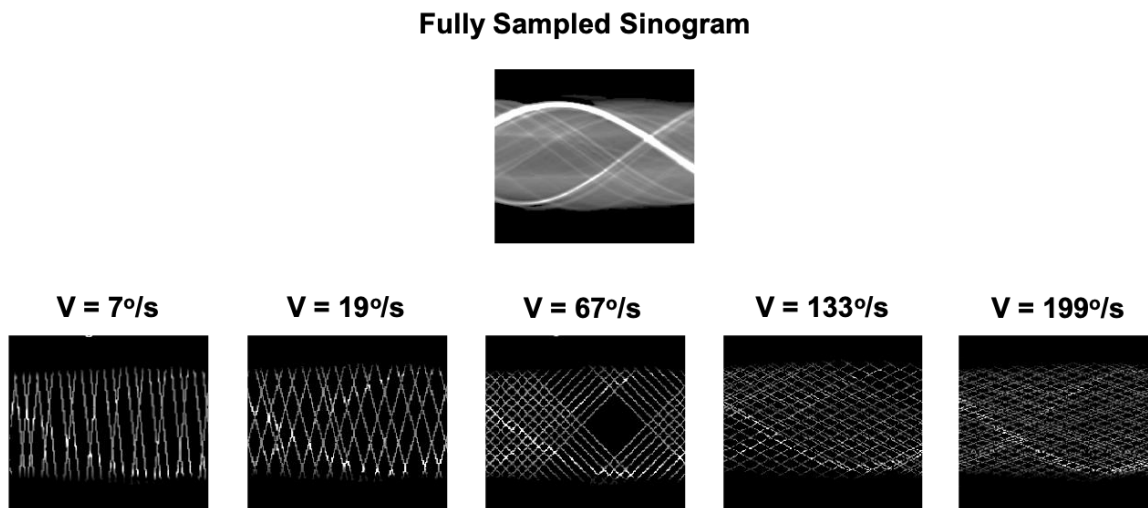


Figure 5.7 Influence of the sample rotation speed to the mask of visited pixels in the sinogram. For the same 31 CORT frame with the same pixel dwell time, the rotation speed of the sample drastically changed the sampling mask in the sinogram. Compared to the fully sampled sinogram, the faster the sample rotates, the more even the pixels visited can distribute through the image. However, notice that at $v = 67^\circ/\text{s}$, there is a sizable void with no pixels sampled. Due to the periodicity in equation 5.1, for some special cases, the high speed does not guarantee even distribution.

5.4.4 Modeling Inorganic Sample: Double-Walled Carbon-Nanotubes with Silver Nanoparticles

We tested the performance of the CORT sampling against conventional tilt series sampling on an inorganic sample: double-walled carbon-nanotube (CNT) with silver nanoparticles. The 3D structure of the sample was reconstructed using the full range rotation series available publicly¹⁹². The CORT sampling was generated numerically, 31 frames with 256 pixels by 256 pixels per

frame were employed with a pixel dwell time of 40 μ s, and a sample rotation speed of 130°/s. In sorting the CORT pixels, the integration span of 1° was used to generate undersampled sinograms. A 3D wavelet inpainting algorithm was performed to recover the missing information in the sinograms¹⁹¹. Projection series from 0° to 180° with 1° interval was created by reslicing the sinograms. We reconstructed the 3D structure from the inpainted CORT projection series by a Penalized Maximum Likelihood (PML) method in TomoPy⁹¹. The structural similarity matrix (SSIM) and pixel-to-pixel correlation were calculated between the 3D tomogram from CORT and the ground truth to quantify the accuracy of the CORT sampling.

We observed that the inpainted CORT sinogram (Figure 5.8 d) and projection image Figure 5.8 e) showed little difference compared to the fully sampled sinogram at the same sample location Figure 5.8 a) and projection image at the same tilt angle Figure 5.8 b). The reconstructed 2D-virtual slices from the fully sampled projection series (Figure 5.8 c) and CORT sparsely sampled series (Figure 5.8 f) were qualitatively identical. For the SSIM and pixel-to-pixel correlation, the quality of the tomography reconstructed by CORT is highly comparable to that of the tomography from conventionally fully sampled data. Notice that in this numerical experiment, CORT required only 31 frames, but the fully sampled data utilized 182 frames. In other words, CORT can reduce the electron dose by almost 6-folds without sacrificing the tomography reconstruction quality.

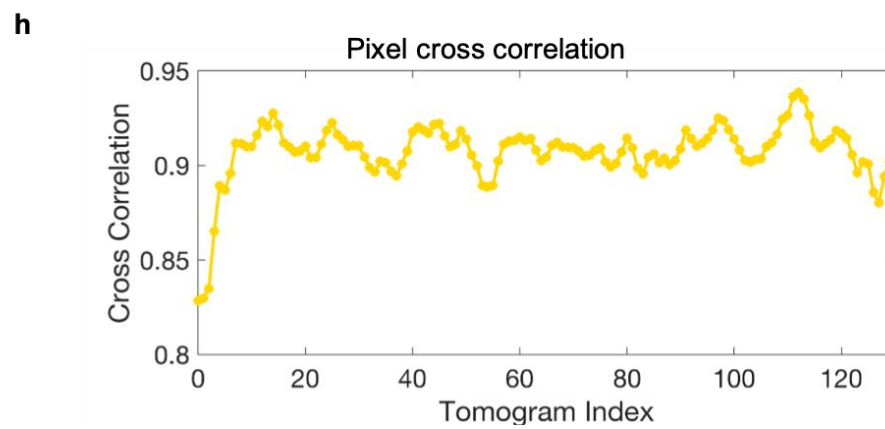
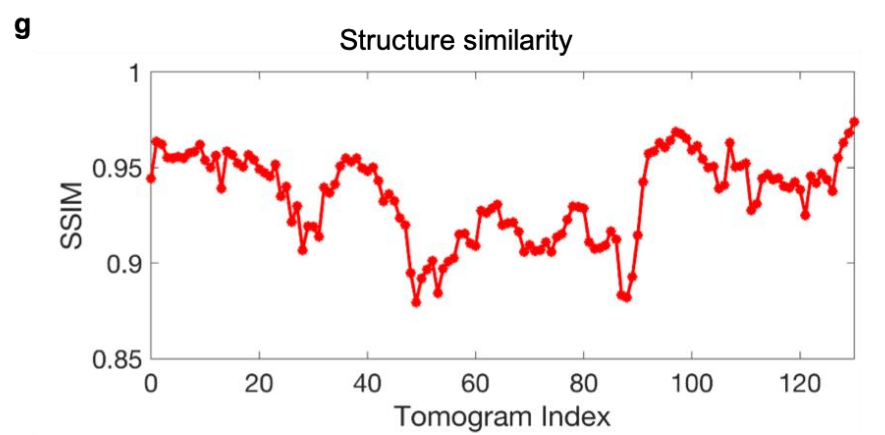
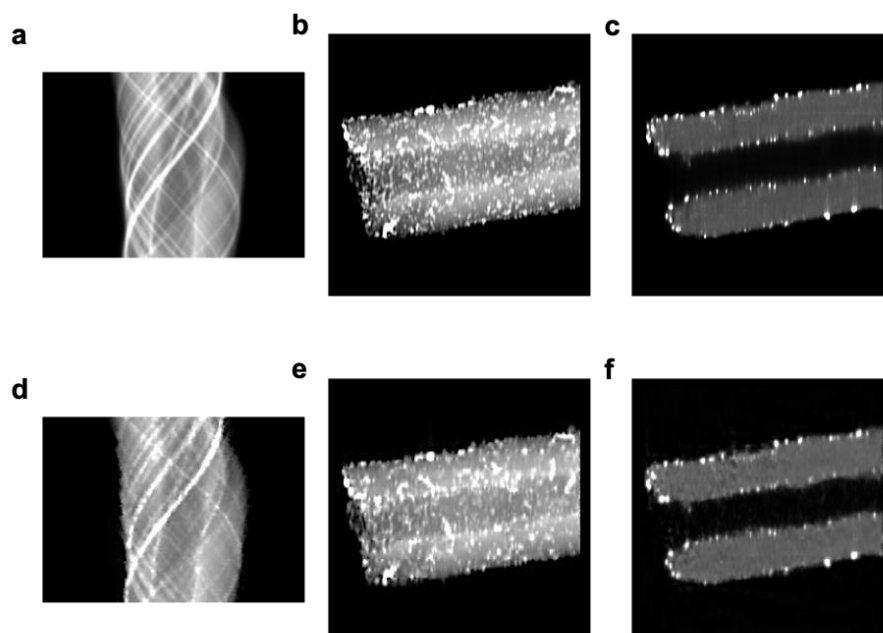


Figure 5.8 Performance of CORT on reconstructing a double-walled carbon nanotube with silver nanoparticles. (a) Fully sampled sinogram. (b) Fully-sample projection image. (c) One virtual 2D slice of the tomogram reconstructed from the fully sampled tilt series. (d) Inpainted sinogram from CORT data. (e) Resliced projection image from inpainted sinogram from CORT data. (d) One virtual 2D slice of the tomogram reconstructed from CORT data. (g) SSIM of the tomography reconstructed from fully-sample tilt series and CORT. (h) Pixel-to-pixel cross-correlation between the tomography reconstructed from fully-sample tilt series and CORT.

5.4.5 Modeling Organic Sample: Human Cheek Cell

Similar to the inorganic sample, we conducted a numerical experiment for an organic sample with beam sensitivity: a human cheek cell. The 3D structure of the cheek cell was reconstructed by PML algorithm in TomoPy⁹¹ from a dual-tilt series (Figure 5.9 a). The CORT sampling was generated under the same set of parameters as the inorganic sample reported in the previous section. Compared to the fully-sample projections, each of the CORT image frames contains multiple orientations for different parts of the sample. After sorting, the undersampled projection series consist of lines while the sinograms show checker-board pattern.

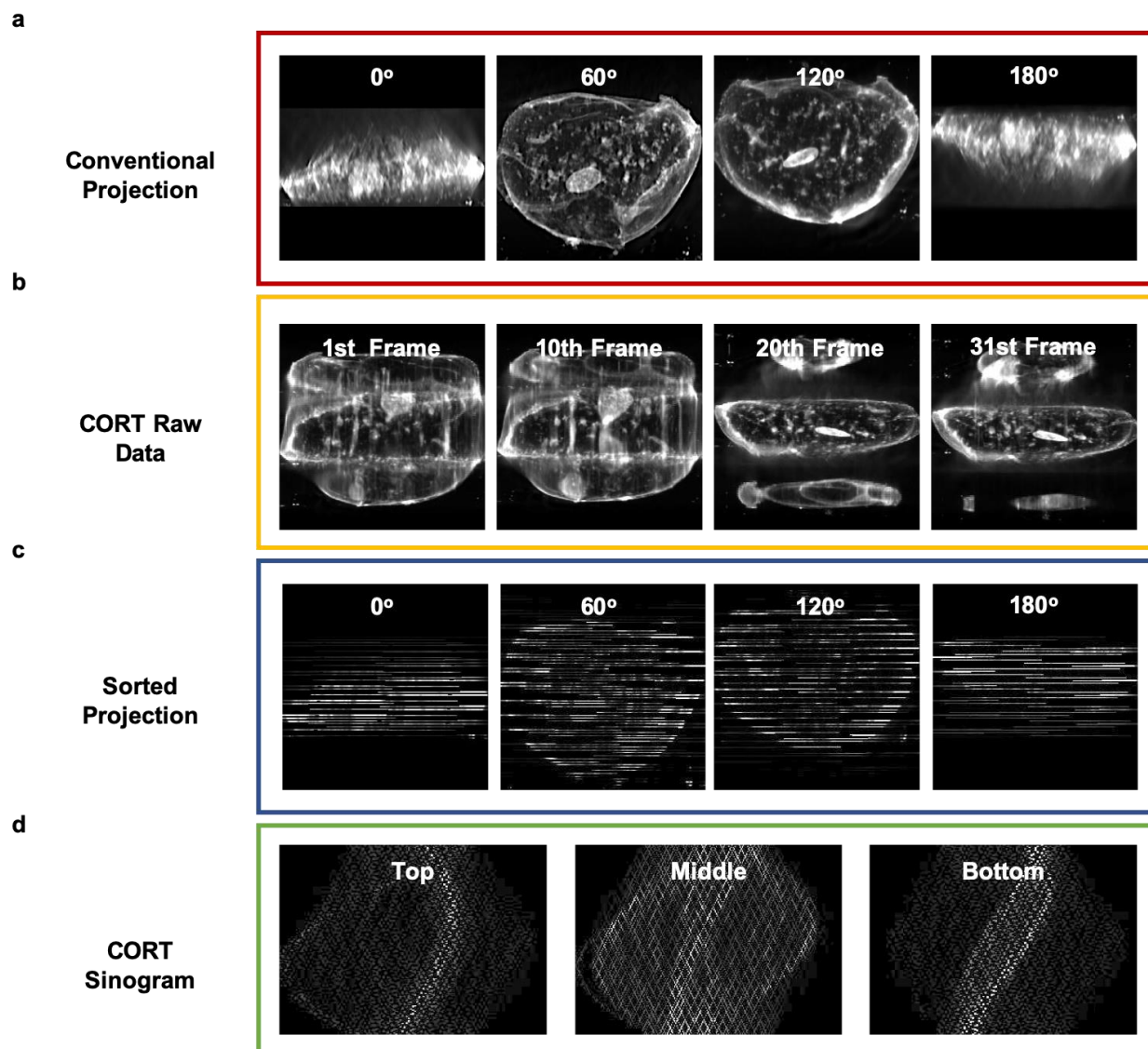


Figure 5.9 CORT data presentation as raw data, sorted projection, and sinogram for a human cheek cell. (a) The fully sampled projection images of a human cheek cell at different tilt angles (0° , 60° , 120° , 180°). (b) CORT raw data of 31 frames. In each frame, the pixels were oriented at different angles. (c) Sorted CORT data can form undersampled traditional

projection image at different tilt angles (0° , 60° , 120° , 180°). (d) The sorted projection can be rotated and resliced to create undersampled sinogram of the sample (top, middle, bottom).

To reconstruct tomography from the CORT data, the missing pixels in the sinograms were recovered by a 3D wavelet inpainting algorithm¹⁹¹. The projection series were generated by reslicing the inpainted sinograms. PLM algorithm was employed for tomography reconstruction, and the SSIM and the pixel-to-pixel cross-correlation were used to quantify the quality of the tomograms. Qualitatively, the inpainted sinograms, and the projection images were like the ground truth. The reconstructed tomograms showed all features, and we obtained a high pixel-to-pixel cross-correlation with the tomograms reconstructed from the fully-sample projection images. However, the SSIM between the CORT tomogram and conventional tomogram for a human cheek cell showed a lower value compared to the double-walled carbon nanotube sample. This might be caused by the inefficiency in the inpainting algorithm for a continuous feature in cheek cell. Smoothness constraints can be applied in the future to compensate and potentially improve the inpainting quality, and thus improve the overall SSIM.

Notice that CORT required only 31 frames to achieve a tomography reconstruction quality similar to the conventional method which required 182 frames. CORT effectively reduced the electron dose by 6-fold while maintaining the accuracy of the tomograms.

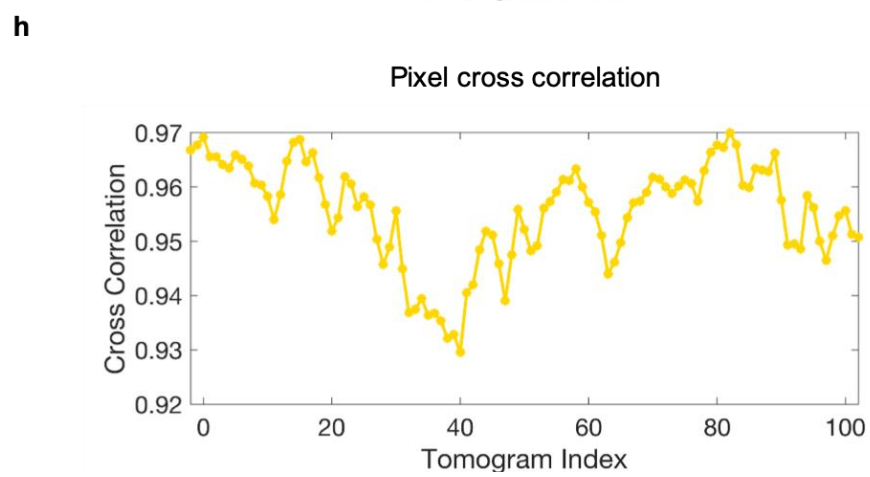
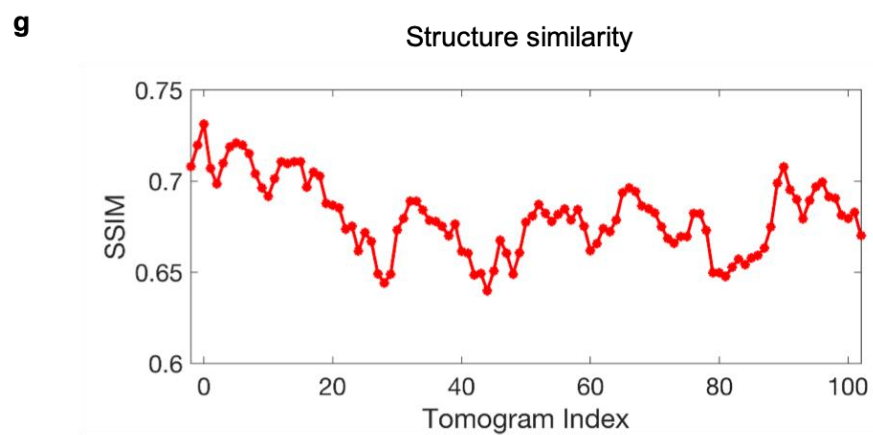
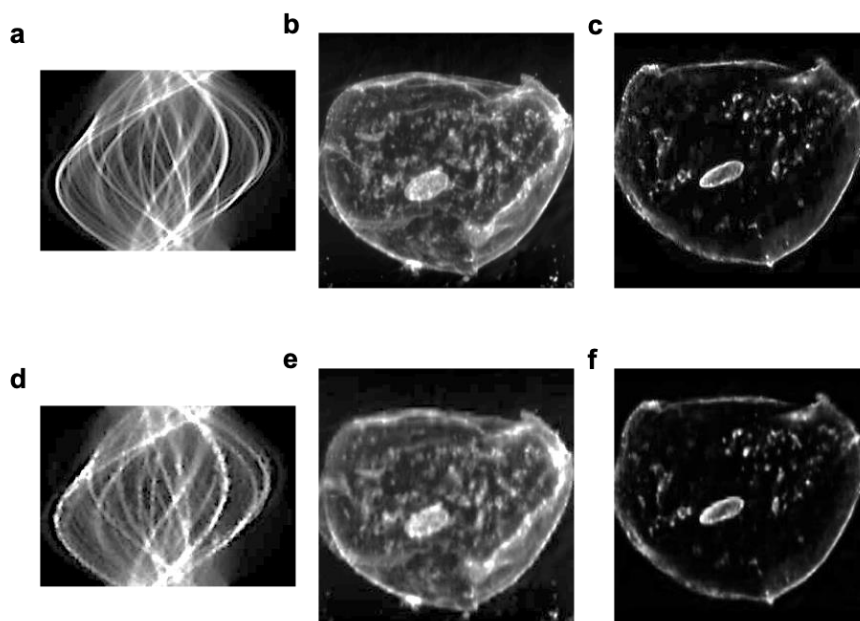


Figure 5.10 Performance of CORT on reconstructing a human cheek cell. (a) Fully sampled sinogram. (b) Fully-sample projection image. (c) One virtual 2D slice of the tomogram reconstructed from the fully sampled tilt series. (d) Inpainted sinogram from CORT data. (e) Resliced projection image from inpainted sinogram from CORT data. (d) One virtual 2D slice of the tomogram reconstructed from CORT data. (g) SSIM of the tomography reconstructed from fully-sample tilt series and CORT. (h) Pixel-to-pixel cross-correlation between the tomography reconstructed from fully-sample tilt series and CORT.

5.5 Discussion and Conclusions

The resolution of tomography reconstruction is determined by the number of projections measured from the same object. However, the illumination time is limited before the object is severely damaged by the beam, and thus restricted the total number of images can be taken at a given signal-to-noise ratio. In principle, a fully sampled image can be faithfully reconstructed using machine learning approach from a randomly under-sampled “corrupted” image. This approach can potentially reduce the total exposure time without harming the image quality. In practice, random under-sampling has not been implemented in high-energy scanning transmission electron microscope with sufficient speed to actually reduce beam damage due to the settlement time after altering the electron beam and is therefore not applicable to improve the resolution of electron tomography. We developed a novel data acquisition scheme, controlled rotation electron tomography (CORT) that sparsely sampled each projection image without interfering the electron beam or any hardware modifications. The mathematical foundations for random and un-adaptive under-sampling are demonstrated, and the performance evaluation of CORT was conducted by

numerical experiments on both inorganic and organic samples. We demonstrated that without sacrificing the tomography reconstruction quality, CORT has the potential to reduce the electron dose by 6-fold.

In contrast to previous methods that focused on in-painting as a post-processing technique for unexpected signal corruption, we have inverted the problem and created the necessary hardware and software inventions to sample information in purposefully under-sampled forms. Statistical machine learning algorithms are used to cast in-painting as a factor analysis problem, under which the discovery of latent features may enable simultaneous image recovery and pattern recognition. As CORT entails the direct application of image in-painting methods to the intentional capture of incomplete information and its subsequent restoral, an improved in-painting algorithm can significantly enhance the performance of this technique. To experimentally implement CORT, a mechanically stable goniometer is required and beyond the current technology limit for electron microscopy. However, CORT is a general sampling strategy that applies to all scanning transmission methods, including STEM and X-ray ptychography. In X-ray microscopy, as the resolution is on the order of dozens of nanometers, the requirement for the stage stability is not as strict, and customized high-speed spinning stages with drift correction are available. We anticipate that the first CORT experimental will be performed in the context of X-ray ptychography and drastically reduce the beam damage and reveal structures that have not been discovered before.

CHAPTER 6 FUTURE OUTLOOK AND CONCLUSIONS

6.1 Spectroscopic Intrinsic-Contrast Photon-Localization Optical Nanoscopy (SICLON)

For Label-free Nucleic Acids Imaging

The nanoarchitecture of chromatin underlies and regulates essentially all genetic machinery with a complex organization ranging from individual macromolecules that are a few nanometers in size (e.g. DNA), to macromolecular assemblies that may span tens of nanometers (e.g. nucleosome, chromatin fiber), to micron-scale structures forming topologically associating domains (TAD) and chromatin compartments. The major scientific challenge is to understand this heterogeneous chromatin structure at all length scales in non-perturbed states. Tremendous advances in techniques such as neutron scattering, small-angle x-ray scattering, electron microscopy, and super-resolution microscopy have greatly enriched our knowledge of chromatin nanostructure in the past decades. Super-resolution microscopy, specifically photon localization microscopy (PLM), is capable of resolving chromatin at sub-diffraction length scales (<200nm) with a micron-scale field of view. PLM has been employed to visualize the second-order (e.g., chromatin fiber) and the higher-order chromatin structure (e.g., TAD)¹⁹³. However, to visualize even finer details of chromatin such as a single nucleosome or DNA (length scales < 10 nm), using conventional PLM is challenging. The resolution of conventional PLM is limited by two key factors: labeling density and the number of photons from each emission (localization uncertainty). High label density is required in order to resolve structures according to the Nyquist criterion. Even with sufficiently high labeling density, the precision of fitting a point-spread function (PSF) during image reconstruction in PLM is dependent on the number of photons in each emission

event¹⁹⁴. Specifically, the spatial resolution of the PSF fit after reconstruction is proportional to $1/\sqrt{n}$, where n is the number of emitted photons. Together, these two factors have limited the resolution of conventional PLM techniques to approximately 20 nm. To improve the resolution of PLM, we describe spectroscopic intrinsic-contrast photon-localization optical nanoscopy (SICLON), a super-resolution microscopy technique to overcome both of these obstacles. Using SICLON, we demonstrate the ability to visualize DNA with sub-10 nm resolution.

To date, the methods for directly imaging chromatin generally require staining, such as the fluorescence dye in super-resolution microscopy (e.g., PALM/STORM)^{194,195} and combined fluorescence dye and heavy metal stain in electron microscopy (e.g., ChromEMT)³¹. However, the use of exogenous dyes has fundamental limitations: the uptake, diffusion, and localization of dyes depends non-linearly on the local environment and could render the chromatin image challenging to interpret, especially for the high label densities required to satisfy the Nyquist criterion for sub-10 nm resolution; and with spacing smaller than 30 nm, steric hindrance and epitope accessibility for most fluorophore probes becomes a significant issue as the labels are nearly the size of the molecules of interest. Additionally, the use of DNA intercalating dyes has the drawbacks of potentially distorting and even damaging DNA structure³². Due to these challenges, an alternative approach using label-free contrast for direct imaging has considerable advantages.

6.1.1 SICLON: Super-Resolution Microscopy for Label-Free Imaging at Sub-10 nm

Resolution

To tackle the labeling density issue and eliminate the potential artifacts introduced by labels, we utilized a newly discovered phenomenon: DNA can fluoresce under visible light, and the nucleotides of DNA itself used as the source of photon emission. While DNA had previously been considered “dark” in the visible spectral range, recently it was shown to exhibit photo-switchable autofluorescence when illuminated by visible light using ground-state depletion (GSD) with dark-state shelving and stochastic return¹⁹⁶. Dong *et al.* previously investigated the photochemical properties of DNA autofluorescence in detail¹⁹⁷. By leveraging GSD, direct nanoscopic imaging of nucleic acids using their intrinsic fluorescence for contrast has been demonstrated. Under visible light illumination, unmodified DNA has the capacity to stochastically emit photons allowing for their use in photon localization microscopy. While nucleic acids have weak absorption within the visible range, they have a remarkably high quantum efficiency, a long-lived dark state, and comparably high photon emission counts^{196,198}. Furthermore, as the base unit of chromatin is nucleic acids, their use for PLM completely bypasses the labeling density limits presented by exogenous approaches, and the non-linear effects of local macromolecular density would have on molecular mobility and binding affinities. Using the intrinsic stochastic fluorescence of nuclear acids, the capacity to image chromatin without exogenous fluorophores with ~20 nm resolution has been demonstrated.

As the fundamental building block of chromatin, the nucleosome is a disk with 11 nm in diameter and 6 nm in thickness, and linker DNA to connect the nucleosomes is merely 2 nm wide, to fully characterize the chromatin requires even higher resolution. To meet this end, Li *et al.*

reported a novel PLM reconstruction algorithm to push the resolution limit to sub-10 nm regime for nucleic acids¹⁹⁹. The Spectroscopic Intrinsic-Contrast Photon-Localization Optical Nanoscopy (SICLON) is able to measure the spatial information and spectra of nucleotides during fluorescing simultaneously and utilized the spectral information to differentiate nucleotides that are in the proximity of each other to enhance resolution. Li et al. reported an unprecedented image resolution for optical microscopy at 6.2 nm for a linearly stretched DNA fiber. To validate the resolution, an AFM measurement of the width of a typical linearly stretched DNA was used as the gold standard (Figure 6.1).

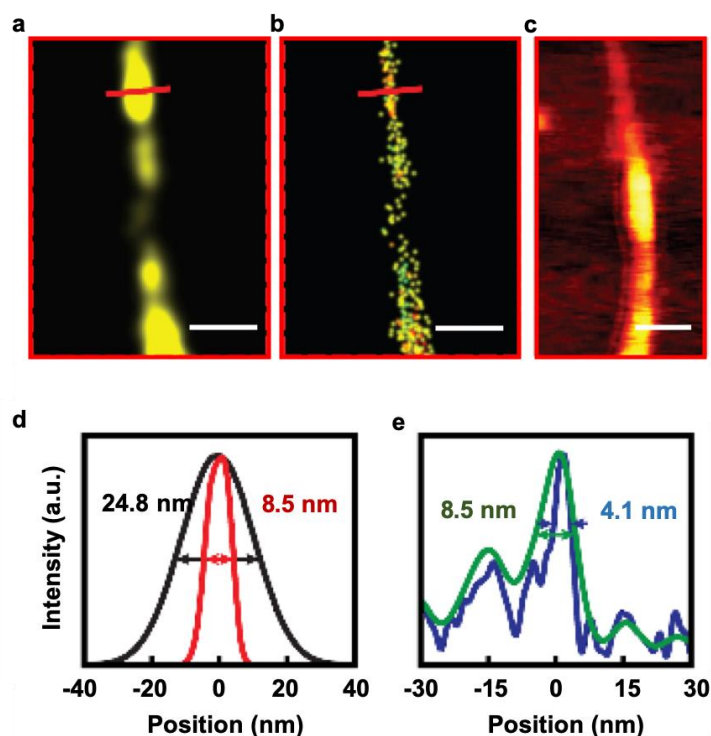


Figure 6.1 Validation of SICLON resolution by AFM. (a) STORM reconstruction of DNA fiber using 532 nm illumination. (b) SICLON reconstruction of DNA fiber after applying the SR algorithm. (c) AFM measurement of a separate single DNA fiber. (d) Comparison of

resolution between traditional PLM and SICLON with SR shows a 4X resolution enhancement. (e) AFM reveals that the ground truth width of the fiber is estimated to be 4.1 nm.

6.1.2 Quantification of Chromatin Structure from SICLON Images

Beyond DNA fibers, the SICLON is also capable of imaging condensed chromosomes²¹⁵, isolated nuclei, and the whole cell. To quantify the chromatin structure resolved by SICLON, herein, we introduce a novel algorithm to calculate the correlation dimension. In general, the chromatin can be modeled as a fractal structure, and the critical physical quantify is the mass-scaling or fractal dimension. To calculate the fractal dimension, the total mass distribution is needed. Correlation dimension, D_c , is utilized in quantifying the sample structure through a set of points instead of the total mass. For instance, an electron microscopy image of the clustering of proteins in biological membranes gives information on point distributions but not the mass content. The SICLON images are essentially the spatial distribution of nucleotides instead of the mass distribution of DNA, so compared to the conventional fractal dimension, the correlation dimension is more convenient to estimate. The correlation dimension is closely related to the mass fractal dimension²⁰⁰.

To calculate the correlation dimension D_c , the number of pairs of points, $C(r)$, that lie within a radius, r , of each other is counted. The quantify scales as:

$$C(r) \sim r^{D_c} \quad (6.1)$$

The correlation dimension is determined from the slope of a log-log plot of $C(r)$ versus r (Figure 6.2).

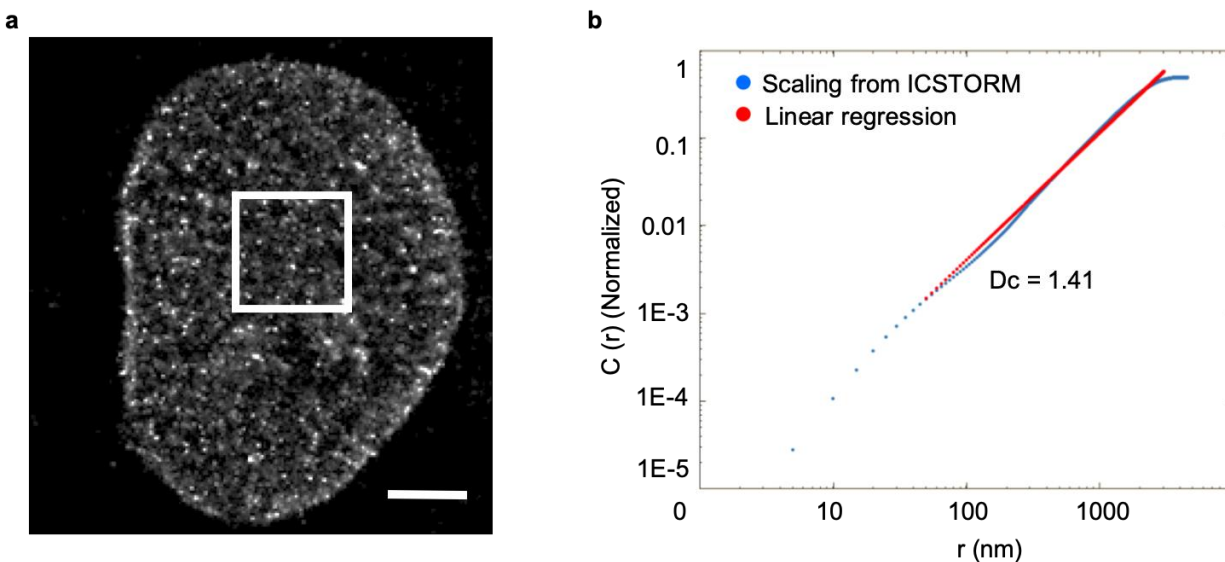


Figure 6.2 Quantifying chromatin structure from SICLON images by correlation dimension D_c . (a) SICLON image of chromatin of an isolated nucleus. Scale bar: $2 \mu\text{m}$. The number of pairs of points with a mutual distance smaller than r as a function of r . The log-log plot showed a linear region, indicating a fractal internal structure. The correlation dimension was 1.41 from the slope of the linear regression.

6.1.3 Chromatin Alterations Detection in Wild Type and Chemo-Treated Ovarian Cancer Cell Lines

Although the genetic information is coded in a linear fashion, it is the 3D genome organization that regulates the gene transcription. It has been hypothesized that the cancer cell

mutation that can survive chemotherapy treatment benefits from increased heterogeneity in the genomic landscape to fully explore different sequences⁷. Based on this hypothesis, we treated the wildtype ovarian cancer cell line A2780 with a conventional chemotherapy drug paclitaxel (Pac). We performed the SICLON experiments on the control and treated cells to obtain chromatin distribution and calculated the correlation dimension accordingly. To cross-validate the difference in chromatin packing detected by SICLON, the same cells were imaged with Partial Wave Spectroscopy Microscopy (PWS). PWS is a nanoscale spectroscopic technique that is sensitive to the chromatin structure between 20 nm to 200 nm. Importantly, the PWS signal (Σ) is directly proportional to the mass-fractal dimension, in other words, proportional to the heterogeneity in the genomic landscape. We observed that after chemo-treatment, the survival cells showed a higher D_c and a higher PWS signal, indicating increased chromatin heterogeneity.

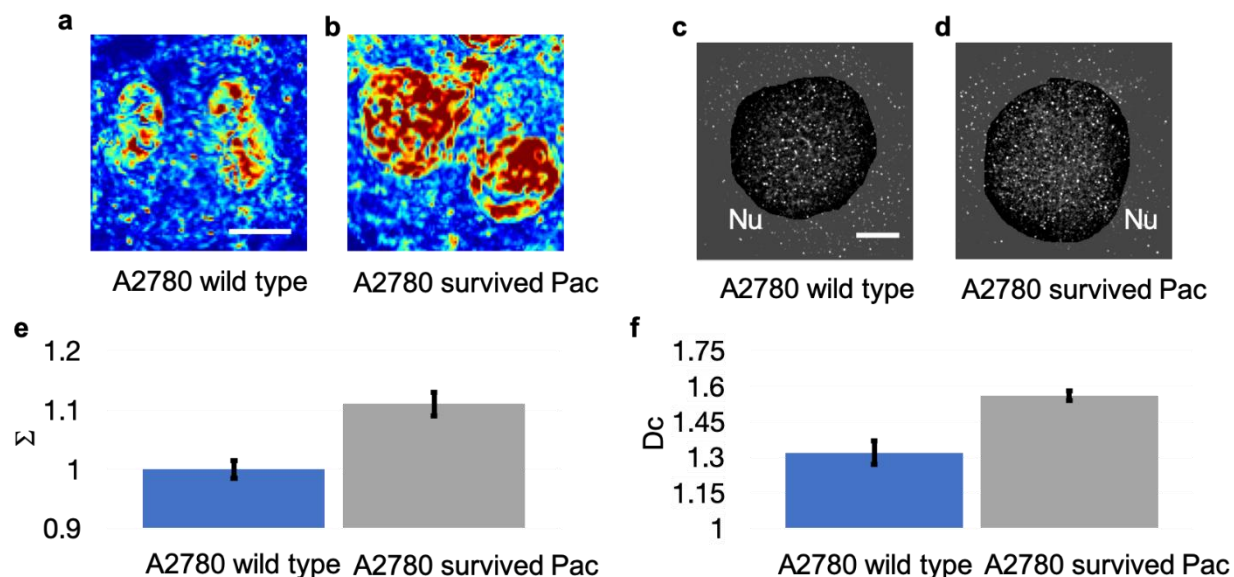


Figure 6.3 Quantifying chromatin alterations in wildtype and chemo-resistant ovarian cancer cell lines (A2780). (a) and (b), PWS measurement of the A2780 wildtype and the strand with chemo-resistance mutation. Scale bar: 15 μm . (c) and (d), SICLON image of the A780 wildtype and chemo-resistant mutation. Scale bar: 10 μm . The cytoplasm was shaded with a gray mask, and the nuclei were labeled. (e) The PWS measurement and (d) Correlation dimension from SICLON for the chromatin in A2780 wildtype and chemo-resistant mutation. In both modules, the chromatin heterogeneity of the chemo-resistant mutation was significantly more considerable than that of the wildtype.

6.1.4 Discussions and Conclusions

SICLON is capable of imaging nucleic acids at the resolution down to sub-10 nm and sufficient to adequately image the organizational structure of without the need for extrinsic dyes.

Using the intrinsic contrast produced by the stochastic emission of nucleic acids and spectral regression, we validated using AFM that for imaging isolated nucleotides and single-stranded DNA, SICLON can achieve a lateral resolution of 6.2 nm.

To characterize the chromatin structure, we employed correlation dimension to estimate the spatial distribution of nucleotides (emitters) in the SICLON images. We observed that the number of emitters $C(r)$ within a mutual distance r were scaled by a power-law with r , and the scaling exponent is defined as the correlation dimension. The power-law scaling also indicated that the chromatin adopted a fractal structure.

We quantified the chromatin alterations in wild-type and chemo-resistant ovarian cancer cell line A2780 using SICLON and PWS. For both modalities, we observed increasing chromatin heterogeneity in the chemo-resistant type. We believe the potential of SICLON to fully map the structure of chromatin in-vitro will significantly expand our understanding of how chromatin topology influences fundamentally all genetic machinery.

6.2 Multi-Technique-Multi-Scale (MTMS) Imaging Platform: Bridging the physical and genomic landscape in chromatin

How does chromatin, a highly disordered, flexible, and time-evolving macromolecular assembly, emerge from a one-dimensional (1D) polymer structure while predictably regulating molecular functions such as gene transcription and DNA replication? This question remains central to the understanding of how the genome fulfills its role as a heritable structure that is both an information assembly and a physical ensemble. To date, chromatin conformation capture

techniques (3C, 4C, 5C, and Hi-C) have produced a wealth of knowledge about the formation of long-range contacts that result from the transition from a 1D polymer filling 3D space. In particular, it has been established that long-range contacts (>50kbp) are maintained across cellular lineages, strongly associate with transcriptional activity, and are the result of the coordination of numerous molecular regulators. Despite this evidence for a well-regulated integration between the 1D and 3D hierarchy of chromatin above individual nucleosomes, the inherent limitation of these methods is that they cannot spatially resolve the observed structures or be applied to the study of live cells over time.

6.2.1 Significance of Developing a Microscopy-Based Multi-Technique Multi-Scale Imaging Platform for Genomics Analysis

With respect to chromatin packing in live cells, evidence has shown that the regulation of gene transcription occurs through the following pathways: (1) at the genetic level through interactions between transcription factors and sequence binding motifs (~2 nm); (2) at the nucleosomal level through alterations in local DNA accessibility (~10 nm); and (3) at the level of topologically associated domains (TADs) through gene compartmentalization (~100 nm)¹⁴¹. As the transcriptional regulation happens at all levels dynamically, it is crucial to investigate the 3D and 4D chromatin organization over complementary length scales and times.

Recently, microscopy-based techniques have been regaining popularity in order to address the challenges imposed by the limitations of current C-based techniques and providing insights to some long-standing questions such as how the genome changes during cell differentiation at single

cell level²⁰¹. Advances in the development of custom staining methods in combination with novel high-resolution imaging approaches have enabled direct visualization of fine-scale structures of the genome with unprecedented labeling specificity and spatial resolution²⁰². In particular, the ChromEMT method, which utilizes a DNA specific labeling protocol (“Click-EM”) and TEM tomography, has achieved a 1.6 nm voxel resolution and resolved individual nucleosomes and linker DNAs in the interphase and mitotic nuclei³². The findings from the ChromEMT experiments suggest that the chromatin polymer is disordered chain packed together at different densities throughout the nucleus. In other studies, the combination of custom oligonucleotide arrays such as Oligopaint and novel super-resolution microscopy approaches such as STORM and PALM have enabled the direct visualization of the chromatin fiber and different groups of nuclear bodies at single cell level, and has been further employed to reveal the power-law relationship between the chromatin physical volume and genomic length at different epigenetic states in active, inactive, and Polycomb-repressed domains for *Drosophila melanogaster*⁴.

Furthermore, early success has been reported to generate “Hi-C” like contact probability maps from STORM images for single cell nucleus¹⁵⁷. In the pursuit of live-cell imaging, Partial Wave Spectroscopy (PWS) Microscopy stands out. Due to its ability to measure the nanoscopic chromatin packing density with sensitivity to chromatin organization between 20 and 350 nm in live cells, PWS has been employed to monitor the chromatin alterations during chemotherapy, UV radiation, ionic environment changes, and cell differentiation²⁰³.

6.2.2 Formulation of the Microscopy-Based Multi-Technique Multi-Scale (MTMS)

Imaging Platform

Despite the invaluable information about the dynamics of individual chromosome domains or generic chromatin provided by these advanced microscopy techniques, every single microscopy-based approach is limited to some resolution, a relatively small field of view, or a small number of genetic loci compared to any C-based techniques. The challenges are to improve the coverage and information obtained from each of these methods, which are all less than complete. To meet this end, we have developed a complete nanoimaging platform to investigate chromatin organization at all length scales from individual cells at high throughput. Combining ChromEM, STORM, and PWS, the streamlined multi-technique nanoimaging platform is capable of imaging the 3D chromatin structure at 2.9 nm voxel resolution, identifying various epigenetic states, and tracking live cells over a prolonged period. As each imaging modality investigates different aspects of the chromatin architecture (ChromEM: DNA density, STORM: epigenetic states, PWS: chromatin transcriptional heterogeneity), we employed mass-scaling of chromatin to unify the multi-omic measurements from all three approaches.

Independent of the exact configuration of supranucleosomal folding, the 3D chromatin packing can be mathematically described by the mass scaling relation and the spatial autocorrelation function (ACF). The mass scaling relation $M(r)$ is the mass of chromatin (M) contained within a sphere of radius r , and it dictates the relationship between the physical size and the genomic size of the chromatin. The ACF is the quantitative relationship between the fundamental structural unit (chromatin fiber) and larger structures such as TADs like nanodomains and chromosomal territories. Although the exact nature of 3D chromatin architecture is a topic of

active debate, most recent evidence with ultrahigh resolution such as ChromSTEM (~3nm) showed a power-law mass scaling $M \propto r^{D_{MS}}$ up to the Mbp range, suggesting chromatin is a mass fractal with a fractal dimension (scaling exponent) $D_{MS} < 3$. The power law mass scaling (D_{MS}) is commonly found in a variety of polymer systems and is associated with the scaling estimated from ACF (D_{ACF}) by $ACF \propto \frac{dM(r)}{dV} \propto r^{D_{ACF}-3}$, where V is the volume. Importantly, the fractal dimension (D_{MS} and D_{ACF}) can be quantified by multiple *ex vivo* molecular technique such as small angle neutron scattering and particularly the 3C-based techniques (3C, 4C, 5C, Hi-C), as well as *in vitro* by nanoscale-sensitive imaging techniques such as ChromEM, STORM, and PWS. Through the fractal dimension analysis, we were able to incorporate ChromEM, STORM, and PWS under one consolidated framework to quantify the chromatin organization, and to compare the measurements from the multi-technique platform to the findings from Hi-C directly.

6.2.3 The workflow of the Microscopy-Based Multi-Technique Multi-Scale (MTMS)

Imaging Platform

Although the genetic and histone codes can be addressed by molecular assays, decoding chromatin packing can only be achieved through “convergent science” that bridges physics-based modeling of transcriptional reactions, nano-imaging, and molecular biology. We have developed a multi-technique platform (Figure 6.4) including state-of-the-art nanoimaging capabilities which spatiotemporally interrogates chromatin packing from individual DNA strands (ChromEMT with STEM HAADF adaptation) to chromatin compartment visualization (ChromEM with thin section TEM imaging) to single molecular-localization nanoscopy (STORM) to chromatin packing at 20-

300 nm length scales in hundreds of live cells in real-time (PWS), and a computational platform, which models gene expression in the realistic chromatin nano-environment.

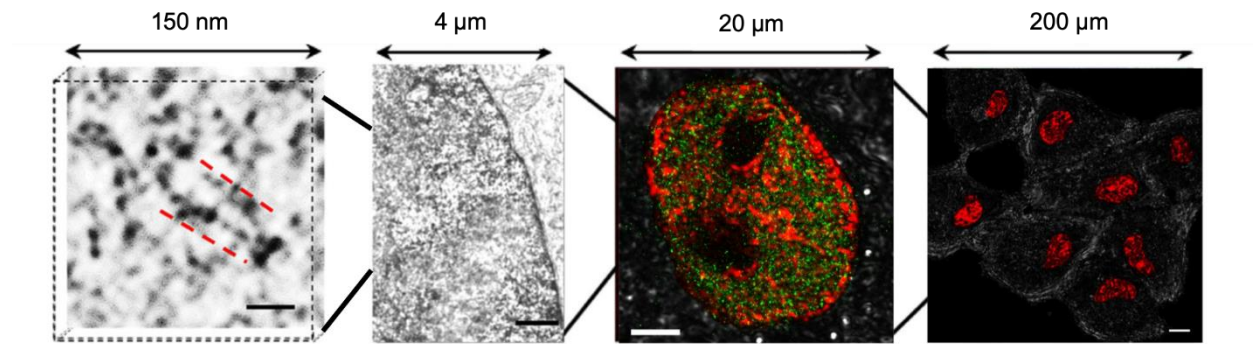


Figure 6.4 Examples of the multi-technique nanoimaging and computational transcriptomics platform. The multi-technique platform consists of three parts: nanoimaging to directly visualize chromatin packing at all length scales (5 nm to 200 μm); multi-scale computational analysis to investigate the underlying physics behind chromatin structure; Hi-C characterization to provide big data for high-statistical power analysis across the entire genome over different cells lines and conditions. Top panel, from left to right: 1. Ultra-high-resolution scanning transmission electron tomography at 3 nm resolution for 3D chromatin structure in mammalian cells. Scale bar: 30 nm. 2. High throughput TEM imaging of 50 nm slice of BJ cell nucleus. Scale bar: 1 μm . 3. PWS (red) and super-resolution STORM (green) co-registered imaging of chromatin scaling and Pol II. Scale bar: 3 μm . 4. Label-free PWS image of live HeLa cells. Pseudo-color: DPWS with sensitivity from 20 to 350 nm. Scale bar: 20 μm .

6.2.4 Materials and Methods

Cell culture

A549 cells were cultured in Dulbecco's Modified Eagle Medium (ThermoFisher Scientific, Waltham, MA, #11965092). BJ cells were cultured in Minimum Essential Media (ThermoFisher Scientific, Waltham, MA, #11095080). All culture media was supplemented with 10% FBS (ThermoFisher Scientific, Waltham, MA, no. 16000044) and 100 µg/mL Penicillin-Streptomycin (ThermoFisher Scientific, Waltham, MA, # 15140122). All cells were maintained and imaged at physiological conditions (5% CO₂ and 37 °C) for the duration of the experiment. All cell lines were tested for mycoplasma contamination with Hoechst 33342 within the past year. Experiments were performed on cells from passage 5–20.

ChromSTEM Sample Prep

For EM experiment, all the cells were prepared by the ChromEM staining protocol (Appendix B). Hank's balanced salt solution without calcium and magnesium was used to remove the medium in the cell culture. Two-step fixation using EM grade 2.5% glutaraldehyde and 2% paraformaldehyde in 0.1M sodium cacodylate buffer (EMS) was performed: 1. Fixation at room temperature for 10 minutes. 2. Continuous fixation on ice for 1 hour with a fresh fixative. The cells were kept cold from this step either on ice or on a cold stage, and the solution was chilled before use. After fixation, the cells were thoroughly rinsed by 0.1M sodium cacodylate buffer, blocked with potassium cyanide (Sigma Aldrich) blocking buffer for 15 minutes, and stained with DRAQ5TM (Thermo Fisher) with 0.1% saponin (Sigma Aldrich) for 10 minutes. The excessive dye was

washed away using blocking buffer. The cells were bathed in 3-3' diaminobenzidine tetrahydrochloride (DAB) solution (Sigma Aldrich) during photo-bleaching.

A Nikon (Eclipse, Nikon) with Cy5 filter sets were employed for photo-bleaching while the cells were kept cold on a custom-made wet chamber with humidity and temperature control. 15 W Xenon lamp and the red filter was used as the source of epi-illumination. With 100x objective, each spot was photo-bleached for 7 min, and fresh DAB was added to the dish for every 30 minutes. After photo-bleaching, the excessive DAB was washed away by 0.1 M sodium cacodylate buffer, and the cells were stained with reduced osmium (2% osmium tetroxide and 1.5% potassium ferrocyanide, EMS) for 30 minutes on ice to further enhance contrast. Following heavy metal staining, the cells were rinsed by DI, serial ethanol dehydrated, and brought back to room temperature in 100% ethanol. The standard procedure of infiltration and embedding using Durcupan resin (EMS) was performed. The flat embedded cells were cured at 60°C for 48 hours.

Two kinds of sections were made using an ultramicrotome (UC7, Leica). For the tomography, 100 nm thick resin sections were cut and deposited onto a copper slot grid with carbon/formvar film (EMS). For investigating the chromatin structure difference with and without dexamethasone treatment, 50 nm, thin sections were made and deposited onto copper 200 mesh grid with carbon/formvar film (EMS). The grids were plasma-cleaned by a plasma cleaner (Easi-Glow, TED PELLA) prior to use. No post staining was performed, but 10 nm colloidal gold nanoparticles were added to the 100 nm thick samples on both sides as fiducial markers for the tomography.

ChromEM imaging and tomography reconstruction

A 200 kV STEM (HD2300, HITACHI) was employed for tomography data collection. High angle annular dark field (HAADF) imaging contrast was used in the tilt series. In order to reduce the missing wedge, tilting -60° to 60° on two perpendicular axes was performed manually, with 2° step size. The pixel dwell time was kept small ($\sim 5 \mu\text{s}$) to prevent severe beam damage during imaging. For the thin sections, a TEM (HT7700, HITACHI) was operated at 80 kV in the bright field to capture high contrast chromatin data. For statistical analysis, 8 cells were imaged for the control group, and 12 cells for the dexamethasone-treated group.

For the STEM HAADF tilt series, the images were aligned using IMOD with fiducial markers^{24,221}. 40 iterations of a penalized maximum likelihood (PML) algorithm with non-negativity constraints in TomoPy²²¹ was employed for tomography reconstruction for each axis. The two reconstructed tomogram sets were re-combined in IMOD to further suppress the artifacts introduced by the missing cone. A nominal voxel size of 2.9 nm was used in the tomography to resolve individual nucleosomes.

3D Chromatin packing analysis using ChromSTEM tomography

Spatial correlation analysis

The chromatin density fluctuations were calculated from the grayscale 2D virtual slices of the chromatin. Firstly, the mean gray-scale value was subtracted from each image, and the resulting image is the chromatin density fluctuation (ρ_Δ). Secondly, the two-dimensional autocorrelation function (ACF) was calculated using the Wiener- Khinchine relation as:

$$B_\rho(x, y) = F^{-1}\{|F(\rho_\Delta(x, y))|^2\}, \quad (6.2)$$

where F^{-1} and F is the inverse Fourier, and the Fourier transforms, and the ρ_{Δ} is the fluctuating part of the chromatin density. To minimize the noise, a rotational average of $B_{\rho}(x, y)$ was taken to obtain the final form of the ACF $B_{\rho}(r)$, representing the correlation of chromatin density as a function of spatial separation r . Notice that mathematically, a fractal structure can be characterized by a power-law ACF, $B_{\rho}(r) \sim r^{D_{ACF}-3}$, with D being the fractal dimension. For the chromatin reconstructed by ChromSTEM, the mean ACF $B_{\rho}(r)$ was averaged over the ACFs of each virtual 2D slices and plotted in log-log scale. Linear regions were identified, and linear regression was performed for each region to obtain the slope. The average fractal dimension for the virtual 2D slices D_{ACF} was calculated by $3 + p$ for each region.

Chromatin fractal dimension comparison for A549 cells with dexamethasone treatment

TEM images of 50 nm thin sections were used in the analysis of chromatin packing alterations induced by the dexamethasone treatment for 32 hours. Unlike STEM HAADF imaging mode, the TEM bright field contrast attenuates following Beer's law,

$$I(x, y) = I_0 e^{-\sigma \rho(x, y) t}, \quad (6.3)$$

where $I(x, y)$ is the TEM image intensity distribution, I_0 is the incident beam intensity, σ is the absorption coefficient, $\rho(x, y)$ is the density distribution, and t is the section thickness. In our experiment, I_0 , σ , t were controlled to be constant for all images, only the chromatin density $\rho(x, y)$ contributes to the final image intensity $I(x, y)$. To obtain the density fluctuation, $\rho_{\Delta}(x, y)$, we took the negative logarithm of all the TEM images directly and subtracted the mean value. At the same time, the incident beam intensity I_0 is canceled out. Each nucleus was carefully

segmented manually in FIJI and the fractal dimension D_{ACF} was calculated through the ACF analysis within the nucleus. The average fractal dimension for the control group (n = 8) and treated group (n = 10) was compared.

6.2.5 Chromatin Forms Spatially Separable Packing Domains with Fractal Internal Structures

To investigate chromatin packing, direct imaging ChromSTEM HAADF tomography with 2.9 nm voxel resolution was performed. From the ChromSTEM HAADF tomography reconstruction, the classical “beads on the string” model with individual nucleosomes and linker DNAs were clearly resolved (Figure 6.5 a-c). Utilizing the HAADF imaging mode with quantitative contrast that is proportional to the mass-thickness of the chromatin, the average ACF of chromatin was calculated directly from all 33 virtual 2D slices to characterize the packing scaling. In (Figure 6.5 d). The ACF of chromatin was plotted against spatial separation r in log-log scale to visualize the power-law relation between the two. Interestingly, three regions with significantly different power-law scaling D_{ACF} were observed: 1. the nucleosomal region from 0 nm to 11.6 nm; 2. the first fractal region from 11.6 nm to 59 nm; 3. the second fractal region from 58 nm to 145 nm. Importantly, the power-law scaling observed in multiple length scales in the chromatin ACF analysis provides direct experimental evidence to model chromatin as a mass fractal with fractal dimension D_{MS} .

The chromatin volume concentration (CVC) was also calculated from the ChromSTEM data, and we observed spatially separable packing domains with diameters of around 100 nm

(Figure 6.5 e). We calculated the fractal dimension (D_{MS}) for each domain and identified the fractal domain boundary. We noticed that one fractal domains could contain more than one CVC domains (Figure 6.5 f), and the CVC has a curvilinear relationship with D_{MS} for each domain (Figure 6.5 g).

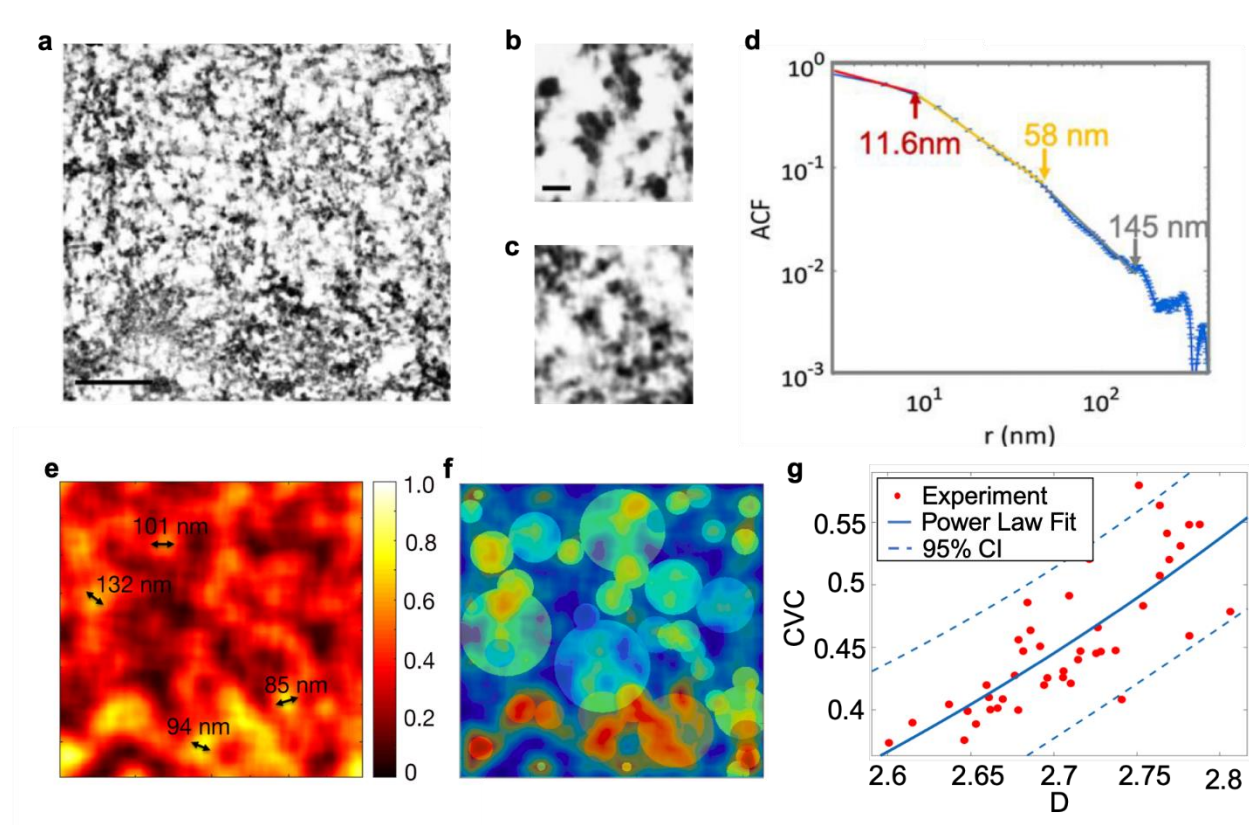


Figure 6.5 Chromatin packing exhibits mass fractal structures in multiple length scales. (a) A pseudo-2D cross-section (2.9 nm in thickness) of A549 cell nucleus chromatin after 3D STEM HAADF tomography reconstruction (contrast inverted). Scale bar: 200 nm. (b-c) The STEM tomography has a nominal resolution of 2.9 nm and is capable of resolving individual nucleosomes and linker DNAs in the pseudo-2D cross sections. Scale bar: 20 nm. (d) Average 2D ACF of 33 chromatin cross sections plotted in log-log scale. Three linear regions

were identified on the curve belonging to different topologies in chromatin packing: nucleosome region (0 to 11.6 nm), pure mass fractal region (11.6 nm to 58 nm), chromatin interpenetrating region (58 nm to 145 nm). The ACF analysis provided experimental evidence that chromatin is a mass fractal structure in certain length scales. (e) The moving average chromatin volume concentration (CVC) map showed spatially separated packing domains with a diameter of around 100 nm. (f) The fractal map overlaid with CVC map. Each fractal domain can contain multiple CVC domains. (g) The mass fractal dimension D_{MS} and CVC showed a positive correlation.

6.2.6 Characterizing Dexamethasone-Induced Time-Sensitive Chromatin Packing

Alterations

From molecular dynamics simulation, the CVC is related to the crowder volume (Φ), which influences the transcription rate by controlling the macromolecular diffusion. As shown in the previous section, the chromatin fractal dimension and CVC are strongly positively correlated; therefore, the chromatin fractal dimension, in principle, should also play an essential role in regulating gene transcription. On the other hand, the physical configuration of chromatin can both influence and be influenced by the genome connectivity, and this configuration is again quantified by the fractal dimension. We hypothesized that the chromatin structure quantified by fractal dimension could be indicative of the state of gene transcription. We employed dexamethasone (DXM), a common chemotherapy drug, to induce transcription alterations in human lung carcinoma epithelial cell line (A549) and human fibroblast cell line (BJ) and measured the difference in chromatin fractal dimensions using ChromSTEM and PWS respectively.

As shown in Figure 6.6, the MTMS platform was employed to capture the chromatin alterations in all length scales induced by DXM treatment in A549 cells. In particular, we utilized the ChromEM technique to directly visualize the fine chromatin structure with 5 nm spatial resolution on a 50 nm thick resin section (Figure 6.6 a-b left panel), the PWS to examine the mid-range (20 nm to 200 nm) chromatin packing across hundreds of cells per condition (Figure 6.6 a-b middle panel), and the Hi-C analysis to reveal the chromatin topological domains with size in between kb-Mb (20 nm to 350 nm) (Figure 6.6 a-b right panel). Qualitatively, compared to the control group, the cell nuclei in the DXM treatment group showed less variation in the image contrast in the ChromEM micrographs, lower image intensity in the PWS maps, and more homogeneous distribution in the Hi-C heat map. The trend we observed in all three techniques indicated a decrease in the scaling of chromatin packing in A549 cells after DXM treatment. We calculated all three different measures of the chromatin packing scaling: the ACF analysis was performed to obtain D_{ACF} in between 20 nm to 50 nm (Figure 6.6 c), D_{PWS} was measured in live cells, and the contact probability analysis was conducted to calculate (Figure 6.6 d) in the range of 60 kb to 0.3 Mb. As shown in Figure 6.6 e-g, in the DXM treated group, we observed a 3.8% decrease in D_{ACF} , a 3% decrease in D_{PWS} , and a 5% increase in s . Notice that s is inversely related to the chromatin density mass scaling D_{MS} , an increment in s indeed indicates a decrease in D_{MS} . In other words, all three techniques agree with each other and confirmed that there is a significant reduction in the chromatin packing scaling in A549 cells after the DXM treatment. The ChromEM has the highest resolution and is able to directly visualize chromatin structure, but it's a low yield method ($n \sim 10$) comparing to the PWS ($n \sim 100$) and the Hi-C ($n \sim \text{millions}$). The power of the the

multi-technique platform is that the individual tools cross-validate each other, and thus capable of rendering conclusions with both high resolution and high statistical power.

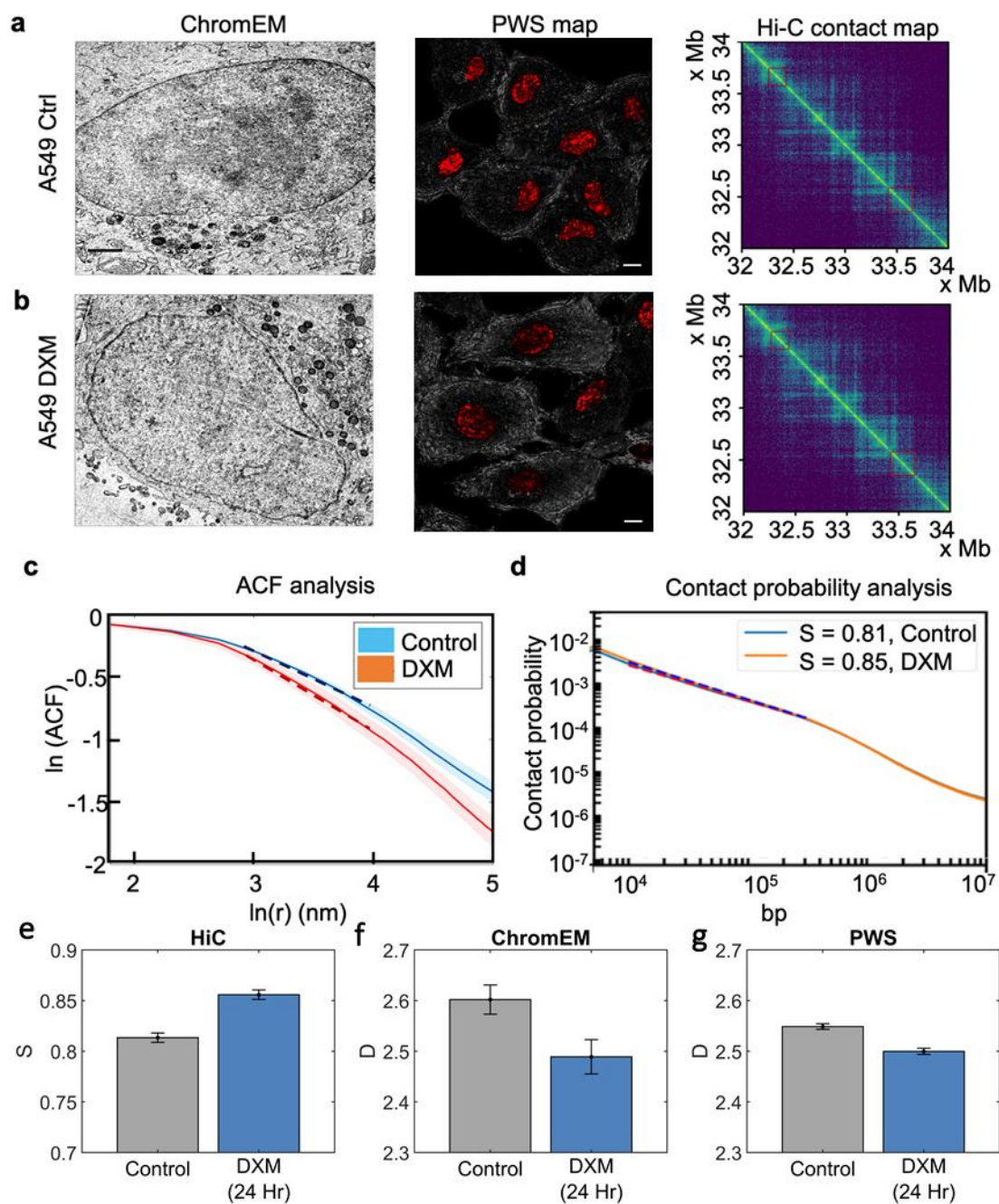


Figure 6.6 Measuring chromatin packing scaling alterations induced by dexamethasone in A549 cells. (a-b) Multi-platform characterization of A549 chromatin with and without DXM

treatment. From left to right: TEM images of the chromatin structure with ChromEM staining, scale bar: $1\mu\text{m}$. Hi-C contact map of the entire genome. The red square highlighted the regions with contact probability analysis. PWS map of the chromatin packing scaling, the black circle highlighted the nucleus. Qualitatively, from both TEM and PWS, after the DXM treatment, the chromatin packing became more homogeneous. (c) ACF analysis using TEM images of A549 chromatins. The average ACF of the control group (blue) is significantly different from the average ACF of the treated group (red). The shades indicate standard errors. The chromatin fractal dimension was measured inside the first fractal domain (20 nm to 54 nm) by linear fitting the ACF in log-log scale (dashed lines). (d) Contact probability analysis using the Hi-C contact map between 60 kb and 0.3 Mb bp. The power-law scaling s was quantified by linear regression (dotted line). (e–g) Chromatin packing scaling alterations induced by DXM treatment measured using ACF analysis of TEM images, contact probability analysis of Hi-C maps, and PWS. Across the platform, consistent changes were observed in chromatin packing.

The multi-technique platform was employed to capture the chromatin alterations induced by DXM treatment in BJ cells (Figure 6.7). Specifically, we tracked the chromatin changes at different time points using ChromEM (Figure 6.7 a), PWS (Figure 6.7 b) and Hi-C (Figure 6.7 c) to investigate the effect of continuous treatment. Using publicly available HiC data, we calculated a significant 1% and 5% increase in the scaling of chromatin contact probability S , 16 hrs and 32 hrs after DXM treatment (Figure 6.7 e). Using ChromEM, we found a 4% increase in Dac_f after 32 hrs of DXM treatment providing experimental evidence of the inverse relationship between the

scaling of chromatin packing and scaling of chromatin contact probability (Figure 6.7 d). Of particular interest, we used PWS to monitor live cells during DXM treatment and found a consistent decrease in D_{pws} (Figure 6.7 b). Together, these results validate the relationship between D and S , while also demonstrating the ability of PWS to characterize the scaling of chromatin packing, similarly to ChromEM, with live-cells and over time (Figure 6.7 f-h).

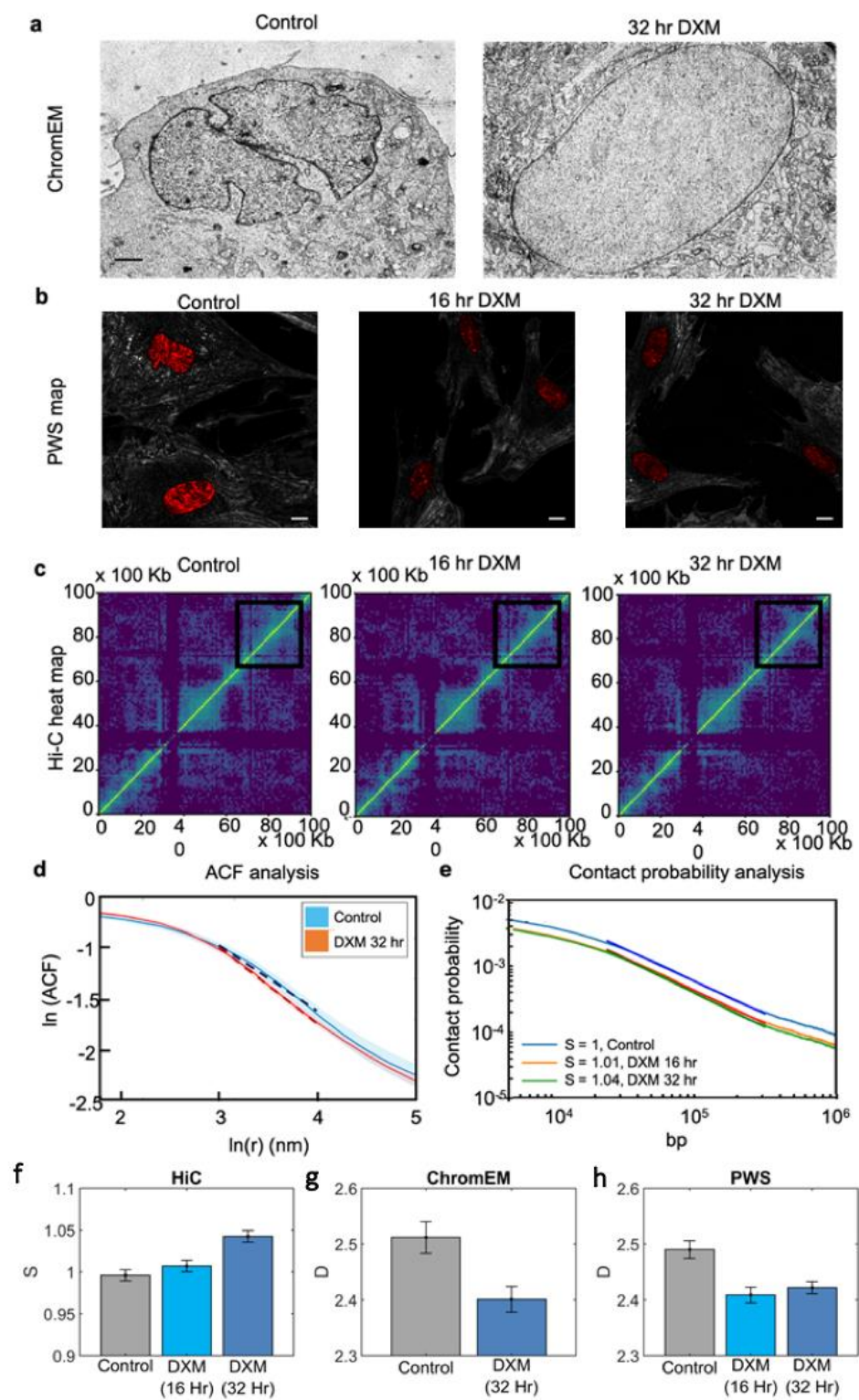


Figure 6.7 Measuring chromatin packing scaling alterations induced by dexamethasone in BJ cells. (a) Characterizing the chromatin packing at three different time points (0hr, 16hr, 32hr) after introducing DXM via the multi-technique platform. The upper panel showed the Hi-C results, and the bottom panel showed the PWS maps. In the PWS maps, the cell nucleus was highlighted by the black circle. The PWS signal continued to drop as we extend the treatment time. The TEM images of the BJ cells in the control group (b) also showed more heterogeneous chromatin distribution than the treated group after 32 hours (c). Scale bar: 1 μ m. (d) ACF analysis of the TEM images, the fractal dimension was calculated by linear regression (dashed lines) of the ACF curve in between 20 nm to 54 nm. (e) The contact probability analysis of the Hi-C map, the power-law scaling s was quantified by linear regression (dashed lines). (f-h) Fractal dimension quantified across the multi-technique platform. For ChromEM, only the control group and the 32 hr treatment were analyzed. In all modalities, we observed a consistent decreasing of D after the DXM treatment.

6.2.7 Discussions and Conclusions

We developed an MTMS platform for a more in-depth and detailed understanding of the 3D even 4D chromatin organization and its role in the regulation of the gene transcription. Using the multi-technique platform, we observed a power-law mass-scaling of the chromatin in the interphasic human lung cancer cell through ChromSTEM, and we observed mass fractals at different length scales with different scaling exponents. Furthermore, we established the non-monotonic relationship between the chromatin fractal dimension and the level of the gene transcription by correlating STORM with PWS, which agreed with the trend predicted by MD

simulations. Leveraging the fractal dimension as a proxy, we compared the changes of chromatin organization with dexamethasone-induced alterations measured independently from the ChromSTEM, the PWS, and the published Hi-C data. In all approaches, we observed the same trends in multiple cell lines at various time points and cross-validated the multi-technique platform with Hi-C. Unlike Hi-C, which takes snapshots of population-based chromatin information in fixed cells, we utilized the live-cell imaging and tracking ability of the multi-technique platform to study the evolution of genome organization between cell generations. With the abilities to characterize 3D even 4D chromatin organization with ultra-high resolution in all scales, the multi-technique platform can be employed to understand the role of chromatin organization in gene transcription, to unveil the mechanism of genetic diseases such as cancer and Parkinson's, and to assist the development of therapies to treat such diseases.

6.3 Correlative Super Resolution and Electron Microscopy (cSRAEM) to Relate Structure-Function Relation for Chromatin Organization and Gene Transcription

6.3.1 Adding Colors to the Electron Micrographs

Unlike fluorescence microscopy that the fluorophores themselves generate signals upon excitation, the image contrast of electron microscopy originates from the interaction between the sample and the incident electrons. Despite structural and mass-density information that electron microscopy can provide, the precise chemical composition is not quantifiable by imaging. To gain molecular specificities, electron spectroscopy techniques are developed. The elemental information can be gained through either electron dispersive X-ray spectroscopy (EDS or EDX) or electron energy loss spectroscopy (EELS) using the energy (loss) fingerprints. With calibration,

the two types of spectroscopy can be performed simultaneously on the same sample for 3D tomography reconstruction. However, as the efficiency of the EDS or EELS detector is limited, to maintain a good signal-to-noise ratio, the electron dose is greater than conventional imaging. For that reason, EDS or EELS are not suited for beam sensitive samples, such as biological samples.

With the advancement with the detector and cryogenic microscopy, it is now possible to perform EDS and EELS on biological sample to extract the metallic elemental distribution²⁰⁴. A more fundamental problem using electron microscopy to study genome organization and its role in regulating gene transcription is that the macromolecular groups in the chromatin are similar in terms of chemical composition. It is the unique molecularly configurations of the carbon, hydrogen, oxygen, nitrogen atoms that enables the molecular specificity in functioning. To meet this end, immune-gold labeling technique was developed. The immune-gold tag is an antibody conjugated with gold nanoparticles, which can label the antigen through antibody-interactions while creating contrast through gold-electron interactions²⁰⁵. As the image contrast originates from gold-electron interaction, the immune-gold labeling has enabled high-accuracy staining for one type of target molecule, because from the electron micrograph there is no distinction between gold particles conjugated to different antibodies. To label more than one type of molecules, a different type of antibodies needs to be conjugated with different types of heavy metals nanoparticles, and either EDS or EELS needs to be performed to distinguish the metals. This approach, again, is strongly restricted by the maximum amount of electron dose the biological sample can bear without significant beam damage.

One approach to mitigate this conflict is to separate the molecular specificity and the structural resolution and delegate different tasks to different imaging modalities. Correlative Light

and Electron Microscopy (CLEM) is a co-localized technique that conducts fluorescent light microscopy and high-resolution electron microscopy on the same sample in sequence²⁰⁶. The abundance fluorophores that have been developed over the past couple of decades provide vast possibilities of the biological molecules that can be labeled simultaneously. Since the joint of the two methods, a considerable amount of knowledge has been generated in how specific cellular structure participate in cell functions²⁰⁷.

6.3.2 Combining Super-Resolution and Electron Microscopy

However, the enormous discrepancies between the diffraction limit (200 nm) and the EM resolution (3-5 nm) make the alignment of the two types of images inaccurate. Moreover, for some biological systems, the spatial distribution of functioning groups in the nanometer range is crucial (e.g., mitochondria nucleoids distribution on the membrane), and the super-resolution fluorescent microscopy is indispensable²⁰⁸⁻²¹⁰. Another example that requires ultra-high resolution colocalization precision involves studies of chromatin structure and gene transcription. As gene transcription happens at the close vicinity of chromatin, and nuclear plasm is intrinsically crowded, to successfully localize the specific regions that are actively transcribing requires high-precision alignment.

To meet this end, herein, we introduced a dual-modality imaging technique, Correlative Super Resolution and Electron Microscopy (cSRAEM), which is able to precisely map the 3D spatial distribution of specific biological molecules (RNA Polymerase, histone tags, etc.) with sub 30-nm resolution and to reconstruct the 3D chromatin architecture down to single nucleosome

level on the same cell. The core techniques for cSRAEM are stochastic reconstruction microscopy (STORM, also known as PLM) and ChromEM²²⁹. In order to align the STORM images with the ChromEM images, 3D reconstruction was performed in both modalities.

6.3.3 Materials and Methods

Human ovarian cancer cell line (A2780) was employed as a model system to demonstrate cSRAEM imaging abilities. In general, the thickness of A2780 is around 7 μm , sectioning is required for electron microscopy and therefore destructive, we performed the STORM imaging before preparing the sample for electron microscopy. In the preliminary study, we focused on investigating if there is a relation between the 3D chromatin structure and gene transcription. For STORM, we labeled the RNA Polymerase II, a multi-protein complex that catalyzes the transcription to DNA to synthesize precursors of mRNA and most snRNA and microRNA, the concentration of which can be used to evaluate transcription level^{230,231}. After STORM acquisition, the sample was immediately prepared with ChromEM method to label the DNA. In order to locate the same cells with STORM measurement, the cells were grown in glass-bottom petri-dish with laser-carved grids on the bottom inside the dish (MatTek). The grids were recorded during STORM experiments. The ChromEM sample preparation was identical to other ChromSTEM experiments, and detailed protocol can be found in Appendix B. Particularly, only the cells with STORM images were photo-oxidized. After resin-embedding, serial-sections of A2780 were prepared by an ultramicrotome (UC7), and each section has a nominal thickness of 120 nm. Each section was imaged by TEM sequentially, and the tomography was reconstructed in IMOD. The workflow of cSRAEM is shown in Figure 6.8

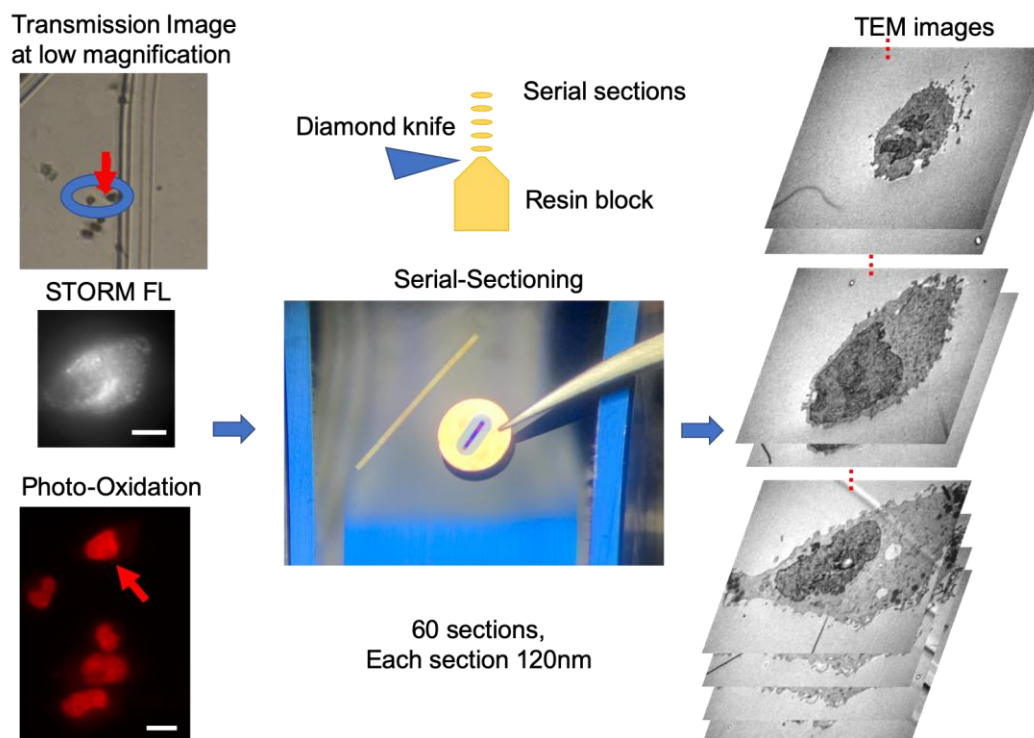


Figure 6.8 Workflow of cSRAEM. Before STORM imaging, a low magnification transmission image was taken using an optical microscope which was used as a roadmap together with the STORM fluorescent image (FL) to assist locating the same cells in the photo-oxidation. The arrows pointed to the same cell in the transmission image and the fluorescent image taken during the photo-oxidation. Scale bar: 5 μm . After resin-embedding, serial sections, with 120 nm in thickness for each section, were prepared by ultramicrotomy. For this cell, 60 sections were made. TEM was performed on each section in sequence, and the images were aligned in IMOD for tomography reconstruction.

6.3.4 Preliminary results for cSRAEM with A2780

As shown in Figure 6.9, the STORM reconstruction showed the distribution of RNA PolII, and the EM images showed the DNA distribution of the same cell.

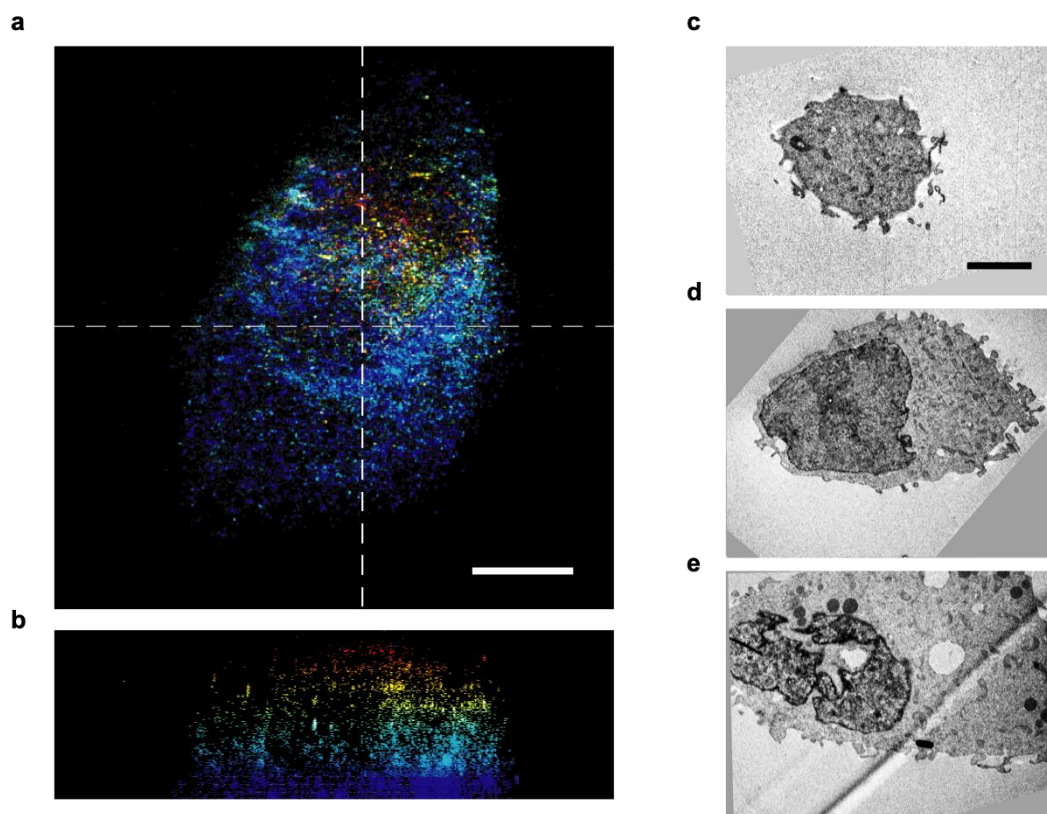


Figure 6.9 cSRAEM on an A2780 cell with RNA PolII labeling for STORM and ChromEM DNA labeling for EM. (a) Projection view of the 3D STORM reconstruction. Scale bar: 5 μm . (b) The side view of the 3D STORM reconstruction. For both (a) and (b), the color represents a different focal plane during acquisition. (c-e) TEM images of the top, middle, and bottom slice of the same cell. Scale bar: 2 μm .

6.3.5 Discussions and Conclusions

In the preliminary work, we did not attempt colocalization. The primary reason is that based on the STORM images, the RNA PolII also appeared to be significant in the cytoplasm. However, RNA PolII, as a transcription specific enzyme, should primarily locate within the nucleus. The almost random distribution of the RNA PolII signal throughout the cell indicated a loss of molecular specification of the antibody. Even with the current data, we were still able to identify similar nuclear envelope in both modalities. We believe in the future with improved labeling efficiency in STORM, and it is highly possible to achieve high precision co-localization in cSRAEM. By adding resolution matching the spatial distribution of functional groups to the 3D chromatin structure, cSRAEM has the potential of shedding lights into interrogating the structure-function relationship in epigenomics.

6.4 Concluding Comments

It is the goal of this thesis to highlight some of the incredible challenges and great opportunities facing the quantification of the genome organization. As the spatial-temporal-genomic characterization reached an unseen resolution, we are closer than ever to address some of the most fundamental questions in biology. New phenomena enabled by improvements in each technique ranging from computation, imaging, and sequencing are being observed daily. However, to truly leverage these advanced microscopes to understand genome structure and its relationship to biological functions will require an equal focus on bringing them together. As every technique only provides limited aspects of the full story, we need to combine the strength of individual methods to create a complete picture covering the evolving genome organization at both single

cell level and across populations. We are quickly moving from a world where we only need to 'see' chromatin, to one where multi-scale and multi-omics information must be interpreted coherently. The field of epigenomics is at the crossroad of consolidating imaging, sequencing, computation, even gene-editing platform. Future work will be painstaking, but the enormous potential of understanding the fundamentals of the miracle of life will increasingly present itself to entrepreneurial researchers.

REFERENCES

- 1 Venkatesh, S. & Workman, J. L. Histone exchange, chromatin structure and the regulation of transcription. *Nat Rev Mol Cell Biol* **16**, 178-189, doi:10.1038/nrm3941 (2015).
- 2 Maeshima, K., Imai, R., Tamura, S. & Nozaki, T. Chromatin as dynamic 10-nm fibers. *Chromosoma* **123**, 225-237, doi:10.1007/s00412-014-0460-2 (2014).
- 3 Lieberman-Aiden, E. *et al.* Comprehensive mapping of long-range interactions reveals folding principles of the human genome. *Science* **326**, 289-293, doi:10.1126/science.1181369 (2009).
- 4 Yuan, W. *et al.* Dense chromatin activates Polycomb repressive complex 2 to regulate H3 lysine 27 methylation. *Science* **337**, 971-975, doi:10.1126/science.1225237 (2012).
- 5 Pajerowski, J. D., Dahl, K. N., Zhong, F. L., Sammak, P. J. & Discher, D. E. Physical plasticity of the nucleus in stem cell differentiation. *Proc Natl Acad Sci U S A* **104**, 15619-15624, doi:10.1073/pnas.0702576104 (2007).
- 6 Irianto, J. *et al.* Osmotic challenge drives rapid and reversible chromatin condensation in chondrocytes. *Biophys J* **104**, 759-769, doi:10.1016/j.bpj.2013.01.006 (2013).
- 7 Almassalha, L. M. *et al.* The Greater Genomic Landscape: The Heterogeneous Evolution of Cancer. *Cancer Res* **76**, 5605-5609, doi:10.1158/0008-5472.CAN-16-0585 (2016).
- 8 Almassalha, L. M. *et al.* The Global Relationship between Chromatin Physical Topology, Fractal Structure, and Gene Expression. *Sci Rep* **7**, 41061, doi:10.1038/srep41061 (2017).
- 9 Matsuda, H., Putzel, G. G., Backman, V. & Szleifer, I. Macromolecular crowding as a regulator of gene transcription. *Biophys J* **106**, 1801-1810, doi:10.1016/j.bpj.2014.02.019 (2014).

- 10 Buenrostro, J. D., Giresi, P. G., Zaba, L. C., Chang, H. Y. & Greenleaf, W. J. Transposition of native chromatin for fast and sensitive epigenomic profiling of open chromatin, DNA-binding proteins and nucleosome position. *Nat Methods* **10**, 1213-1218, doi:10.1038/nmeth.2688 (2013).
- 11 Song, L. & Crawford, G. E. DNase-seq: a high-resolution technique for mapping active gene regulatory elements across the genome from mammalian cells. *Cold Spring Harb Protoc* **2010**, pdb prot5384, doi:10.1101/pdb.prot5384 (2010).
- 12 Ren, B. *et al.* Genome-wide location and function of DNA binding proteins. *Science* **290**, 2306-2309, doi:10.1126/science.290.5500.2306 (2000).
- 13 Consortium, E. P. An integrated encyclopedia of DNA elements in the human genome. *Nature* **489**, 57 (2012).
- 14 Hawkins, R. D., Hon, G. C. & Ren, B. Next-generation genomics: an integrative approach. *Nat Rev Genet* **11**, 476-486, doi:10.1038/nrg2795 (2010).
- 15 van Steensel, B. & Dekker, J. Genomics tools for unraveling chromosome architecture. *Nat Biotechnol* **28**, 1089-1095, doi:10.1038/nbt.1680 (2010).
- 16 van Berkum, N. L. *et al.* Hi-C: a method to study the three-dimensional architecture of genomes. *J Vis Exp*, e1869, doi:10.3791/1869 (2010).
- 17 Sims, D., Sudbery, I., Ilott, N. E., Heger, A. & Ponting, C. P. Sequencing depth and coverage: key considerations in genomic analyses. *Nat Rev Genet* **15**, 121-132, doi:10.1038/nrg3642 (2014).
- 18 Ong, C. T. & Corces, V. G. CTCF: an architectural protein bridging genome topology and function. *Nat Rev Genet* **15**, 234-246, doi:10.1038/nrg3663 (2014).

- 19 Mifsud, B. *et al.* Mapping long-range promoter contacts in human cells with high-resolution capture Hi-C. *Nat Genet* **47**, 598-606, doi:10.1038/ng.3286 (2015).
- 20 Jones, S. A., Shim, S. H., He, J. & Zhuang, X. Fast, three-dimensional super-resolution imaging of live cells. *Nat Methods* **8**, 499-508, doi:10.1038/nmeth.1605 (2011).
- 21 Shim, S. H. *et al.* Super-resolution fluorescence imaging of organelles in live cells with photoswitchable membrane probes. *Proc Natl Acad Sci U S A* **109**, 13978-13983, doi:10.1073/pnas.1201882109 (2012).
- 22 Huang, B., Babcock, H. & Zhuang, X. Breaking the diffraction barrier: super-resolution imaging of cells. *Cell* **143**, 1047-1058, doi:10.1016/j.cell.2010.12.002 (2010).
- 23 Bintu, B. *et al.* Super-resolution chromatin tracing reveals domains and cooperative interactions in single cells. *Science* **362**, eaau1783, doi:10.1126/science.aau1783 (2018).
- 24 Almassalha, L. M. *et al.* Label-free imaging of the native, living cellular nanoarchitecture using partial-wave spectroscopic microscopy. *Proceedings of the National Academy of Sciences of the United States of America* **113**, E6372-E6381, doi:10.1073/pnas.1608198113 (2016).
- 25 Subramanian, H. *et al.* Nanoscale cellular changes in field carcinogenesis detected by partial wave spectroscopy. *Cancer Res* **69**, 5357-5363, doi:10.1158/0008-5472.CAN-08-3895 (2009).
- 26 Scott, M. C. *et al.* Electron tomography at 2.4-angstrom resolution. *Nature* **483**, 444-447, doi:10.1038/nature10934 (2012).
- 27 Hildebrand, D. G. C. *et al.* Whole-brain serial-section electron microscopy in larval zebrafish. *Nature* **545**, 345-349, doi:10.1038/nature22356 (2017).

- 28 Frey, T. G. & Mannella, C. A. The internal structure of mitochondria. *Trends Biochem Sci* **25**, 319-324 (2000).
- 29 Mikula, S., Binding, J. & Denk, W. Staining and embedding the whole mouse brain for electron microscopy. *Nat Methods* **9**, 1198-1201, doi:10.1038/nmeth.2213 (2012).
- 30 Liu, H. *et al.* Atomic structure of human adenovirus by cryo-EM reveals interactions among protein networks. *Science* **329**, 1038-1043, doi:10.1126/science.1187433 (2010).
- 31 Ngo, J. T. *et al.* Click-EM for imaging metabolically tagged nonprotein biomolecules. *Nat Chem Biol* **12**, 459-465, doi:10.1038/nchembio.2076 (2016).
- 32 Ou, H. D. *et al.* ChromEMT: Visualizing 3D chromatin structure and compaction in interphase and mitotic cells. *Science* **357**, eaag0025, doi:10.1126/science.aag0025 (2017).
- 33 Strom, A. R. *et al.* Phase separation drives heterochromatin domain formation. *Nature* **547**, 241-245, doi:10.1038/nature22989 (2017).
- 34 Larson, A. G. *et al.* Liquid droplet formation by HP1alpha suggests a role for phase separation in heterochromatin. *Nature* **547**, 236-240, doi:10.1038/nature22822 (2017).
- 35 Naughton, C. *et al.* Transcription forms and remodels supercoiling domains unfolding large-scale chromatin structures. *Nat Struct Mol Biol* **20**, 387-395, doi:10.1038/nsmb.2509 (2013).
- 36 Gilbert, N. & Allan, J. Supercoiling in DNA and chromatin. *Curr Opin Genet Dev* **25**, 15-21, doi:10.1016/j.gde.2013.10.013 (2014).
- 37 Androulakis, J. *et al.* Thermoelectrics from abundant chemical elements: high-performance nanostructured PbSe-PbS. *J Am Chem Soc* **133**, 10920-10927, doi:10.1021/ja203022c (2011).

- 38 Ji, L. W., Lin, Z., Alcoutlabi, M. & Zhang, X. W. Recent developments in nanostructured anode materials for rechargeable lithium-ion batteries. *Energ Environ Sci* **4**, 2682-2699, doi:10.1039/c0ee00699h (2011).
- 39 Friedrich, H., de Jongh, P. E., Verkleij, A. J. & de Jong, K. P. Electron tomography for heterogeneous catalysts and related nanostructured materials. *Chem Rev* **109**, 1613-1629, doi:10.1021/cr800434t (2009).
- 40 Xin, H. L. *et al.* Atomic-resolution spectroscopic imaging of ensembles of nanocatalyst particles across the life of a fuel cell. *Nano Lett* **12**, 490-497, doi:10.1021/nl203975u (2012).
- 41 Horcajada, P. *et al.* Porous metal–organic-framework nanoscale carriers as a potential platform for drug delivery and imaging. *Nature Materials* **9**, 172 (2010).
- 42 Chou, S. S. *et al.* Nanoscale graphene oxide (nGO) as artificial receptors: implications for biomolecular interactions and sensing. *J Am Chem Soc* **134**, 16725-16733, doi:10.1021/ja306767y (2012).
- 43 Williams, D. B. & Carter, C. B. *Transmission electron microscopy : a textbook for materials science*. 2nd edn, (Springer, 2008).
- 44 Wang, P. *et al.* Bright-field scanning confocal electron microscopy using a double aberration-corrected transmission electron microscope. *Ultramicroscopy* **111**, 877-886, doi:10.1016/j.ultramic.2010.10.012 (2011).
- 45 Lynch, D., Moodie, A. F. & O'keefe, M. n-Beam lattice images. V. The use of the charge-density approximation in the interpretation of lattice images. *Acta Crystallographica*

- Section A: Crystal Physics, Diffraction, Theoretical and General Crystallography* **31**, 300-307 (1975).
- 46 Scherzer, O. The Theoretical Resolution Limit of the Electron Microscope. *Journal of Applied Physics* **20**, 20-29, doi:Doi 10.1063/1.1698233 (1949).
- 47 Völkl, E., Allard, L. F. & Joy, D. C. *Introduction to electron holography*. (Springer Science & Business Media, 2013).
- 48 Coene, W., Janssen, G., de Beeck, M. O. & Van Dyck, D. Phase retrieval through focus variation for ultra-resolution in field-emission transmission electron microscopy. *Physical Review Letters* **69**, 3743 (1992).
- 49 Crewe, A. V. Scanning transmission electron microscopy. *J Microsc* **100**, 247-259 (1974).
- 50 Batson, P. E., Dellby, N. & Krivanek, O. L. Sub-ångstrom resolution using aberration corrected electron optics. *Nature* **418**, 617 (2002).
- 51 Weyland, M., Midgley, P. A. & Thomas, J. M. Electron tomography of nanoparticle catalysts on porous supports: A new technique based on Rutherford scattering. *J Phys Chem B* **105**, 7882-7886, doi:10.1021/jp011566s (2001).
- 52 Gentsch, P., Gilde, H. & Reimer, L. Measurement of the top bottom effect in scanning transmission electron microscopy of thick amorphous specimens. *Journal of Microscopy* **100**, 81-92 (1974).
- 53 Reimer, L. & Gentsch, P. Superposition of chromatic error and beam broadening in transmission electron microscopy of thick carbon and organic specimens. *Ultramicroscopy* **1**, 1-5 (1975).

- 54 Pennycook, S. J. & Jesson, D. E. Atomic Resolution Z-Contrast Imaging of Interfaces. *Acta Metallurgica Et Materialia* **40**, S149-S159, doi:Doi 10.1016/0956-7151(92)90275-J (1992).
- 55 Midgley, P. A. & Weyland, M. 3D electron microscopy in the physical sciences: the development of Z-contrast and EFTEM tomography. *Ultramicroscopy* **96**, 413-431, doi:10.1016/S0304-3991(03)00105-0 (2003).
- 56 McIntosh, R., Nicastro, D. & Mastronarde, D. New views of cells in 3D: an introduction to electron tomography. *Trends Cell Biol* **15**, 43-51, doi:10.1016/j.tcb.2004.11.009 (2005).
- 57 Lucic, V., Forster, F. & Baumeister, W. Structural studies by electron tomography: from cells to molecules. *Annu Rev Biochem* **74**, 833-865, doi:10.1146/annurev.biochem.73.011303.074112 (2005).
- 58 Leis, A., Rockel, B., Andrees, L. & Baumeister, W. Visualizing cells at the nanoscale. *Trends Biochem Sci* **34**, 60-70, doi:10.1016/j.tibs.2008.10.011 (2009).
- 59 Hoenger, A. & McIntosh, J. R. Probing the macromolecular organization of cells by electron tomography. *Curr Opin Cell Biol* **21**, 89-96, doi:10.1016/j.ceb.2008.12.003 (2009).
- 60 Beck, M. & Baumeister, W. Cryo-Electron Tomography: Can it Reveal the Molecular Sociology of Cells in Atomic Detail? *Trends in cell biology* **26**, 825-837 (2016).
- 61 Kollmer, M. *et al.* Electron tomography reveals the fibril structure and lipid interactions in amyloid deposits. *Proc Natl Acad Sci U S A* **113**, 5604-5609, doi:10.1073/pnas.1523496113 (2016).
- 62 Frank, J. *Electron tomography*. (Springer, 1992).

- 63 Kremer, J. R., Mastronarde, D. N. & McIntosh, J. R. Computer visualization of three-dimensional image data using IMOD. *J Struct Biol* **116**, 71-76, doi:10.1006/jsbi.1996.0013 (1996).
- 64 Medalia, O. *et al.* Macromolecular architecture in eukaryotic cells visualized by cryoelectron tomography. *Science* **298**, 1209-1213, doi:10.1126/science.1076184 (2002).
- 65 He, W. *et al.* FcRn-mediated antibody transport across epithelial cells revealed by electron tomography. *Nature* **455**, 542-546, doi:10.1038/nature07255 (2008).
- 66 Patla, I. *et al.* Dissecting the molecular architecture of integrin adhesion sites by cryoelectron tomography. *Nat Cell Biol* **12**, 909-915, doi:10.1038/ncb2095 (2010).
- 67 Sirohi, D. *et al.* The 3.8 Å resolution cryo-EM structure of Zika virus. *Science* **352**, 467-470 (2016).
- 68 Beck, M. *et al.* Nuclear pore complex structure and dynamics revealed by cryoelectron tomography. *Science* **306**, 1387-1390, doi:10.1126/science.1104808 (2004).
- 69 Kurner, J., Frangakis, A. S. & Baumeister, W. Cryo-electron tomography reveals the cytoskeletal structure of *Spiroplasma melliferum*. *Science* **307**, 436-438, doi:10.1126/science.1104031 (2005).
- 70 Baumeister, W. Electron tomography: towards visualizing the molecular organization of the cytoplasm. *Curr Opin Struct Biol* **12**, 679-684 (2002).
- 71 Liu, J., Bartesaghi, A., Borgnia, M. J., Sapiro, G. & Subramaniam, S. Molecular architecture of native HIV-1 gp120 trimers. *Nature* **455**, 109-113, doi:10.1038/nature07159 (2008).

- 72 Webb, R. H. Confocal optical microscopy. *Rep Prog Phys* **59**, 427-471, doi:Doi:10.1088/0034-4885/59/3/003 (1996).
- 73 Cnudde, V. *et al.* Recent progress in X-ray CT as a geosciences tool. *Appl Geochem* **21**, 826-832, doi:10.1016/j.apgeochem.2006.02.010 (2006).
- 74 Chen, S. *et al.* The Bionanoprobe: hard X-ray fluorescence nanoprobe with cryogenic capabilities. *J Synchrotron Radiat* **21**, 66-75, doi:10.1107/S1600577513029676 (2014).
- 75 Jiang, Y. *et al.* X-ray structure of a voltage-dependent K⁺ channel. *Nature* **423**, 33-41, doi:10.1038/nature01580 (2003).
- 76 Shi, D., Nannenga, B. L., Iadanza, M. G. & Gonen, T. Three-dimensional electron crystallography of protein microcrystals. *Elife* **2**, e01345, doi:10.7554/eLife.01345 (2013).
- 77 La Mar, G. N., Horrocks, W. D. & Holm, R. H. *NMR of paramagnetic molecules: principles and applications*. (Elsevier, 2016).
- 78 Risco, C. *et al.* Three-Dimensional Imaging of Viral Infections. *Annu Rev Virol* **1**, 453-473, doi:10.1146/annurev-virology-031413-085351 (2014).
- 79 Xu, P., Donaldson, L. A., Gergely, Z. R. & Staehelin, L. A. Dual-axis electron tomography: a new approach for investigating the spatial organization of wood cellulose microfibrils. *Wood Sci Technol* **41**, 101-116, doi:10.1007/s00226-006-0088-3 (2007).
- 80 Mastronarde, D. N. Dual-axis tomography: an approach with alignment methods that preserve resolution. *J Struct Biol* **120**, 343-352, doi:10.1006/jsbi.1997.3919 (1997).
- 81 Sousa, A. A., Azari, A. A., Zhang, G. & Leapman, R. D. Dual-axis electron tomography of biological specimens: Extending the limits of specimen thickness with bright-field STEM imaging. *J Struct Biol* **174**, 107-114, doi:10.1016/j.jsb.2010.10.017 (2011).

- 82 Castano-Diez, D., Al-Amoudi, A., Glynn, A. M., Seybert, A. & Frangakis, A. S. Fiducial-less alignment of cryo-sections. *J Struct Biol* **159**, 413-423, doi:10.1016/j.jsb.2007.04.014 (2007).
- 83 Castano-Diez, D., Scheffer, M., Al-Amoudi, A. & Frangakis, A. S. Alignator: a GPU powered software package for robust fiducial-less alignment of cryo tilt-series. *J Struct Biol* **170**, 117-126, doi:10.1016/j.jsb.2010.01.014 (2010).
- 84 Mastronarde, D. N. Automated electron microscope tomography using robust prediction of specimen movements. *J Struct Biol* **152**, 36-51, doi:10.1016/j.jsb.2005.07.007 (2005).
- 85 Mastronarde, D. N. in *Electron Tomography*, 163-185 (Springer, 2007).
- 86 Fernandez, J. J. Computational methods for electron tomography. *Micron* **43**, 1010-1030, doi:10.1016/j.micron.2012.05.003 (2012).
- 87 Venkatakrisnan, S. V. *et al.* A model based iterative reconstruction algorithm for high angle annular dark field-scanning transmission electron microscope (HAADF-STEM) tomography. *IEEE Trans Image Process* **22**, 4532-4544, doi:10.1109/TIP.2013.2277784 (2013).
- 88 Saghi, Z. *et al.* Reduced-dose and high-speed acquisition strategies for multi-dimensional electron microscopy. *Adv Struct Chem Imag* **1**, 1-10, doi:ARTN 710.1186/s40679-015-0007-5 (2015).
- 89 Donati, L. *et al.* in *Proceedings of the Fourteenth IEEE International Symposium on Biomedical Imaging: From Nano to Macro (ISBI' 17)*. 23–27 (IEEE).
- 90 Leary, R., Saghi, Z., Midgley, P. A. & Holland, D. J. Compressed sensing electron tomography. *Ultramicroscopy* **131**, 70-91, doi:10.1016/j.ultramic.2013.03.019 (2013).

- 91 Gursoy, D., De Carlo, F., Xiao, X. & Jacobsen, C. TomoPy: a framework for the analysis of synchrotron tomographic data. *J Synchrotron Radiat* **21**, 1188-1193, doi:10.1107/S1600577514013939 (2014).
- 92 Weyland, M. & Midgley, P. in *Transmission Electron Microscopy* 343-376 (Springer, 2016).
- 93 Tanurna, S. Calculations of electron inelastic mean free paths. *Surface and Interface analysis* **17**, 927-939 (1991).
- 94 Martone, M. E., Deerinck, T. J., Yamada, N., Bushong, E. & Ellisman, M. H. Correlated 3D light and electron microscopy: Use of high voltage electron microscopy and electron tomography for imaging large biological structures. *J Histotechnol* **23**, 261-270, doi:DOI 10.1179/his.2000.23.3.261 (2000).
- 95 Han, K. F., Sedat, J. W. & Agard, D. A. Practical image restoration of thick biological specimens using multiple focus levels in transmission electron microscopy. *J Struct Biol* **120**, 237-244, doi:10.1006/jsbi.1997.3914 (1997).
- 96 Hayworth, K., Kasthuri, N., Schalek, R. & Lichtman, J. Automating the collection of ultrathin serial sections for large volume TEM reconstructions. *Microscopy and Microanalysis* **12**, 86-87 (2006).
- 97 Bleck, C. K. *et al.* Comparison of different methods for thin section EM analysis of *Mycobacterium smegmatis*. *J Microsc* **237**, 23-38, doi:10.1111/j.1365-2818.2009.03299.x (2010).

- 98 Al-Amoudi, A., Dubochet, J., Gnaegi, H., Luthi, W. & Studer, D. An oscillating cryo-knife reduces cutting-induced deformation of vitreous ultrathin sections. *J Microsc* **212**, 26-33 (2003).
- 99 Al-Amoudi, A., Studer, D. & Dubochet, J. Cutting artefacts and cutting process in vitreous sections for cryo-electron microscopy. *J Struct Biol* **150**, 109-121, doi:10.1016/j.jsb.2005.01.003 (2005).
- 100 Hohmann-Marriott, M. F. *et al.* Nanoscale 3D cellular imaging by axial scanning transmission electron tomography. *Nat Methods* **6**, 729-731, doi:10.1038/nmeth.1367 (2009).
- 101 Sousa, A. A., Hohmann-Marriott, M. F., Zhang, G. & Leapman, R. D. Monte Carlo electron-trajectory simulations in bright-field and dark-field STEM: implications for tomography of thick biological sections. *Ultramicroscopy* **109**, 213-221, doi:10.1016/j.ultramic.2008.10.005 (2009).
- 102 Sousa, A. A. & Leapman, R. D. Development and application of STEM for the biological sciences. *Ultramicroscopy* **123**, 38-49, doi:10.1016/j.ultramic.2012.04.005 (2012).
- 103 Vazquez-Nin, G. H., Biggiogera, M. & Echeverria, O. M. Activation of osmium ammine by SO₂-generating chemicals for EM Feulgen-type staining of DNA. *Eur J Histochem* **39**, 101-106 (1995).
- 104 Bremer, A., Henn, C., Engel, A., Baumeister, W. & Aebi, U. Has negative staining still a place in biomacromolecular electron microscopy? *Ultramicroscopy* **46**, 85-111 (1992).
- 105 Watson, M. L. Staining of tissue sections for electron microscopy with heavy metals. *The Journal of Cell Biology* **4**, 475-478 (1958).

- 106 Angermuller, S. & Fahimi, H. D. Imidazole-buffered osmium tetroxide: an excellent stain for visualization of lipids in transmission electron microscopy. *Histochem J* **14**, 823-835 (1982).
- 107 Locke, M. & Krishnan, N. Hot alcoholic phosphotungstic acid and uranyl acetate as routine stains for thick and thin sections. *J Cell Biol* **50**, 550-557, doi:10.1083/jcb.50.2.550 (1971).
- 108 Stempak, J. G. & Ward, R. T. An Improved Staining Method for Electron Microscopy. *J Cell Biol* **22**, 697-701, doi:10.1083/jcb.22.3.697 (1964).
- 109 Venable, J. H. & Coggeshall, R. A Simplified Lead Citrate Stain for Use in Electron Microscopy. *J Cell Biol* **25**, 407-408, doi:10.1083/jcb.25.2.407 (1965).
- 110 Stirling, J. W. Immuno- and affinity probes for electron microscopy: a review of labeling and preparation techniques. *J Histochem Cytochem* **38**, 145-157, doi:10.1177/38.2.2405054 (1990).
- 111 De Mey, J., Moeremans, M., Geuens, G., Nuydens, R. & De Brabander, M. High resolution light and electron microscopic localization of tubulin with the IGS (immuno gold staining) method. *Cell Biol Int Rep* **5**, 889-899 (1981).
- 112 Holgate, C. S., Jackson, P., Cowen, P. N. & Bird, C. C. Immunogold-silver staining: new method of immunostaining with enhanced sensitivity. *J Histochem Cytochem* **31**, 938-944, doi:10.1177/31.7.6189883 (1983).
- 113 Manuelidis, L., Langer-Safer, P. R. & Ward, D. C. High-resolution mapping of satellite DNA using biotin-labeled DNA probes. *J Cell Biol* **95**, 619-625, doi:10.1083/jcb.95.2.619 (1982).

- 114 Sosinsky, G. E., Giepmans, B. N., Deerinck, T. J., Gaietta, G. M. & Ellisman, M. H. Markers for correlated light and electron microscopy. *Methods Cell Biol* **79**, 575-591, doi:10.1016/S0091-679X(06)79023-9 (2007).
- 115 Egerton, R. F., Li, P. & Malac, M. Radiation damage in the TEM and SEM. *Micron* **35**, 399-409, doi:10.1016/j.micron.2004.02.003 (2004).
- 116 Glaeser, R. M. Limitations to Significant Information in Biological Electron Microscopy as a Result of Radiation Damage. *J Ultra Mol Struct R* **36**, 466-&, doi:Doi 10.1016/S0022-5320(71)80118-1 (1971).
- 117 Egerton, R. F. Choice of operating voltage for a transmission electron microscope. *Ultramicroscopy* **145**, 85-93, doi:10.1016/j.ultramic.2013.10.019 (2014).
- 118 Henderson, R. The potential and limitations of neutrons, electrons and X-rays for atomic resolution microscopy of unstained biological molecules. *Q Rev Biophys* **28**, 171-193 (1995).
- 119 Mamaghanian, H., Khaled, N., Atienza, D. & Vandergheynst, P. Compressed sensing for real-time energy-efficient ECG compression on wireless body sensor nodes. *IEEE Trans Biomed Eng* **58**, 2456-2466, doi:10.1109/TBME.2011.2156795 (2011).
- 120 Candes, E. J. The restricted isometry property and its implications for compressed sensing. *Cr Math* **346**, 589-592, doi:10.1016/j.crma.2008.03.014 (2008).
- 121 Willett, R. M., Marcia, R. F. & Nichols, J. M. Compressed sensing for practical optical imaging systems: a tutorial. *Opt Eng* **50**, 072601, doi:Artn 07260110.1117/1.3596602 (2011).

- 122 Choi, K. *et al.* Compressed sensing based cone-beam computed tomography reconstruction with a first-order method. *Med Phys* **37**, 5113-5125, doi:10.1118/1.3481510 (2010).
- 123 Lustig, M., Donoho, D. & Pauly, J. M. Sparse MRI: The application of compressed sensing for rapid MR imaging. *Magn Reson Med* **58**, 1182-1195, doi:10.1002/mrm.21391 (2007).
- 124 Hujsak, K., Myers, B. D., Roth, E., Li, Y. & Dravid, V. P. Suppressing Electron Exposure Artifacts: An Electron Scanning Paradigm with Bayesian Machine Learning. *Microsc Microanal* **22**, 778-788, doi:10.1017/S1431927616011417 (2016).
- 125 Beche, A., Goris, B., Freitag, B. & Verbeeck, J. Development of a fast electromagnetic beam blanker for compressed sensing in scanning transmission electron microscopy. *Appl Phys Lett* **108**, 093103, doi:Artn 09310310.1063/1.4943086 (2016).
- 126 Candes, E. & Romberg, J. Sparsity and incoherence in compressive sampling. *Inverse Probl* **23**, 969-985, doi:10.1088/0266-5611/23/3/008 (2007).
- 127 Guay, M. D., Czaja, W., Aronova, M. A. & Leapman, R. D. Compressed Sensing Electron Tomography for Determining Biological Structure. *Sci Rep* **6**, 27614, doi:10.1038/srep27614 (2016).
- 128 Mannella, C. A., Buttle, K., Rath, B. K. & Marko, M. Electron microscopic tomography of rat-liver mitochondria and their interactions with the endoplasmic reticulum. *Biofactors* **8**, 225-228, doi:DOI 10.1002/biof.5520080309 (1998).
- 129 Marsh, B. J., Mastronarde, D. N., Buttle, K. F., Howell, K. E. & McIntosh, J. R. Organellar relationships in the Golgi region of the pancreatic beta cell line, HIT-T15, visualized by high resolution electron tomography. *Proc Natl Acad Sci U S A* **98**, 2399-2406, doi:10.1073/pnas.051631998 (2001).

- 130 Zeuschner, D. *et al.* Immuno-electron tomography of ER exit sites reveals the existence of free COPII-coated transport carriers. *Nat Cell Biol* **8**, 377-383, doi:10.1038/ncb1371 (2006).
- 131 Koning, R. I. & Koster, A. J. Cryo-electron tomography in biology and medicine. *Ann Anat* **191**, 427-445, doi:10.1016/j.aanat.2009.04.003 (2009).
- 132 Al-Amoudi, A. *et al.* Cryo-electron microscopy of vitreous sections. *The EMBO journal* **23**, 3583-3588 (2004).
- 133 Midgley, P. A. & Dunin-Borkowski, R. E. Electron tomography and holography in materials science. *Nat Mater* **8**, 271-280, doi:10.1038/nmat2406 (2009).
- 134 Stark, H., Zemlin, F. & Boettcher, C. Electron radiation damage to protein crystals of bacteriorhodopsin at different temperatures. *Ultramicroscopy* **63**, 75-79, doi:10.1016/0304-3991(96)00045-9 (1996).
- 135 Mastronarde, D. N. & Held, S. R. Automated tilt series alignment and tomographic reconstruction in IMOD. *J Struct Biol* **197**, 102-113, doi:10.1016/j.jsb.2016.07.011 (2017).
- 136 Çelebi. Çelebi Tutorial Volume Rendering, <https://www.byclb.com/TR/Tutorials/volume_rendering/images/image013.jpg>
- 137 Steinbrecht, R. A. & Müller, M. in *Cryotechniques in biological electron microscopy* 149-172 (Springer, 1987).
- 138 Yu, M. & Ren, B. The Three-Dimensional Organization of Mammalian Genomes. *Annu Rev Cell Dev Biol* **33**, 265-289, doi:10.1146/annurev-cellbio-100616-060531 (2017).
- 139 Clowney, E. J. *et al.* Nuclear aggregation of olfactory receptor genes governs their monogenic expression. *Cell* **151**, 724-737, doi:10.1016/j.cell.2012.09.043 (2012).

- 140 Bickmore, W. A. The spatial organization of the human genome. *Annu Rev Genomics Hum Genet* **14**, 67-84, doi:10.1146/annurev-genom-091212-153515 (2013).
- 141 Gorkin, D. U., Leung, D. & Ren, B. The 3D genome in transcriptional regulation and pluripotency. *Cell Stem Cell* **14**, 762-775, doi:10.1016/j.stem.2014.05.017 (2014).
- 142 van Steensel, B. & Belmont, A. S. Lamina-Associated Domains: Links with Chromosome Architecture, Heterochromatin, and Gene Repression. *Cell* **169**, 780-791, doi:10.1016/j.cell.2017.04.022 (2017).
- 143 Dekker, J. & Mirny, L. The 3D Genome as Moderator of Chromosomal Communication. *Cell* **164**, 1110-1121, doi:10.1016/j.cell.2016.02.007 (2016).
- 144 Tang, Z. *et al.* CTCF-Mediated Human 3D Genome Architecture Reveals Chromatin Topology for Transcription. *Cell* **163**, 1611-1627, doi:10.1016/j.cell.2015.11.024 (2015).
- 145 Almassalha, L. M. *et al.* Macrogenomic engineering via modulation of the scaling of chromatin packing density. *Nat Biomed Eng* **1**, 902-913, doi:10.1038/s41551-017-0153-2 (2017).
- 146 Li, G. *et al.* Extensive promoter-centered chromatin interactions provide a topological basis for transcription regulation. *Cell* **148**, 84-98, doi:10.1016/j.cell.2011.12.014 (2012).
- 147 Wang, H. *et al.* CRISPR-Mediated Programmable 3D Genome Positioning and Nuclear Organization. *Cell* **175**, 1405-1417 e1414, doi:10.1016/j.cell.2018.09.013 (2018).
- 148 Montavon, T. *et al.* A regulatory archipelago controls Hox genes transcription in digits. *Cell* **147**, 1132-1145, doi:10.1016/j.cell.2011.10.023 (2011).

- 149 Furlan-Magaril, M., Varnai, C., Nagano, T. & Fraser, P. 3D genome architecture from populations to single cells. *Curr Opin Genet Dev* **31**, 36-41, doi:10.1016/j.gde.2015.04.004 (2015).
- 150 Iwafuchi-Doi, M. & Zaret, K. S. Pioneer transcription factors in cell reprogramming. *Genes Dev* **28**, 2679-2692, doi:10.1101/gad.253443.114 (2014).
- 151 Zhang, Z. & Pugh, B. F. High-resolution genome-wide mapping of the primary structure of chromatin. *Cell* **144**, 175-186, doi:10.1016/j.cell.2011.01.003 (2011).
- 152 Gibcus, J. H. & Dekker, J. The hierarchy of the 3D genome. *Mol Cell* **49**, 773-782, doi:10.1016/j.molcel.2013.02.011 (2013).
- 153 Rao, S. S. *et al.* A 3D map of the human genome at kilobase resolution reveals principles of chromatin looping. *Cell* **159**, 1665-1680, doi:10.1016/j.cell.2014.11.021 (2014).
- 154 Le Gros, M. A. *et al.* Soft X-Ray Tomography Reveals Gradual Chromatin Compaction and Reorganization during Neurogenesis In Vivo. *Cell Rep* **17**, 2125-2136, doi:10.1016/j.celrep.2016.10.060 (2016).
- 155 Shi, G., Liu, L., Hyeon, C. & Thirumalai, D. Interphase human chromosome exhibits out of equilibrium glassy dynamics. *Nat Commun* **9**, 3161, doi:10.1038/s41467-018-05606-6 (2018).
- 156 Szabo, Q. *et al.* TADs are 3D structural units of higher-order chromosome organization in *Drosophila*. *Sci Adv* **4**, eaar8082, doi:10.1126/sciadv.aar8082 (2018).
- 157 Boettiger, A. N. *et al.* Super-resolution imaging reveals distinct chromatin folding for different epigenetic states. *Nature* **529**, 418-422, doi:10.1038/nature16496 (2016).

- 158 Schwarzer, W. *et al.* Two independent modes of chromatin organization revealed by cohesin removal. *Nature* **551**, 51-56, doi:10.1038/nature24281 (2017).
- 159 Li, Y. *et al.* Measuring the Autocorrelation Function of Nanoscale Three-Dimensional Density Distribution in Individual Cells Using Scanning Transmission Electron Microscopy, Atomic Force Microscopy, and a New Deconvolution Algorithm. *Microsc Microanal* **23**, 661-667, doi:10.1017/S1431927617000447 (2017).
- 160 Acemel, R. D., Maeso, I. & Gomez-Skarmeta, J. L. Topologically associated domains: a successful scaffold for the evolution of gene regulation in animals. *Wiley Interdiscip Rev Dev Biol* **6**, e265, doi:10.1002/wdev.265 (2017).
- 161 Narendra, V., Bulajic, M., Dekker, J., Mazzoni, E. O. & Reinberg, D. CTCF-mediated topological boundaries during development foster appropriate gene regulation. *Genes Dev* **30**, 2657-2662, doi:10.1101/gad.288324.116 (2016).
- 162 Cremer, T. & Cremer, C. Chromosome territories, nuclear architecture and gene regulation in mammalian cells. *Nat Rev Genet* **2**, 292-301, doi:10.1038/35066075 (2001).
- 163 Dekker, J. & Heard, E. Structural and functional diversity of Topologically Associating Domains. *FEBS Lett* **589**, 2877-2884, doi:10.1016/j.febslet.2015.08.044 (2015).
- 164 Sexton, T. & Cavalli, G. The role of chromosome domains in shaping the functional genome. *Cell* **160**, 1049-1059, doi:10.1016/j.cell.2015.02.040 (2015).
- 165 Dixon, J. R., Gorkin, D. U. & Ren, B. Chromatin Domains: The Unit of Chromosome Organization. *Mol Cell* **62**, 668-680, doi:10.1016/j.molcel.2016.05.018 (2016).
- 166 Huang, K. *et al.* Physical and data structure of 3D genome. *bioRxiv*, 596262 (2019).

- 167 Stevens, T. J. *et al.* 3D structures of individual mammalian genomes studied by single-cell Hi-C. *Nature* **544**, 59-64, doi:10.1038/nature21429 (2017).
- 168 Larson, A. G. & Narlikar, G. J. The Role of Phase Separation in Heterochromatin Formation, Function, and Regulation. *Biochemistry* **57**, 2540-2548, doi:10.1021/acs.biochem.8b00401 (2018).
- 169 Hansen, A. S., Cattoglio, C., Darzacq, X. & Tjian, R. Recent evidence that TADs and chromatin loops are dynamic structures. *Nucleus-Phila* **9**, 20-32, doi:10.1080/19491034.2017.1389365 (2018).
- 170 Bancaud, A. *et al.* Molecular crowding affects diffusion and binding of nuclear proteins in heterochromatin and reveals the fractal organization of chromatin. *EMBO J* **28**, 3785-3798, doi:10.1038/emboj.2009.340 (2009).
- 171 Imai, R. *et al.* Density imaging of heterochromatin in live cells using orientation-independent-DIC microscopy. *Mol Biol Cell* **28**, 3349-3359, doi:10.1091/mbc.E17-06-0359 (2017).
- 172 Bancaud, A., Lavelle, C., Huet, S. & Ellenberg, J. A fractal model for nuclear organization: current evidence and biological implications. *Nucleic Acids Res* **40**, 8783-8792, doi:10.1093/nar/gks586 (2012).
- 173 Bedin, V., Adam, R. L., de Sa, B. C., Landman, G. & Metze, K. Fractal dimension of chromatin is an independent prognostic factor for survival in melanoma. *BMC Cancer* **10**, 260, doi:10.1186/1471-2407-10-260 (2010).

- 174 Cherkezyan, L. *et al.* Nanoscale changes in chromatin organization represent the initial steps of tumorigenesis: a transmission electron microscopy study. *BMC Cancer* **14**, 189, doi:10.1186/1471-2407-14-189 (2014).
- 175 Metze, K. Fractal dimension of chromatin: potential molecular diagnostic applications for cancer prognosis. *Expert Rev Mol Diagn* **13**, 719-735, doi:10.1586/14737159.2013.828889 (2013).
- 176 Rogers, J. D., Radosevich, A. J., Yi, J. & Backman, V. Modeling Light Scattering in Tissue as Continuous Random Media Using a Versatile Refractive Index Correlation Function. *Ieee J Sel Top Quant* **20**, 7000514, doi:10.1109/JSTQE.2013.2280999 (2013).
- 177 Yi, J. *et al.* Spatially resolved optical and ultrastructural properties of colorectal and pancreatic field carcinogenesis observed by inverse spectroscopic optical coherence tomography. *J Biomed Opt* **19**, 36013, doi:10.1117/1.JBO.19.3.036013 (2014).
- 178 Radosevich, A. J. *et al.* Rectal Optical Markers for In Vivo Risk Stratification of Premalignant Colorectal Lesions. *Clin Cancer Res* **21**, 4347-4355, doi:10.1158/1078-0432.CCR-15-0136 (2015).
- 179 Damania, D. *et al.* Nanocytology of rectal colonocytes to assess risk of colon cancer based on field cancerization. *Cancer Res* **72**, 2720-2727, doi:10.1158/0008-5472.CAN-11-3807 (2012).
- 180 Yakushevskaya, A. E. *et al.* STEM tomography in cell biology. *J Struct Biol* **159**, 381-391, doi:10.1016/j.jsb.2007.04.006 (2007).

- 181 Biskupek, J., Leschner, J., Walther, P. & Kaiser, U. Optimization of STEM tomography acquisition—A comparison of convergent beam and parallel beam STEM tomography. *Ultramicroscopy* **110**, 1231-1237 (2010).
- 182 Cherkezyan, L. *et al.* Interferometric spectroscopy of scattered light can quantify the statistics of subdiffractive refractive-index fluctuations. *Phys Rev Lett* **111**, 033903, doi:10.1103/PhysRevLett.111.033903 (2013).
- 183 Barer, R. Refractometry and Interferometry of Living Cells*†. *JOSA* **47**, 545-556 (1957).
- 184 Davies, H. G., Wilkins, M. H. F., Chayen, J. & Lacour, L. F. The Use of the Interference Microscope to Determine Dry Mass in Living Cells and as a Quantitative Cytochemical Method. *Q J Microsc Sci* **95**, 271-& (1954).
- 185 Barer, R. & Tkaczyk, S. Refractive index of concentrated protein solutions. *Nature* **173**, 821-822, doi:10.1038/173821b0 (1954).
- 186 Suloway, C. *et al.* Fully automated, sequential tilt-series acquisition with Legion. *J Struct Biol* **167**, 11-18, doi:10.1016/j.jsb.2009.03.019 (2009).
- 187 Nickell, S. *et al.* TOM software toolbox: acquisition and analysis for electron tomography. *J Struct Biol* **149**, 227-234, doi:10.1016/j.jsb.2004.10.006 (2005).
- 188 Zheng, S. Q. *et al.* UCSF tomography: an integrated software suite for real-time electron microscopic tomographic data collection, alignment, and reconstruction. *J Struct Biol* **157**, 138-147, doi:10.1016/j.jsb.2006.06.005 (2007).
- 189 Donoho, D. L. Compressed sensing. *IEEE Transactions on information theory* **52**, 1289-1306 (2006).

- 190 Zhou, M. *et al.* Nonparametric Bayesian dictionary learning for analysis of noisy and incomplete images. *IEEE Trans Image Process* **21**, 130-144, doi:10.1109/TIP.2011.2160072 (2012).
- 191 Wang, G. J., Garcia, D., Liu, Y., de Jeu, R. & Dolman, A. J. A three-dimensional gap filling method for large geophysical datasets: Application to global satellite soil moisture observations. *Environ Modell Softw* **30**, 139-142, doi:10.1016/j.envsoft.2011.10.015 (2012).
- 192 Levin, B. D. *et al.* Nanomaterial datasets to advance tomography in scanning transmission electron microscopy. *Sci Data* **3**, 160041, doi:10.1038/sdata.2016.41 (2016).
- 193 Wang, S. *et al.* Spatial organization of chromatin domains and compartments in single chromosomes. *Science* **353**, 598-602, doi:10.1126/science.aaf8084 (2016).
- 194 Dong, B. *et al.* Super-resolution spectroscopic microscopy via photon localization. *Nat Commun* **7**, 12290, doi:10.1038/ncomms12290 (2016).
- 195 Henriques, R., Griffiths, C., Hesper Rego, E. & Mhlanga, M. M. PALM and STORM: unlocking live-cell super-resolution. *Biopolymers* **95**, 322-331, doi:10.1002/bip.21586 (2011).
- 196 Dong, B. *et al.* Superresolution intrinsic fluorescence imaging of chromatin utilizing native, unmodified nucleic acids for contrast. *Proc Natl Acad Sci U S A* **113**, 9716-9721, doi:10.1073/pnas.1602202113 (2016).
- 197 Dong, B. *et al.* Stochastic fluorescence switching of nucleic acids under visible light illumination. *Opt Express* **25**, 7929-7944, doi:10.1364/OE.25.007929 (2017).

- 198 Dong, B. Q. *et al.* Parallel Three-Dimensional Tracking of Quantum Rods Using Polarization-Sensitive Spectroscopic Photon Localization Microscopy. *Acs Photonics* **4**, 1747-1752, doi:10.1021/acsphotonics.7b00294 (2017).
- 199 Eshein, A. *et al.* Sub-10-nm imaging of nucleic acids using spectroscopic intrinsic-contrast photon-localization optical nanoscopy (SICLON). *Opt Lett* **43**, 5817-5820, doi:10.1364/OL.43.005817 (2018).
- 200 Dewey, T. G. *Fractals in molecular biophysics*. (Oxford University Press, 1998).
- 201 Flyamer, I. M. *et al.* Single-nucleus Hi-C reveals unique chromatin reorganization at oocyte-to-zygote transition. *Nature* **544**, 110-114, doi:10.1038/nature21711 (2017).
- 202 Lando, D. *et al.* Combining fluorescence imaging with Hi-C to study 3D genome architecture of the same single cell. *Nat Protoc* **13**, 1034-1061, doi:10.1038/nprot.2018.017 (2018).
- 203 Gladstein, S. *et al.* Multimodal interference-based imaging of nanoscale structure and macromolecular motion uncovers UV induced cellular paroxysm. *Nat Commun* **10**, 1652, doi:10.1038/s41467-019-09717-6 (2019).
- 204 Haberfehlner, G., Orthacker, A., Albu, M., Li, J. & Kothleitner, G. Nanoscale voxel spectroscopy by simultaneous EELS and EDS tomography. *Nanoscale* **6**, 14563-14569, doi:10.1039/c4nr04553j (2014).
- 205 Wu, J. S. *et al.* Imaging and elemental mapping of biological specimens with a dual-EDS dedicated scanning transmission electron microscope. *Ultramicroscopy* **128**, 24-31, doi:10.1016/j.ultramic.2013.01.004 (2013).

- 206 Liou, W., Geuze, H. J. & Slot, J. W. Improving structural integrity of cryosections for immunogold labeling. *Histochem Cell Biol* **106**, 41-58 (1996).
- 207 van Rijnsoever, C., Oorschot, V. & Klumperman, J. Correlative light-electron microscopy (CLEM) combining live-cell imaging and immunolabeling of ultrathin cryosections. *Nat Methods* **5**, 973-980, doi:10.1038/nmeth.1263 (2008).
- 208 Polishchuk, R. S. *et al.* Correlative light-electron microscopy reveals the tubular-saccular ultrastructure of carriers operating between Golgi apparatus and plasma membrane. *J Cell Biol* **148**, 45-58 (2000).
- 209 Powell, R. D., Halsey, C. M. & Hainfeld, J. F. Combined fluorescent and gold immunoprobes: reagents and methods for correlative light and electron microscopy. *Microsc Res Tech* **42**, 2-12, doi:10.1002/(SICI)1097-0029(19980701)42:1<2::AID-JEMT2>3.0.CO;2-Y (1998).
- 210 Sartori, A. *et al.* Correlative microscopy: bridging the gap between fluorescence light microscopy and cryo-electron tomography. *J Struct Biol* **160**, 135-145, doi:10.1016/j.jsb.2007.07.011 (2007).

APPENDIX

Appendix A: Chemicals Used in ChromSTEM Staining

<i>Reagent</i>	<i>Formula</i>
<i>Washing solution</i>	Hank's balanced salt solution without calcium and magnesium
<i>Fixation solution</i>	2.5% EM grade glutaraldehyde 2% paraformaldehyde 2 mM CaCl ₂ 0.1 M sodium cacodylate buffer, pH = 7.4
<i>Blocking solution</i>	10 mM glycine 10 mM potassium cyanide 0.1 M sodium cacodylate buffer, pH = 7.4
<i>DNA staining solution</i>	10 μM DRAQ5 0.1% SAPONIN 0.1 M sodium cacodylate buffer, pH = 7.4
<i>Bathing solution</i>	2.5 mM 3,3' - diaminobenzidine tetrahydrochloride (DAB) 0.1 M sodium cacodylate buffer, pH = 7.4
<i>Reduced osmium staining solution</i>	2% osmium tetroxide 1.5% potassium ferrocyanide 2 mM CaCl ₂ 0.15 M sodium cacodylate buffer, pH = 7.4

<p><i>DurcupanTM resin mixture</i></p> <p>1</p>	<p>10 mL DurcupanTM ACM single component A, M, epoxy resin</p> <p>10 mL DurucupanTM ACM single component B, hardener 964</p> <p>0.15 mL DurcupanTM ACM single component D</p>
<p><i>DurcupanTM resin mixture</i></p> <p>2</p>	<p>10 mL DurcupanTM ACM single component A, M, epoxy resin</p> <p>10 mL DurucupanTM ACM single component B, hardener 964</p> <p>0.2 mL DurcupanTM ACM, single component C, accelerator 960</p> <p>0.15 mL DurcupanTM ACM single component D</p>
<p><i>1:1 infiltration mixture</i></p>	<p>10 mL 100% ethanol</p> <p>10 mL DurcupanTM resin mixture 1</p>
<p><i>2:1 infiltration mixture</i></p>	<p>5 mL 100% ethanol</p> <p>10 mL DurcupanTM resin mixture 1</p>

Appendix B: Sample Preparation for ChromSTEM for Cell Cultures

Fixation:

1. Wash the cells in the petri-dish in the washing solution for 3 times, 2 minutes each.
2. Fix the cells with the fixation solution for 5 minutes at room temperature.
3. Continue to fix the cells with fresh fixation solution for an additional 1 hour on ice.

The following steps before the last ethanol dehydration are either on ice or on a cold stage. All reagents must be chilled to 4°C prior to use.

DNA Staining:

4. Wash the cells with 0.1M sodium cacodylate buffer for 5 times on the ice, 2 minutes each.
5. Block the cells with blocking solution for 15 minutes.
6. Stain the cells with DNA staining solution for 10 minutes.
7. Wash the cells with the blocking solution for 3 times, 5 minutes each.

Photo-bleaching:

8. Bath the cells in the bathing solution prior to photo-bleaching
9. Photo-bleach the cells using continuous epi-fluorescence illumination (150 W Xenon Lamp) with Cy5 red filter and a 100x objective for 7 minutes for each spot on the cold stage.
10. Replace the bathing solution in the petri-dish with a fresh bathing solution every 15 minutes (roughly two spots).

Heavy metal staining:

11. Rinse the cells with 0.1 M sodium cacodylate buffer for 5 times, 2 minutes each.
12. Stain the cells with reduced osmium staining solution for 30 minutes.
13. Wash the cells with double distilled water for 5 times, 2 minutes each.

Dehydration and Resin embedding:

14. Dehydrate the cells with serial ethanol (30%, 50%, 70%, 85%, 95%, 100% twice) on ice, 2 minutes each.
15. Wash the cells with 100% ethanol at room temperature for 2 minutes.
16. Infiltrate the cells with 1:1 infiltration mixture at room temperature for 30 minutes.
17. Infiltrate the cells with 2:1 infiltration mixture at room temperature for 2 hours.
18. Infiltrate the cells with DurcupanTM resin mixture 1 at room temperature for 1 hour.
19. Infiltrate the cells with DurcupanTM resin mixture 2 at 50 °C in the dry oven for 1 hour.
20. Flat embed the cells with fresh DurcupanTM resin mixture 2 in Beem capsule and cure at 60 °C in the dry oven for 48 hours.

Appendix C: Sample Preparation for ChromSTEM for Tissue Biopsies

Harvest mouse ovary (Performed by PDX tumor core in Northwestern University)

1. Euthanize the mice and harvest the ovary
2. Dissect the ovary with ideal orientation using a double-edged platinum knife to smaller pieces ($\sim 4^3$ mm³ cubes).
3. Store the tissue biopsies on ice-cold 0.1 M PBS for no more than 30 minutes before the sectioning.

Section the tissue with a vibratome

4. Embed the tissue cubes in 5% low-temperature agarose and chill at 4°C for 5 minutes
5. Section the agarose-tissue sample in ice-cold 0.1 M PBS using a vibratome (Leica) to 40 μ m (roughly 3 layers of cells) slices.
6. Deposit the thin slices onto a plasma treated glass-bottom petri-dish (MatTek) coated with poly-L-lysine, and cover with ice-cold 0.1 M PBS. The tissue slice will adhere to the bottom of the dish due to gravity and poly-L-lysine. DO NOT leave the tissue in PBS for more than 5 minutes before chemical fixation.

ChromSTEM tissue sample preparation

7. Treat the tissue slice in the petri-dish as the cell culture and repeat S1 Protocol for the rest of ChromSTEM sample preparation.

Appendix D: Sample Preparation and Imaging for Photon Localization Microscopy of

A549

Photon Localization Microscopy sample preparation

1. Wash cells with phosphate-buffered saline (PBS) for 2 minutes
2. Fix cell with a solution of 3% Paraformaldehyde and 0.1% Glutaraldehyde in PBS for 10 minutes.
3. Wash cells for 5 minutes in PBS.
4. Quenched cells in 0.1% sodium borohydride in PBS for 7 minutes.
5. Wash cells 3 times in PBS for 5 minutes each
6. Permeabilize cells in blocking buffer (0.2% Triton X-100 and 3% Bovine serum albumin (BSA) in PBS) for 20 minutes.
7. Add the primary antibodies to target heterochromatin (anti-H3K9me3, Abcam and anti-H3K27me3, Abcam) to the blocking buffer to a concentration of 2.5 $\mu\text{g}/\text{mL}$ and incubated for 2 hours.
8. Wash cells in washing buffer (0.1% Triton X-100 and 0.2% BSA in PBS) 3 times for 5 minutes.
9. Incubate cells with the secondary antibody (Alexa Fluor 647, Thermo Fisher Scientific) at a concentration of 2.5 $\mu\text{g}/\text{mL}$ in blocking buffer for 40 minutes.
10. Wash cells two times in PBS for 5 minutes each.
11. Image cells in standard imaging buffer with an oxygen scavenging system containing 0.5 mg/mL glucose oxidase (Sigma-Aldrich), 40 $\mu\text{g}/\text{mL}$ catalase (Roche or Sigma-Aldrich),

143 mM 2-hydroxy-1-ethanethiol, and 100 mg/mL glucose in TN buffer (50 mM Tris (pH 8.0) and 10 mM NaCl)

Appendix E: Sample Preparation for Whole Cheek Cell STEM Tomography

Cheek Cell Collection:

1. Volunteer needs to rinse their mouth before sample collection with water.
2. Gently brush the inner cheek with a CytoBrush from top to bottom in one direction without rotation for 5 times.
3. Rinse the CtyoBrush with cells in PBS (1x) in 1mL vial thoroughly. Rotating the brush gently release the cheek cells into the solution.
4. Concentrate the cell solution by centrifuging at 2000 rpm, dispose of the supernatant carefully, and resuspend the cell pellet in 1 mL fresh PBS
5. Concentrate the cell solution again by centrifuging at 2000 rpm, dispose of the supernatant, and resuspend the cell pellet in 100 uL fresh PBS

Cell attachment:

6. Carefully deposit 30 μ L cell suspension onto a hydrophobic surface (ideally the cap of the petri-dish, a droplet will form.
7. Place the TEM grid with carbon/formvar film on the droplet, and the plasma-treated side in touch with the liquid.
8. Flip the petri-dish cap and the grid will hang freely because of the surface tension of the droplet. Place the cap onto a wet chamber and leave the sample in a cell incubator at 37°C for 30 min.

Fixation:

9. Carefully flip the cap again so the TEM grid is on top of the droplet. Deposit 5 100 μ L 1x PBS droplets onto a hydrophobic surface (parafilm). Carefully rinse the TEM grid by floating it on the 100 μ L droplet for 2 min each. Transfer the grid with a loop tool or carefully with a pair of tweezers.
10. Deposit 100 μ L droplet of EM fixative (same as the ChrmSTEM fixative in Appendix A). Float the TEM grid on top of the droplet for 20 min at room temperature.
11. Deposit 5 100 μ L DI droplet onto a hydrophobic surface (parafilm) Carefully rinse the TEM grid by floating on the 100 μ L droplet for 2 min each. Transfer the grid with a loop tool or carefully with a pair of tweezers.

Dehydration (Freeze-dry method):

12. Plunge freeze the sample in liquid ethane with Vitrobot. Blot the sample once for 1s before freezing
13. Transfer the frozen sample into a turbo freeze dryer, follow the protocol for cell sample.

Dehydration (Critical point dry method):

12. Transfer the frozen sample into a turbo freeze dryer, follow the protocol for cell sample.
13. Dehydrate the sample in ethanol with progressively higher concentration (30%, 50%, 70%, 85%, 95%, 100% x 2 times) in a foam capsule for 10 min in each concentration.
14. Transfer the sample into a critical point dryer and follow the protocol for a small sample.

Appendix F: Publications

Peer-Reviewed

1. **Li, Yue**, Eshein, Adam, Biqin Dong, Luay M. Almassalha, John E. Chandler, Karl A. Hujsak, Vinayak P. Dravid, Cheng Sun, Hao F. Zhang, and Vadim Backman. "Sub-10-nm imaging of nucleic acids using spectroscopic intrinsic-contrast photon-localization optical nanoscopy (SICLON)." *Opt Lett* 43, no. 23 (2018): 5817-5820.
2. **Li, Yue**, Luay M. Almassalha, John E. Chandler, Xiang Zhou, Yolanda E. Stypula-Cyrus, Karl A. Hujsak, Eric W. Roth, et al. "The effects of chemical fixation on the cellular nanostructure." *Exp Cell Res*, **358**, no. 2 (2017): 253-259.
3. **Li, Yue**, Di Zhang, Ilker Capoglu, Karl A. Hujsak, Dhwani Damania, Lusik Cherkezyan, Eric Roth, et al. "Measuring the Autocorrelation Function of Nanoscale Three-Dimensional Density Distribution in Individual Cells Using Scanning Transmission Electron Microscopy, Atomic Force Microscopy, and a New Deconvolution Algorithm." *Microsc Microanal* **23**, no. 3 (2017): 661-667.
4. Hujsak, Karl A., Eric W. Roth, William Kellogg, **Yue Li**, and Vinayak P. Dravid. "High speed/low dose analytical electron microscopy with dynamic sampling." *Micron* **108** (2018): 31-40.
5. Nandwana, Vikas, Abhalaxmi Singh, Marisa M. You, Gefei Zhang, John Higham, Tiffany S. Zheng, **Yue Li**, Pottumarthi V. Prasad, and Vinayak P. Dravid. "Magnetic lipid

- nanocapsules (MLNCs): self-assembled lipid-based nanoconstruct for non-invasive theranostic applications." *J Mater Chem B* **6**, no. 7 (2018): 1026-1034.
6. Gürsoy, Doğa, Young P. Hong, Kuan He, Karl Hujsak, Seunghwan Yoo, Si Chen, **Yue Li** et al. "Rapid alignment of nanotomography data using joint iterative reconstruction and reprojection." *Sci Rep* **7**, no. 1 (2017): 11818.
 7. Gao, Changrui, Honghao Li, **Yue Li**, Sumit Kewalramani, Liam C. Palmer, Vinayak P. Dravid, Samuel I. Stupp, Monica Olvera de la Cruz, and Michael J. Bedzyk. "Electrostatic control of polymorphism in charged amphiphile assemblies." *J Phys Chem B* **121**, no. 7 (2017): 1623-1628.
 8. Nandwana, Vikas, S-R. Ryoo, S. Kanthala, A. Kumar, A. Sharma, F. C. Castro, **Yue Li**, B. Hoffman, S. Lim, and V. P. Dravid. "Engineered ferritin nanocages as natural contrast agents in magnetic resonance imaging." *RSC Advances* **7**, no. 55 (2017): 34892-34900.
 9. Nandwana, Vikas, Soo-Ryoon Ryoo, Shanthi Kanthala, Kaylin M. McMahon, Jonathan S. Rink, **Yue Li**, Subbu S. Venkatraman, C. Shad Thaxton, and Vinayak P. Dravid. "High-density lipoprotein-like magnetic nanostructures (HDL-MNS): theranostic agents for cardiovascular disease." *Chem Mater* **29**, no. 5 (2017): 2276-2282.
 10. Zhang, Di, Ilker Capoglu, **Yue Li**, Lusik Cherkezyan, John Chandler, Graham Spicer, Hariharan Subramanian, Allen Taflove, and Vadim Backman. "Finite-difference time-domain-based optical microscopy simulation of dispersive media facilitates the development of optical imaging techniques." *J Biomed Opt* **21**, no. 6 (2016): 065004.

Preprint

1. **Li, Yue**, Eric W. Roth, Vasundhara Agrawal, Adam Eshein, Jane Frederick, Luay Matthew Almassalha, Anne Shim, Reiner Bleher, Vinayak P. Dravid, and Vadim Backman. "Quantifying Three-dimensional Chromatin Organization Utilizing Scanning Transmission Electron Microscopy: ChromSTEM." *bioRxiv* (2019): 636209.
2. Huang, Kai, **Yue Li**, Anne R. Shim, Rikkert J. Nap, Vasundhara Agrawal, Ranya KA Virk, Adam Eshein, Luay M. Almassalha, Vadim Backman, and Igal Szleifer. "Physical and data structure of 3D genome." *bioRxiv* (2019): 596262.
3. Zhou, Xiang, Luay Almassalha, **Yue Li**, Adam Eshein, Lusik Cherkezyan, Parvathi Viswanathan, Hariharan Subramanian, Igal Szleifer, and Vadim Backman. "Preservation of cellular nano-architecture by the process of chemical fixation for nanopathology." *bioRxiv* (2018): 371286.